Politecnico di Torino

Master of Science: Sustainable Nuclear Energy
A.a. 2024/2025

Master Thesis

Graduation session, March 2025

Analysis of electrons vs. ions energy transport in TCV with the SOLPS-ITER code

Swiss Plasma Center at
EPFL

Relator, Politecnico di Torino:

Fabio Subba

Relators, Swiss Plasma Center:

Holger Reimerdes, Elena Tonello

Candidate:

Stefano Angelo Donzella

Abstract

The growing demand for energy, coupled with the urgent need to mitigate global warming, necessitates the development of sustainable and carbon-free energy sources. Nuclear fusion presents a promising solution, offering a virtually limitless energy supply with minimal environmental impact. In line with the Sustainable Development Goals (SDGs), particularly SDG 7 (Affordable and Clean Energy) and SDG 13 (Climate Action), advancing fusion energy is critical for ensuring a sustainable energy future. However, significant challenges remain in achieving viable fusion power, one of which is the Power Exhaust problem in tokamak devices. The extreme heat fluxes directed towards the reactor walls pose a major limitation, requiring effective plasma confinement and exhaust solutions, such as the divertor, to manage energy and particle transport.

This thesis focuses on the energy transport mechanisms of electrons and ions in the Tokamak à Configuration Variable (TCV), particularly in the outer core and Scrape-Off Layer (SOL) through the SOLPS-ITER code. This work presents a parametric study on the energy balance in the SOL of the TCV tokamak, specifically in its SILO baffled configuration on a Lower Single Null divertor. The primary focus is on ion and electron energy transport, particularly near the last flux surface, where discrepancies between experimental and simulated ion temperature, electron density and temperature profiles have been observed.

To investigate the dominant transport mechanisms, we conduct a systematic scan on key parameters affecting energy balance and transport, namely: (i) the power split between electrons and ions at fixed total input power, (ii) the anomalous cross-field energy transport coefficients, and (iii) the ion flux limiter on parallel heat conduction. The study explores how these parameters influence plasma temperature profiles, power balance, and the electron-ion temperature difference in the SOL. Given the limitations of fluid-based codes such as SOLPS-ITER, which rely on effective transport coefficients rather than fully resolving turbulence, these scans provide insight into the effects of anomalous transport and non-local heat flux regulation.

The results, obtained through an analysis of fundamental plasma variables and internal energy balance equations, provide valuable input for refining transport models and improving the predictive capabilities of SOLPS-ITER. This study contributes to a better understanding of energy transport in the SOL and informs future efforts in plasma edge modeling for tokamak operation.

Sommario

La crescente domanda di energia, unita all'urgente necessità di mitigare il riscaldamento globale, rende indispensabile lo sviluppo di fonti energetiche sostenibili e prive di emissioni di carbonio. La fusione nucleare rappresenta una soluzione promettente, offrendo una fonte di energia virtualmente illimitata con un impatto ambientale minimo. In linea con gli Obiettivi di Sviluppo Sostenibile (SDG), in particolare l'SDG 7 (Energia Accessibile e Pulita) e l'SDG 13 (Azione per il Clima), il progresso della fusione è fondamentale per garantire un futuro energetico sostenibile. Tuttavia, rimangono significative sfide nel raggiungere una fusione praticabile, tra cui il problema dell'esaurimento della potenza nei dispositivi tokamak. I flussi di calore estremi diretti verso le pareti del reattore rappresentano una limitazione critica, richiedendo soluzioni efficaci per il confinamento e l'espulsione del plasma, come il divertore, per gestire il trasporto di energia e particelle.

Questa tesi si concentra sui meccanismi di trasporto energetico degli elettroni e degli ioni nel Tokamak à Configuration Variable (TCV), in particolare nel nucleo esterno e nello Scrape-Off Layer (SOL), utilizzando il codice SOLPS-ITER. Questo lavoro presenta uno studio parametrico sull'equilibrio energetico nel SOL del tokamak TCV, specificamente nella sua configurazione baffled SILO con un divertore Lower Single Null. L'attenzione principale è rivolta al trasporto di energia degli elettroni e degli ioni, con particolare focus sulla regione vicino all'ultima superficie di flusso, dove sono state osservate discrepanze tra le temperature ioniche sperimentali e simulate, così come nei profili di densità ed energia degli elettroni.

Per indagare i meccanismi di trasporto dominanti, è stata condotta un'analisi sistematica su parametri chiave che influenzano l'equilibrio energetico e il trasporto, in particolare: (i) la distribuzione della potenza tra elettroni e ioni a potenza totale fissata, (ii) i coefficienti di trasporto energetico anomalo attraverso il campo magnetico e (iii) il flux limiter ionico sulla conduzione termica parallela. Lo studio esplora come questi parametri influenzino i profili di temperatura del plasma, il bilancio energetico e la differenza di temperatura tra elettroni e ioni nel SOL. Data la natura dei codici fluidodinamici come SOLPS-ITER, che si basano su coefficienti di trasporto efficaci piuttosto che sulla risoluzione completa della turbolenza, questi studi parametrici forniscono informazioni sui meccanismi di trasporto anomalo e sulla regolazione del flusso termico non locale.

I risultati, ottenuti attraverso l'analisi delle variabili fondamentali del plasma e delle equazioni di bilancio energetico interno, forniscono contributi significativi per il miglioramento dei modelli di trasporto e delle capacità predittive di SOLPS-ITER. Questo studio contribuisce a una migliore comprensione del trasporto energetico nel SOL e supporta lo sviluppo di modelli avanzati per l'operatività dei tokamak.

Contents

Contents **i**

List of Figures **iii**

1 Introduction **1**
- 1.1 Why nuclear fusion? 1
  - 1.1.1 Energy outlook 1
  - 1.1.2 Nuclear fusion energy 2
- 1.2 Nuclear fusion physics 3
  - 1.2.1 Plasma state 5
  - 1.2.2 Charged particle collisions in plasmas 5
  - 1.2.3 Energy balance and the Lawson criterion 7
  - 1.2.4 Magnetic confinement 9
- 1.3 The Power Exhaust challenge 12
  - 1.3.1 The detachment 14
- 1.4 TCV tokamak 15
  - 1.4.1 Divertor upgrade 16
- 1.5 Aim of the thesis 17

2 Edge plasma physics **19**
- 2.1 Plasma transport 19
  - 2.1.1 Drifts effect 20
- 2.2 Physics of the Scrape Off Layer 22
  - 2.2.1 The Scrape Off Layer 22
  - 2.2.2 Fluid Model - Braginskii equations 23
  - 2.2.3 Plasma sheath 27

3 Scrape-Off-Layer modeling **35**
- 3.1 Analytic 2 Point Modeling 35
- 3.2 The SOLPS-ITER code 38
  - 3.2.1 B2.5 multi-fluid code 39
  - 3.2.2 B2.5 model equations 41
  - 3.2.3 EIRENE code 43

4 Simulation results **47**
- 4.1 Input power on electrons and ions 49
  - 4.1.1 Attached case 49

4.1.2 Internal energy balance 52
4.1.3 Detached case 54
4.2 Anomalous cross-field energy diffusivity 57
4.2.1 Ion χ_i 57
4.2.2 Electron χ_e 61
4.3 The ion flux limiter 65
4.3.1 Power balance 69

5 Conclusion and perspectives **73**

Bibliography **75**

List of Figures

1.1 Relevant data stating the existence of the global warming threat, from [1] 2
1.2 Binding energy per nucleon over the number of nucleons in the nucleus 3
1.3 Thermonuclear reaction rates 4
1.4 Geometry of the Coulomb collision orbit 6
1.5 Charged particle trajectory along a straight field line B 10
1.6 Particle trajectory in a helical magnetic field [2] 11
1.7 Sketch of the two main magnetic confinement devices 12
1.8 Different ways to bring the plasma edge in contact with the wall, taken from [2] 13
1.9 Radiative loss parameter L_z from ADAS, as the sum of line radiation, recombination-induced radiation and bremsstrahlung (from [3]) 14
1.10 Poloidal section of TCV (*source: epfl.ch*) 15
1.11 TCV tokamak (*source: epfl.ch*) 16

2.1 Turbulent and parallel transport processes in the divertor volume, taken from [4] 22
2.2 Debye shielding 1-D, taken from [5] 27
2.3 Electron–Ion energy transfer mechanism, transferring energy $|e\phi_{sf}|$ from electron to ion. Inspired by [6] 30
2.4 Plasma wall interaction when the angle between **B** and the solid surface is oblique. Taken by [6] 31

3.1 SOLPS-ITER workflow, taken by [7] 39
3.2 a) Curvilinear reference frame of B2.5 . b) Geometrical reference frame of a tokamak (ASDEX in figure), taken by [8] 40
3.3 B2.5 mesh of TCV SILO 40
3.4 B2.5 computational space in a LSN configuration, inspired by [5] 41
3.5 Eirene grid of TCV SILO 44

4.1 Regions division in the TCV SILO simulated: Core, SOL, Inner divertor, Outer divertor 47
4.2 Upstream plasma parameters - percentage power distribution represents $P^e_{core}/P^{tot}_{core}$ – $P^i_{core}/P^{tot}_{core}\%$ - *Power split* 50
4.3 a) Power transport in the core b) Collisional heat transfer in the regions - refer to figure 4.1 for the identification of the regions 51
4.4 Temperatures in the outer core and in the SOL - Outer Mid Plane. Electrons in blue, ions in red 51
4.5 Target plasma variables - *Power split* 52
4.6 Target plasma fluxes - *Power split* 52
4.7 Internal energy balance in the Scrape-Off Layer - *Power split* 53

4.8 Internal energy balance in the divertor legs - *Power split* 54
4.9 a) Power transport in the core b) Collisional heat transfer in the regions - refer to figure 4.1 for the identification of the regions 55
4.10 Target plasma variables 55
4.11 Target plasma fluxes 56
4.12 2PMf on the outer divertor - comparison between the attached and detached case with the two opposite power splits 57
4.13 Upstream plasma variables - χ_i 58
4.14 Temperatures in the outer core and in the SOL - Outer Mid Plane. Electrons in blue, ions in red - χ_i 58
4.15 Target plasma variables - χ_i 59
4.16 Target plasma fluxes - χ_i 59
4.17 Internal energy balance in the Scrape-Off Layer - χ_i 60
4.18 Internal energy balance in the divertor legs - χ_i 61
4.19 Upstream plasma variables - χ_e 61
4.20 Temperatures in the outer core and in the SOL - Outer Mid Plane. Electrons in blue, ions in red - χ_e 62
4.21 Target plasma variables - χ_e 62
4.22 Target plasma fluxes χ_e 63
4.23 Internal energy balance in the Scrape-Off Layer - χ_e 64
4.24 Internal energy balance in the divertor legs - χ_e 65
4.25 Upstream plasma variables - *cflmi* 66
4.26 Temperatures in the outer core and in the SOL - Outer Mid Plane - *cflmi* 66
4.27 Trend of variables from OMP towards the outer target, averaged in the common flux region (CFR) from OMP to the target. 67
4.28 Target plasma variables - *cflmi* 67
4.29 Target plasma fluxes - *cflmi* 68
4.30 Neutral density and potential drop at the divertor targets 69
4.31 2PM formatting analysis on the two opposite cases 69
4.32 Total power entering in the outer divertor CFR and flowing towards the target 70
4.33 Internal energy balance in the Scrape-Off Layer - *cflmi* 70
4.34 Internal energy balance in the divertor legs - *cflmi* 71

"Nobody ever figures out what life is all about, and it doesn't matter. Explore the world. Nearly everything is really interesting if you go into it deeply enough"

— Richard P. Feymann

1. Introduction

1.1 Why nuclear fusion?

1.1.1 Energy outlook

Since the Industrial Revolution, Earth's average air temperatures have been rising. While natural variability contributes to climate fluctuations, the overwhelming evidence indicates that human activities—particularly the emission of greenhouse gases—are the primary drivers of global warming. It is important to note that global warming does not mean uniform temperature increases everywhere; some regions may experience significant warming, while others may see cooling. For example, exceptionally cold winters in one area might be offset by extremely warm winters elsewhere. Generally, warming is more pronounced over land than over oceans because water has a higher heat capacity and takes longer to heat up or cool down. Additionally, warming can vary significantly within specific landmasses and ocean basins.

We might wonder why a one or two-degree increase in global temperature matters, especially since daily temperatures can fluctuate by several degrees. Local and short-term temperature variations are influenced by predictable cycles (like day and night, or seasons) and unpredictable weather patterns. However, the global temperature is primarily determined by the balance between the energy Earth receives from the Sun and the energy it radiates back into space. While solar energy remains relatively constant year-to-year, the amount of energy Earth radiates is closely linked to the composition of its atmosphere, particularly the concentration of greenhouse gases. A one-degree global temperature change is significant because it requires a substantial amount of heat to warm the entire planet by that amount. Historically, even a one to two-degree drop in global temperature was enough to trigger the Little Ice Age, and a five-degree drop led to the extensive glaciation of North America 20,000 years ago.

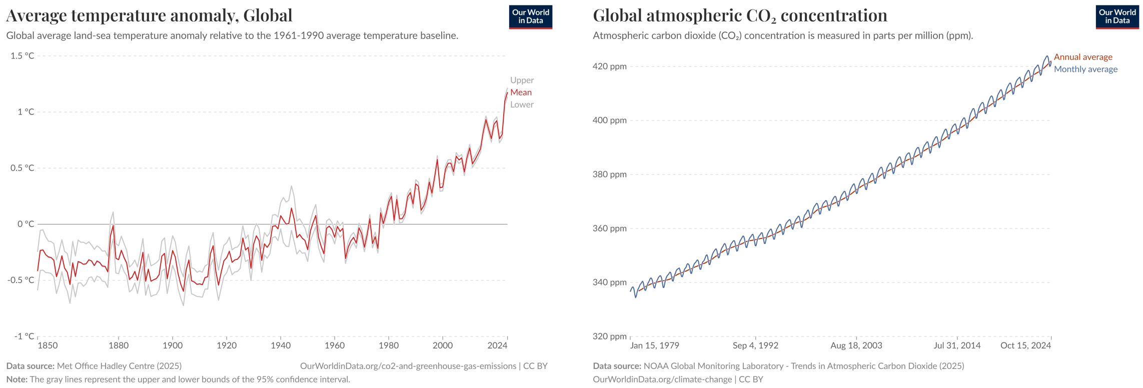

(a) Global temperature trend

(b) Global CO_2 concentration trend

Figure 1.1: Relevant data stating the existence of the global warming threat, from [1]

The trends above clearly demonstrate that human activities are the primary contributors to global warming, with energy production from fossil fuels being the most significant factor. Therefore, transitioning to clean and safe energy sources is essential for the well-being of our planet and future generations. More details can also be found in [9].

1.1.2 Nuclear fusion energy

Nuclear fusion is the process in which two light atomic nuclei merge to form a heavier nucleus, releasing an immense amount of energy. Fusion reactions occur in a state of matter known as plasma—a hot, ionized gas composed of free-moving electrons and positively charged ions. Plasma has unique properties that set it apart from solids, liquids, and gases.

This reaction is the power source of the Sun and all other stars. For fusion to occur in the Sun, atomic nuclei must collide at extremely high temperatures—around ten million degrees Celsius. These temperatures provide the necessary energy to overcome the natural electrostatic repulsion between nuclei. Once they are close enough, the strong nuclear force takes over, allowing them to fuse. To achieve this, nuclei must be confined in a small space to increase the probability of collisions. In the Sun, immense gravitational pressure creates the required conditions for fusion. However, since Earth lacks this natural compression, significantly higher temperatures—exceeding 100 million degrees Celsius—are needed to induce fusion with deuterium and tritium. Additionally, magnetic and pressure regulation is required to sustain stable plasma confinement and keep the fusion reaction active long enough to produce more energy than is consumed to initiate it.

If fusion can be harnessed at an industrial scale, it could provide a virtually limitless, clean, safe, and cost-effective energy source to meet global demand. Fusion has the potential to generate four times more energy per kilogram of fuel than nuclear fission (the process used in current nuclear power plants) and nearly four million times more energy than fossil fuels like coal and oil.

Most fusion reactor designs under development rely on a fuel mixture of deuterium and tritium, both isotopes of hydrogen. Fusion fuel is abundant and easily accessible: deuterium can be inexpensively extracted from seawater, while tritium can potentially be produced by the interaction of fusion-generated neutrons with lithium, which is naturally widespread. These fuel reserves could sustain energy production for millions of years.

Furthermore, fusion is inherently safe and does not produce long-lived, high-level nuclear waste. Since initiating and maintaining fusion is highly complex, there is no risk of a runaway reaction or meltdown.

Fusion can only occur under precisely controlled conditions, and in the event of a malfunction or system failure, the plasma would rapidly lose energy and extinguish itself before causing harm to the public.

1.2 Nuclear fusion physics

As previously mentioned, the process of combining lighter nuclei to make heavier and more stable nuclei is called nuclear fusion. As with fission reactions, fusion reactions are exothermic—they release energy. The energy released during fusion arises from a fundamental property of nuclear matter known as *binding energy*. The binding energy of a nucleus measures the strength of the force that holds its constituent nucleons—protons and neutrons—together. A higher binding energy indicates a more stable nucleus. When light nuclei fuse to form a heavier nucleus, the resulting nucleus has a higher binding energy per nucleon, and the difference in binding energy is released as kinetic energy.

As shown in figure 1.2, all nuclei up to ^{56}Fe can undergo exothermic fusion reaction. Anyway, the most efficients for energy production are the ones with very light nuclei for two main reasons. First, the gain in binding energy per nucleon is significantly larger when two light nuclei fuse. Second, fusion requires overcoming the Coulomb potential barrier, which arises from the positive charges of the nuclei. Using lighter nuclei minimizes the energy needed to trigger the reaction. This is why hydrogen and helium isotopes are the most commonly used reactants in fusion applications.

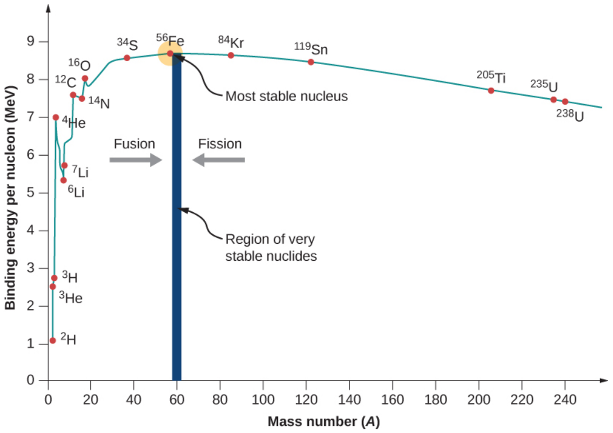

Figure 1.2: Binding energy per nucleon over the number of nucleons in the nucleus

But, it is not easy to achieve fusion. The cross section, figure 1.3a, quantifies the likelihood of a specific reaction occurring between particles and varies with their relative collision energy. Quantum mechanics shows that fusion cross section ([10]) can be defined by the product of three factors:

$$\sigma = S(E)\frac{1}{E}e^{(-B_G/\sqrt{E})} \tag{1.1}$$

where $S(E)$ is the astrophysical S-factor and B_G is the Gamow factor.

In practice, particles collide with a range of relative velocities, each corresponding to different collision energies. The distribution of these velocities is described by a function, $\boldsymbol{f(v)}$, which represents the probability density of the particles having a particular relative velocity between the two populations. This distribution influences the overall probability of the reaction, as reactions are more likely at certain collision energies. Thus, the reaction rates can be determined:

$$\langle \sigma v \rangle = \int \sigma(v) v f(\mathbf{v}) d\mathbf{v} \tag{1.2}$$

Reaction rates can be used to estimate the number of reactions per unit volume and time as:

$$N_V = n_i n_j \langle \sigma v \rangle \tag{1.3}$$

where n_i, n_j are the particle densities of the fusion reactants.

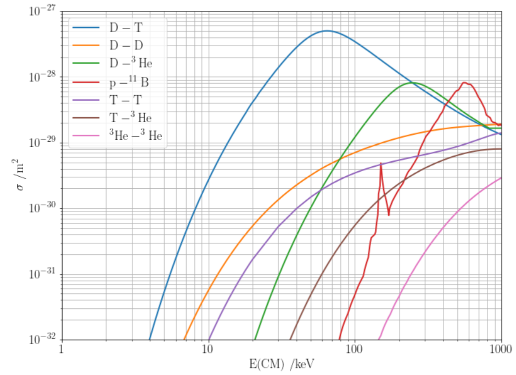

(a) Nuclear fusion cross sections over the center of mass kinetic energy

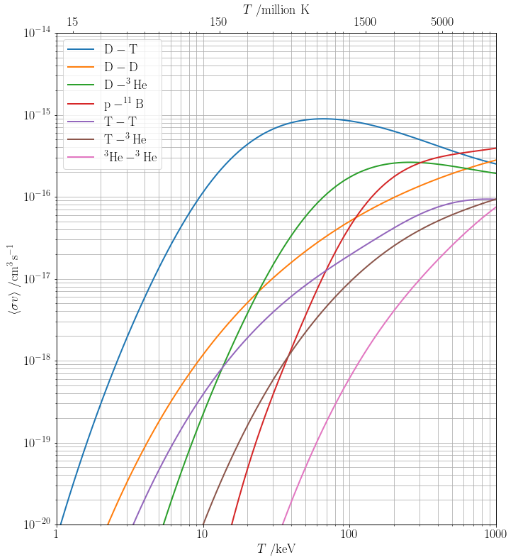

(b) Thermonuclear reaction rates [11]

Figure 1.3: Thermonuclear reaction rates

Looking to the reaction rates in figure 1.3b, we clearly see that the most favorable one at affordable temperatures, i.e. in a range around 10-100 keV (corresponding to over a hundred million Celsius degrees), is the D-T. The fusion of D and T, two hydrogen isotopes, gives birth to a helium nucleus and a highly energetic neutron.

$$D + T \rightarrow {}^4He(3.5MeV) + n(14.1MeV) \tag{1.4}$$

The neutron cannot be, being electrically neutral, confined by electric or magnetic fields (as will be described in 1.2.4). But, its high kinetic energy can be used to sustain a thermodynamic cycle to produce electric energy. While, the energetic *α particle* (${}^4He$), being positively charged, stays confined within the magnetically confined plasma transferring energy to the bulk fuel. This mechanism is called *alpha heating* (or self-heating).

1.2.1 Plasma state

As just mentioned at the end of section 1.2, to make fusion between D and T happen very high temperatures are required. As a direct consequence, we cannot expect fuel atoms to remain electrically neutral when exposed to such extreme temperatures. In a reactor, particle collisions are intense enough to easily strip electrons from hydrogen atoms. Therefore, the fuel in a fusion reactor should not be considered a simple gas but rather a collection of different charged particles: positive ions and electrons. As a first approximation, we do not need to differentiate between deuterium and tritium ions in the following discussion, since their similar mass and identical electrical charge result in comparable properties. The most straightforward way to describe this environment is as a mixture of two distinct gases: one composed of ions and the other of electrons.

However, this mixture behaves very differently from the common gas mixtures we are familiar with (such as air). These differences stem from the following two key characteristics:

- Although the gas mixture remains globally neutral—since ions and electrons are no longer bound to each other but do not escape the reactor chamber—it contains an extremely large number of free electric charges. As a result, this mixture exhibits excellent electrical conductivity.
- Ions and electrons have vastly different masses (recall that $m_i/m_e \approx 4000$). This implies that electrons will respond almost instantaneously to any perturbation caused by external conditions, whereas ions will react much more slowly and that the energy exchange between them will not be very efficient.

Furthermore, when the density of an ionized gas is sufficiently high, an entirely new behavior emerges. Due to the long-range nature of Coulomb collisions, each ion or electron continuously interacts with all other particles in the reactor simultaneously. While interactions with distant charges are weak, a sufficiently high particle density allows the cumulative effect of numerous small interactions to produce a significant macroscopic impact. As a result, every region of matter within the reactor both influences and is influenced by all other regions. When these collective effects become strong in an ionized gas, the system is referred to as a *plasma.*

1.2.2 Charged particle collisions in plasmas

Since we are talking about a strongly ionized gas, we have to focus on collisions between charged particles occurring in the plasma. Collisions of charged particles are the result of the *long range Coulomb force* and can be considered as elastic. We can define a collision as a binary interaction between two charged particles. This is an approximation, since the trajectory of a particle is influenced by many other particles at once. We will take into account this by considering the combined effect of many binary collisions.

Taking 2 charged particles, we can say they have initial velocities $\mathbf{v_1}$, $\mathbf{v_2}$ and final ones $\mathbf{v_1'}$, $\mathbf{v_2'}$ after the interaction. Mass and charge are conserved, and, since we are talking about elastic collisions, even momentum and energy are conserved:

$$m_1\mathbf{v_1} + m_2\mathbf{v_2} = m_1\mathbf{v_1'} + m_2\mathbf{v_2'} \tag{1.5}$$

$$m_1 v_1^2 + m_2 v_2^2 = m_1 v_1'^2 + m_2 v_2'^2 \tag{1.6}$$

Defining the velocity of the center of mass

$$\mathbf{u} = \frac{m_1\mathbf{v_1} + m_2\mathbf{v_2}}{m_1 + m_2} = const \tag{1.7}$$

the relative velocity

$$\mathbf{v} = \mathbf{v_1} - \mathbf{v_2} \tag{1.8}$$

and the reduced mass

$$\mu = \frac{m_1 m_2}{m_1 + m_2} \tag{1.9}$$

We know that the force acting on the 2 particles is the Coulomb force

$$F(\mathbf{r}) = \frac{q_1 q_2}{4\pi\varepsilon_0}\frac{\mathbf{r}}{r^3} = \mu\frac{d\mathbf{v}}{dt} \tag{1.10}$$

, exerting an effect equal and contrary depending on the reduced mass μ. From conservation of energy and momentum we know that the final velocity $|\mathbf{v}'|$ is equal to the initial one $|\mathbf{v}|$, i.e. the velocity changes direction but not magnitude.

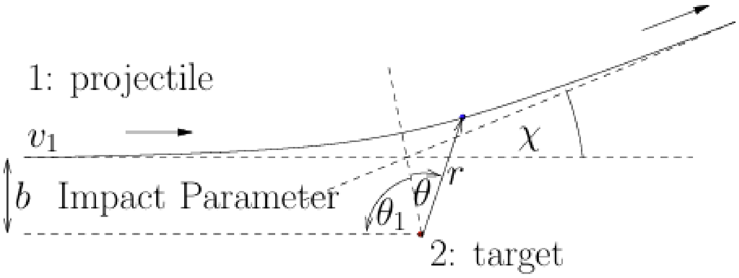

Figure 1.4: Geometry of the Coulomb collision orbit

In the above picture, b is the impact parameter and χ is the deflection angle. Usually, a parameter named b_{90} is defined, which is the distance needed from particle 1 to be deviated of a 90 degrees angle.

Energy transfer rate due to collisions

The cumulative effect of multiple small-angle collisions has an effect on the momentum and energy transfer rate between particles. The last one is also why we have *thermalisation.*

The kinetic energy lost by a collision by particle 1, $\Delta E_k = E_k - E_k'$, which after several passages (Appendix B of [12]), becomes:

$$\Delta E_k \cong \frac{1}{2} m_1 v^2 \frac{m_1 m_2}{(m_1 + m_2)^2}\chi^2 \tag{1.11}$$

and since we are considering small angles ($\chi \simeq 2b_{90}/b$)

$$\Delta E_k \cong \frac{1}{2} m_1 v^2 \frac{m_1 m_2}{(m_1 + m_2)^2} \left(\frac{2b_{90}}{b} \right)^2 \tag{1.12}$$

Looking to the loss of energy per unit length

$$\frac{dE_k}{dl} = \frac{1}{v} \frac{dE_k}{dt} \tag{1.13}$$

it is possible to define the **collision frequency** for energy loss:

$$\nu_{E_k} = \frac{1}{E_k} \frac{dE_k}{dt} = v \frac{1}{E_k} \frac{dE_k}{dl} \tag{1.14}$$

i.e. the rate at which collisions take place removing energy. Due to the fact that $\frac{dE_k}{dl} \propto ln\Lambda$, where $ln\Lambda$ is the *Coulomb logarithm* [13], it results:

$$\nu_{E_K} = \frac{n q_1^2 q_2^2}{2\pi \varepsilon_0^2 m_1 m_2} \frac{ln\Lambda}{v^3} \tag{1.15}$$

In particular, in a plasma there can be 4 different kinds of collisions between charged particles, i.e. $e \to i, e \to e, i \to e, i \to i$. Analysing the $e \to i$ collision, its collision frequency will be:

$$\nu_{ei} = \frac{n_i Z^2 e^4}{2\pi \varepsilon_0^2 m_i m_e} \frac{ln\Lambda}{v_e^3} \tag{1.16}$$

where the electron velocity is thermal $v_{th,e} = \sqrt{T_e/m_e}$ resulting in:

$$\nu_{ei} = \frac{n_i Z^2 e^4}{2\pi \varepsilon_0^2 m_i m_e} \frac{ln\Lambda}{T_e^{3/2}} \tag{1.17}$$

Up to this point, we have considered the case of a single particle with a given velocity v colliding with a fixed target. However, in a plasma, we typically deal with many particles of the same species, each having different velocities—what we refer to as a population. Since tracking the dynamics of each individual particle is impractical, we are often more interested in the average behavior of this population, particularly in terms of energy and momentum transfer, rather than focusing on individual interactions. A common way to describe such a population is through its distribution function *f*. The average is performed over the distribution function (see [12]).

The collision rate is strictly related to the *equilibration time* $\tau \equiv \nu^{-1}$ describing the thermal exchange, in the absence of transport, between species

$$\frac{dT_i}{dt} = \frac{T_e - T_i}{\tau_{ei}} \tag{1.18}$$

The frequency of collisions is dominated by the fastest component, i.e. the electrons. However, because of the difference of mass the energy transfer in a collision is inefficient and only a fraction ($\sim m_e/m_i$) of the electron energy is transferred to the ions[14].

1.2.3 Energy balance and the Lawson criterion

Constructing a fusion reactor involves

- assembling a sufficient quantity of nuclear fuel
- achieving the necessary conditions for the desired reactions to occur at a sufficiently high rate
- maintaining these conditions for as long as possible, ideally in a steady-state regime.

To obtain an initial rough estimate of the parameters characterizing a fusion reactor, it is common to adopt a 0-D (zero-dimensional) model based on lumped parameters, which is defined in terms of the plasma's internal energy content. This model is derived from the full set of 3-D fluid equations (section 2.2.2) by applying a series of simplifying assumptions [15]. First, the fuel is considered to be a $50\% - 50\%$ deuterium-tritium (D-T) mixture, with a negligible concentration of alpha particles. As a result, the number densities satisfy the relation $2n_D = 2n_T = n_e \equiv n$ and $n_\alpha << n$. Second, all fuel components are assumed to be at the same temperature, such that $T_D = T_T = T_e \equiv T$. Third, the plasma is considered to be fully ionized and near thermodynamic equilibrium, meaning the particle velocity distributions follow Maxwellian statistics. Under these conditions, the internal energy density and pressure for each species j are given by $U_j = (3/2)n_jT_j$ and $p_j = n_jT_j$. The total internal energy density and pressure of the fuel are then $U = U_D + U_T + U_e = 3nT$ and $p = p_D + p_T + p_e = 2nT$. With these, the energy balance equation can be rewritten in a simplified form. Inside this equation, a term describing sources and sinks is present [15].

In such a hot environment, there will be strong volumetric power losses (W/m^3), as the Brehmsstrahlung radiation

$$S_B = C_B Z_{eff} n^2 \sqrt{T} \tag{1.19}$$

where C_B is a constant, and conduction losses

$$S_\kappa = \frac{3}{2}\frac{p}{\tau_E} \tag{1.20}$$

where τ_E is the *energy confinement time*, which is a measure of how effectively the reactor retains its internal energy, that can be defined as

$$\tau_E = \frac{U}{P_{losses}} \tag{1.21}$$

,through the reactor boundary. To maintain steady-state conditions, these losses must be compensated, in addition to the alpha heating

$$S_\alpha = n_D n_T \langle \sigma v \rangle E_\alpha = \frac{1}{4} n^2 \langle \sigma v \rangle E_\alpha \tag{1.22}$$

where $E_\alpha = 3.5 MeV$, by proper external heating S_h.

The ultimate goal would be the *ignition condition*, i.e. the situation where, in a steady-state regime, the heating provided by alpha particles is sufficient to offset the combined losses from Bremsstrahlung and thermal conduction, eliminating the need for external power input:

$$S_\alpha = S_B + S_\kappa \tag{1.23}$$

From equation 1.23, the **Lawson criterion** ([16], [17]) can be retrieved, resulting in:

$$n\tau_E \geq \frac{12T}{\langle \sigma v \rangle E_\alpha - 4 \cdot C_B \sqrt{T}} \approx 2 \cdot 10^{14}\ cm^{-3}s \tag{1.24}$$

where $n\tau_E$ is named the Lawson parameter.

Current reactor designs are expected to achieve low confinement times. This can be increased through size, which is expensive. Consequently, ignition would require high densities, hence large fuel pressures ($p = nT$). However, maintaining effective fuel confinement becomes increasingly challenging and costly as pressure rises. As a result, it is unlikely that the first generation of reactors will operate in ignition mode. Consequently, some level of external heating will still be necessary to sustain the reactor in a steady-state condition.

Assume that a combination of alpha heating and external power input sustains the plasma in a steady-state equilibrium. The key objective is to maximize the ratio of output power to input power (that is, gain) to determine the conditions under which the system is viable as a power reactor. The first one, Q, based primarily on physics considerations

$$Q = \frac{net\ thermal\ power\ output}{heating\ power\ input} \tag{1.25}$$

while the second one based on some basic engineering constraints

$$Q_E = \frac{net\ electric\ power\ output}{electric\ power\ input} \tag{1.26}$$

The gain parameter Q is essentially telling us the net thermal power produced by the plasma as a result of the physics of the fusion process. Anyway, the engineering factor Q_E is of commercial importance, which converts all contributions to electric power densities by the introduction of appropriate power conversion efficiencies. Obviously, the condition required by a fusion reactor is to have $Q_E > 1$.

1.2.4 Magnetic confinement

Because, at such extremely high temperatures, hydrogen gas is transformed into a mix of independently moving positively charged ions and negatively charged electrons—the so-called plasma state (section 1.2.1)—strong magnetic fields can be used to keep this plasma sufficiently far away from the wall.

A charged particle in a strong magnetic field is confined by the magnetic field lines due to the Lorentz force. In a straight and uniform magnetic field, it travels along a helical path around a field line. Assumed the magnetic field to be aligned along the x direction, a charged particle subjected to such a field exhibits significantly different behavior along $\vec{B}$ in the x-direction (referred to as the parallel direction) compared to the *yz-plane* (referred to as the perpendicular plane). In the parallel direction, the magnetic field does not exert any force. Consequently, the motion of a particle with charge e and mass m along the x-direction is simply:

$$x = x_0 + v_x t \tag{1.27}$$

with x_0 the location x at time $t = 0$ and v_x the constant velocity along the magnetic field.

Instead, in the perpendicular plane there will be the effect of the *Lorentz force* due to the presence of the magnetic field as:

$$\vec{F} = m\frac{d\vec{v}}{dt} = e\vec{v} \times \vec{B} \tag{1.28}$$

which will lead the charged particle to have a circular path. From the latter, a motion on the *yz-plane* will result as:

$$y = y_g + \rho_L sin(\omega_L t + \Phi) \tag{1.29}$$

$$z = z_g + \rho_L cos(\omega_L t + \Phi) \tag{1.30}$$

where

$$\omega_L = \frac{eZB}{m} \tag{1.31}$$

is the gyration frequency and

$$\rho_L = \frac{mv_\perp}{eZB} \tag{1.32}$$

is the Larmor radius, with $v_\perp$ the magnitude of the velocity in the plane perpendicular to the magnetic field and Φ is the angular position of the particle at time 0. The typical path of a particle along a field line can be displayed as in figure 1.5.

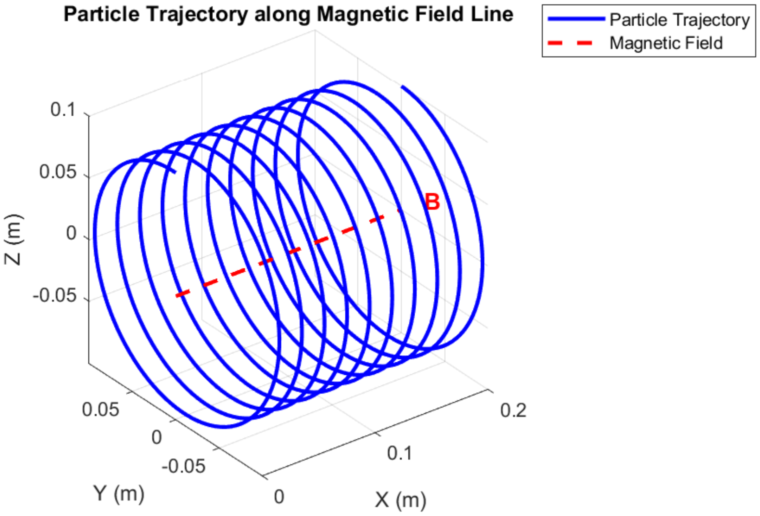

Figure 1.5: Charged particle trajectory along a straight field line B

From equations 1.29 and 1.30 the velocity components in the *yz-plane* can be retrieved [18].

Particles will tipically have a velocity in the *yz-plane* comparable to the thermal speed $v_\perp \approx \sqrt{T/m}$ resulting in a Larmor radius

$$\rho_L \approx \frac{1}{\omega_L}\sqrt{\frac{T}{m}} \propto \frac{1}{B}\sqrt{\frac{T}{m}} \tag{1.33}$$

Now, let's consider L, the *connection length*, i.e. the typical parallel-to-B distance that a particle has to travel in the Scrape-Off Layer (see section 3) before striking the divertor target.

If the magnetic field is strong enough it will result in:

$$\frac{\rho_L}{L} << 1 \tag{1.34}$$

which implies that most of the particles will be prevented to reach the solid walls.

Since an electron is much lighter than an ion, it rotates much faster but with a significantly smaller Larmor radius. In a fusion reactor, the magnetic field strength is selected so that the ions' gyration radii are much smaller than the device's dimensions.

The simplest magnetic field geometry for plasma confinement is a straight cylinder. However, this setup has the drawback that plasma particles escape from both ends. This loss can be significantly reduced by creating two "magnetic mirrors", achieved by increasing the field strength at both ends with additional magnetic coils. However, effective confinement could never be achieved in such machines, primarily due to instabilities caused by particle losses at the ends. In fact, the end mirrors only reflect particles with a sufficiently large perpendicular velocity component $v_\perp$. Moreover, particles with velocities primarily aligned with the magnetic field lines are not stopped by the end mirrors and therefore escape. As a result, the particle population confined within the mirror becomes depleted of particles with small perpendicular velocities.

The obvious solution to prevent end losses is to bend the cylindrical configuration into itself, forming a **toroidal** shape. The required toroidal magnetic field is generated by winding coils (toroidal field coils) around the toroidal vacuum chamber. However, this coil arrangement creates a magnetic field that is stronger near the vertical symmetry axis of the machine, where the coils are closer together, compared to the outer part of the torus. This results in a vertical drift of particles (as in Figure 1.6), leading to charge density buildup and plasma loss. This drift can be counteracted—and all particles can be confined—if the magnetic field lines, instead of forming simple circular loops as in the previously discussed configuration, are wound around the torus in such a way that the drift in the outer part of the trajectory is balanced by the drift in the inner part.

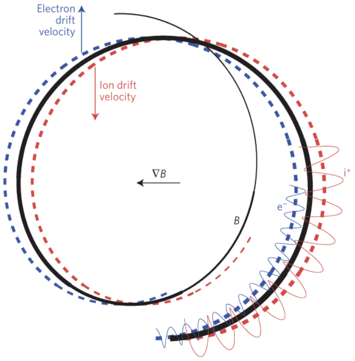

Figure 1.6: Particle trajectory in a helical magnetic field [2]

The *tokamak* [19] configuration (Fig. 1.7a) seems to be, nowadays, the most promising and reliable magnetic confinement device able to achieve stable fusion reactions in order to effectively produce energy. In this device, the toroidal current flowing in the plasma is induced by the central transformer by varying the magnetic flux. This results in an inductive voltage along the plasma torus. This voltage drives the plasma current and this is why the tokamak works in pulsed operation. Due to the electrical resistance of the plasma loop, the current leads to ohmic power dissipation, following the law $P = R_p I_p$, where R_p and I_p are the plasma resistance and current respectively, which contributes to heating the plasma. In addition to the previously mentioned toroidal field coils that generate the toroidal magnetic field B_ϕ, the main contributor of the total magnetic field $\mathbf{B}$, *poloidal* coils are integrated to generate a poloidal field B_θ. These coils are essential for counteracting the expansion forces caused by the plasma current loop and plasma pressure. In addition, they help shape the plasma and can also be used to create a divertor (Section 1.3). The combination of these two magnetic fields

$$\mathbf{B} = \mathbf{B}_\phi + \mathbf{B}_\theta \tag{1.35}$$

results in a helical magnetic field within the chamber (Fig. 1.6). For a tokamak the previously mentioned connection length L can be defined as $L \approx \pi R q$, where q is the *safety factor* defined as:

$$q \approx \frac{r B_\phi}{R B_\theta} \tag{1.36}$$

where r is the minor radius of any particular flux surface and R is the major radius of the torus. The safety factor represents the number of toroidal turns for a particle to reach the exact poloidal location from where it started. In the confined plasma, the principal significance of the safety factor q is that the plasma is magnetohydrodynamically unstable if $q \leq 2$.

Alternatively, the *stellarator* [20], figure 1.7b, is a fusion device designed for continuous operation, i.e. the plasma is sustained indefinitely without interruptions, which would be more easily achieved if the need for a pulsed plasma current, as in the tokamak, were eliminated. This concept offers such a solution by using external currents to generate the helical magnetic configuration. In its simplest form, additional helical coils surrounding the toroidal plasma introduce the necessary twist to the toroidal magnetic field produced by the main field coils. However, these helical windings around the plasma ring add complexity to the stellarator's construction. Early stellarator designs suffered from poor confinement properties, but modern stellarators have improved confinement through an advanced and intricate set of coils.

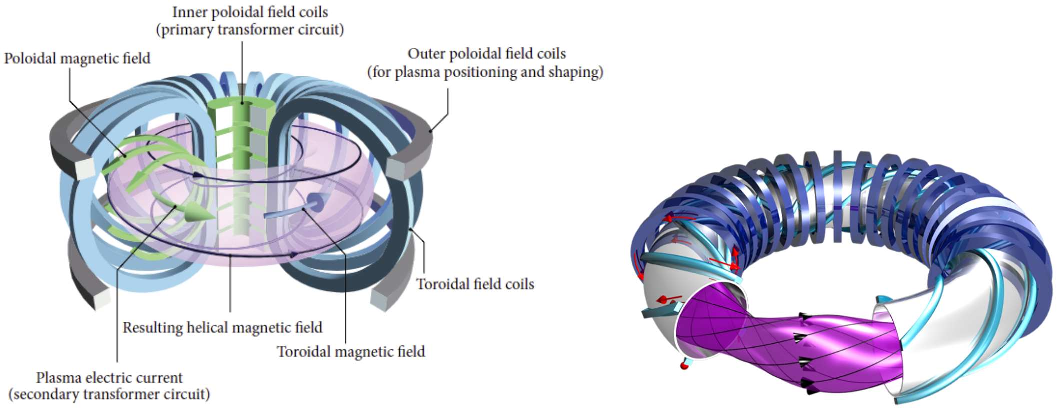
Inner poloidal field coils
(primary transformer circuit)
Poloidal magnetic field
Outer poloidal field coils
(for plasma positioning and shaping)
Toroidal field coils
Resulting helical magnetic field
Toroidal magnetic field
Plasma electric current
(secondary transformer circuit)

(a) Tokamak [21]

(b) Stellarator (*source: ipp.mpg.de*)

Figure 1.7: Sketch of the two main magnetic confinement devices

1.3 The Power Exhaust challenge

One of the primary challenges in making fusion energy commercially viable is the effective management of *power exhaust* [22]. The substantial heat generated within the plasma must be efficiently removed to maintain stable temperature and pressure conditions. Failure to do so poses a significant threat to the internal components that are directly exposed to the plasma, known as *Plasma-Facing Components* (PFCs). These include the *first wall* — the inner surface of the vacuum vessel — and structures like limiters and divertors, which are designed to handle heat dissipation within the reactor. Efficiently managing the intense heat and particle fluxes generated during fusion reactions is essential to prevent damage to these critical components and to ensure the sustained operation of fusion reactors. Additionally, it's crucial to minimize the release of impurities from the reactor walls during the exhaust process, as these can migrate into the plasma core and potentially inhibit fusion reactions. Developing materials and technologies capable of withstanding these extreme conditions while minimizing impurity generation remains a significant focus in fusion research.

One of the earliest and simplest plasma-facing components studied in tokamak reactors to control plasma interaction with the walls and dissipate heat loads was the **limiter** configuration (Fig. 1.8a) [23]. In this setup, a specially designed structure extends into the plasma, ensuring that the outermost magnetic field lines connect the two faces of the limiter, concentrating particle-surface interactions in this region. The structure's geometry is optimized to achieve an almost parallel incidence of the magnetic field at the limiter's top, thereby reducing particle fluxes on its surface. This design minimizes erosion, which is directly linked to flux strength and incidence angle. However, a significant drawback is that the plasma-wall interaction area directly faces the core plasma, allowing impurities eroded from the limiter to easily diffuse into the main plasma and potentially affect reactor behavior.

To address this last problem, the choice of the **divertor** in the last years is the favorite [24] [25]. With the addition of external poloidal conductors there can be the creation of magnetic field nulls, known as **X-point**, which aids to divert the open magnetic field lines towards the divertor volume and the target plates. The line which has the X-point is called the *separatrix*, that is the equivalent of the last closed magnetic surface for the limiter. The region outside the separatrix is called Scrape Off Layer (SOL). The most popular divertor configuration right now is the Lower Single Null (LSN) as can be seen in Fig. 1.8b, while many other newer alternative configurations can be appreciated in [26], [27]. In between the two legs directed to the targets, this region is named *private flux region* (PFR), while the rest of the SOL is called the *common flux region* (CFR). In the regions beyond the closed-flux surfaces, open magnetic field lines connect to wall elements, leading to strong localization of heat and particle fluxes. Any plasma particle escaping the confinement region follows these open field lines directly to the wall. To manage this, magnetic field topologies are designed to guide open field lines toward remote areas that are far enough from the confined plasma and equipped with high-heat-flux targets capable of withstanding extreme thermal and particle loads. However, even with these measures, handling the heat loads at the divertor targets remains a significant challenge, as current materials are unable to sustain such high heat fluxes indefinitely.

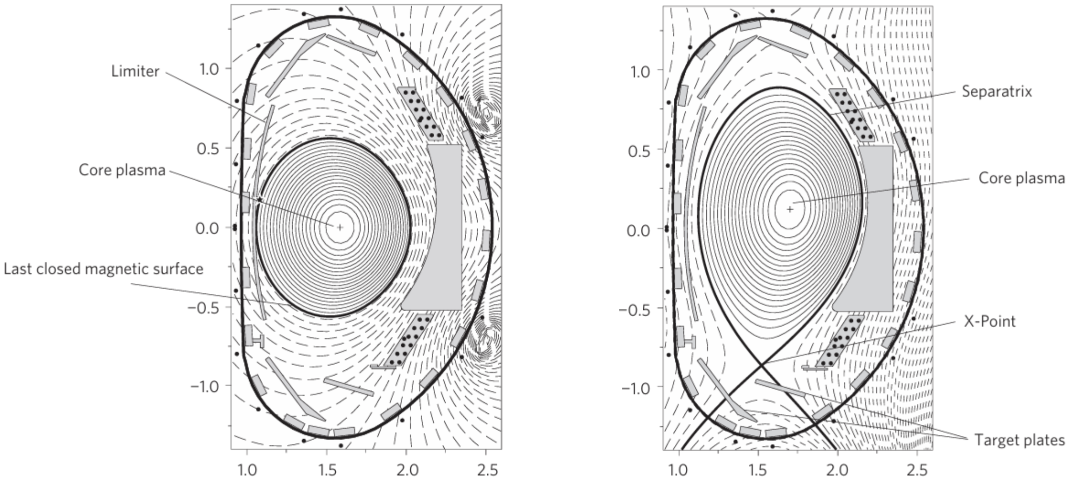

(a) Limiter

(b) Divertor

Figure 1.8: Different ways to bring the plasma edge in contact with the wall, taken from [2]

The selection of materials for plasma-facing components is crucial, as it directly impacts heat and particle exhaust, as well as plasma transport properties. Two key requirements must be balanced:

1. the erosion of materials must be minimized to ensure a sufficiently long lifetime for highly exposed components
2. plasma contamination due to impurities—resulting from wall erosion and plasma transport—must be kept at levels that do not disrupt fusion reactions

Specifically, impurity radiation losses in the plasma core and dilution of the fuel must remain low enough to maintain stable plasma burning. At the same time, substantial radiation in the plasma periphery is desirable to help manage power exhaust. Historically, carbon was widely used as a first-wall material in fusion experiments due to its resistance to melting, relatively high sublimation temperature, and excellent thermal conductivity. Additionally, in high-temperature fusion plasmas, carbon impurities become fully ionized, reducing their radiative impact. However, carbon chemically interacts with hydrogen plasmas, leading to high erosion rates and the formation of hydrocarbon compounds that redeposit throughout the plasma chamber. In the presence of tritium, this results in an unacceptable accumulation of radioactive material inside the reactor vessel. Molybdenum was one of the first heavy metals successfully used as a plasma-facing material. Today, tungsten [28] is considered the most promising candidate for fusion power plants due to its superior resistance to heat and erosion and a low retention of hydrogen isotopes.

1.3.1 The detachment

As a main solution for the power and particle exhaust challenge mentioned in the previous section has been identified the *detached* regime. Firsts experiments to try to reduce the divertor heat flux were carried in the mid '90s on many experimental fusion reactors. These were successful, with increased divertor radiation through additional gas fueling to raise density and lower divertor plasma pressure.

The Scrape-Off Layer parallel transport strongly depends on plasma collisionality and at higher plasma collisionality, a low temperature highly radiative divertor regime sets in, the **detachment** ([29],[30]). This regime sets when the plasma flowing to divertor plates looses energy through radiation and dissipative processes, and momentum through charge exchange, inelastic collisions and recombination. This leads to plasma neutralization and detachment from the target plate, and as a result, significantly reduced heat load and material erosion. This regime is characterized by a parallel SOL electron pressure drop, high neutral divertor pressure, low plasma temperature and high electron density at the divertor plate, leading to high impurity radiation.

The radiative loss power of an impurity species can be determined using a collisional–radiative model, based on rate coefficients for ionization, recombination, and line excitation. In figure 1.9, the total radiative loss parameter for different kind of impurities is shown. the loss of power is the sum of the emission of individual spectral lines and continuum emission. It depends on the electron temperature because the radiation process is driven by ion-electron collisions, which, in turn, are influenced by the relative velocity of ion-electron encounters.

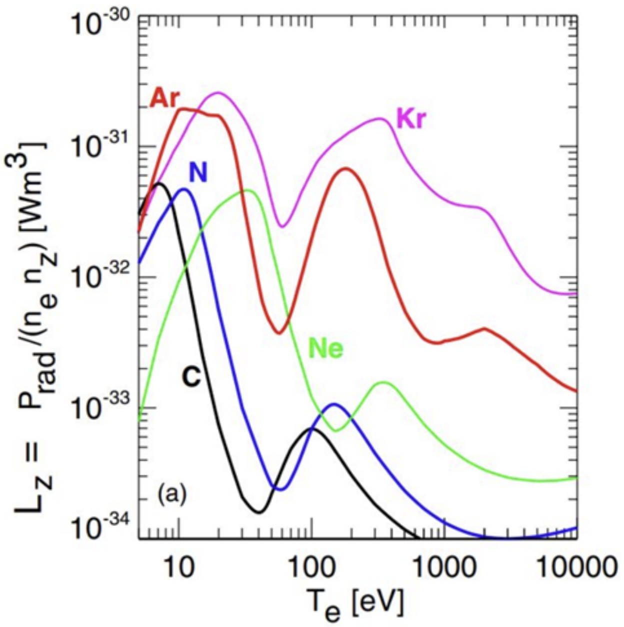

Figure 1.9: Radiative loss parameter L_z from ADAS, as the sum of line radiation, recombination-induced radiation and bremsstrahlung (from [3])

The power radiated by an impurity can then be described as:

$$P_{rad} = n_e n_z L_z(T_e) \tag{1.37}$$

where n_z is the density of an impurity with atomic number Z.

In tokamaks with low-Z plasma-facing components (as the TCV, section 1.4), such as carbon, intrinsic impurities generally play a significant role in radiative losses and impurity influx is mainly driven by physical sputtering during low-density attached divertor conditions. However, in high-density detached operation, where T_e falls below the physical sputtering threshold, impurity influx is predominantly governed by chemical sputtering in regions with high ion flux ([31]). After the PFC changeover to tungsten, i.e. a high Z material, injection of low Z impurities, typically nitrogen or neon, is used to produce sufficient radiation to achieve divertor detachment. While the physical processes of divertor detachment remain similar, the dynamics and control of detachment can differ significantly between tokamaks with intrinsic impurities from low-Z PFCs and those with high-Z PFCs that require impurity injection.

Moreover, detached plasmas typically show a reduction in ion flux to the divertor target. This reduction is important not only for minimizing target erosion but also for lowering surface heat flux through atomic and molecular recombination of the ionization potential. The reduction of ion flux with divertor detachment can be quantified as *degree of detachment* (see [32]):

$$DOD \equiv \frac{C_0 n_{e,sep}^2}{\Gamma_i} \tag{1.38}$$

where C_0 is a normalization constant obtained experimentally, $n_{e,sep}$ is the electron density at the separatrix and Γ_i is the ion flux. The onset of divertor detachment in tokamaks is often identified as the point where the divertor ion flux rolls over and begins to decrease.

1.4 TCV tokamak

In order to support experimental reactors like **ITER** that are currently under construction, the TCV Tokamak (*Tokamak à Configuration Variable*) is still working to understand the physics of nuclear fusion by magnetic confinement. It is also exploring new and alternative avenues in anticipation of future prototype power plants like **DEMO**. The TCV tokamak's goal is to create new plasma shapes and configurations by using its highly specialized plasma shaping capability. A variety of heating and current drive systems are also offered via high power neutral beam heating and strong microwave electron heating. These extremely adaptable features, along with ongoing improvements to a real-time control system and the development and modernization of measuring systems (diagnostics), make TCV a great tool for studying the physics of magnetically confined plasmas.

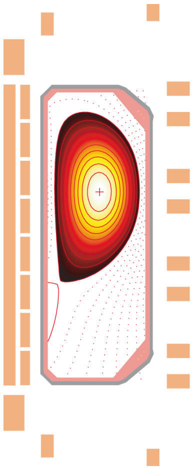

Figure 1.10: Poloidal section of TCV (*source: epfl.ch*)

TCV is a carbon walled, medium sized (major plasma radius $R_0 = 0.88$ m and minor plasma radius $r_0 = 0.25$ m, magnetic field $B_0 < 1.5$ T from *epfl.ch*), conventional aspect ratio tokamak with unique shaping capabilities. It is characterized by a highly elongated, rectangular vacuum vessel and by 16 poloidal coils for plasma shaping equally shared out into two stacks located on both sides of the vacuum vessel as shown on the figure. The coil represented by a long vertical rectangle (figure 1.10) is the 'OH-coil'. It is used to inductively drive current into the plasma.

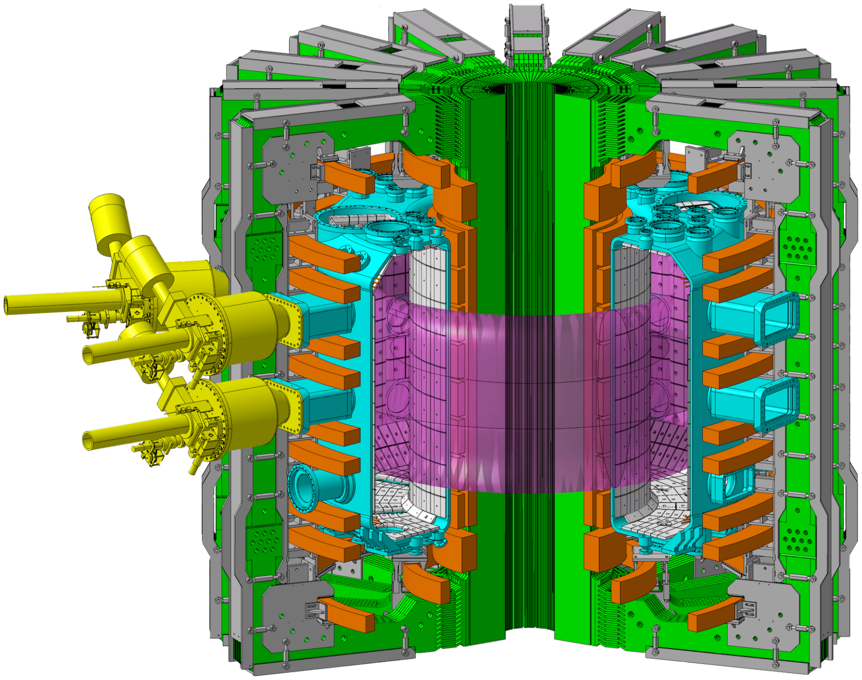

Figure 1.11: TCV tokamak (*source: epfl.ch*)

1.4.1 Divertor upgrade

In the last years the *TCV divertor upgrade* [33] started its operations [34]. As mentioned in [35], the divertor upgrade is centred around the installation of removable gas *baffles* that partially separate the vessel into main and divertor chambers. The main goal of the baffles is to diminish the transit of recycling neutrals to closed flux surfaces, permitting an increased divertor region density, thereby enhancing volumetric losses in the divertor volume, to raise the divertor neutral pressure, which will make it easier to extrapolate to devices like ITER [36] in the future that will need a high divertor neutral pressure. The edge transport code SOLPS-ITER, which uses a fluid description of the plasma combined with kinetic neutrals, was used to optimize the divertor closure in [37] of a first set of baffles for a significant neutral compression in a traditional, *single-null divertor*. Standard wall protection tiles are replaced by graphite tiles for the baffles, which may be installed and removed with just brief manual entry. Simulation results show the average main chamber neutral density decreases by a factor of around 2 to 3 when the baffles are fitted, whereas the equivalent divertor neutral density rises by a factor 5. Due to the latter, an increase of target density can be noticed that leads to a reduction of the ionisation mean free path ($\lambda_{ion} \propto 1/n_e$) and an enhanced ionisation. Moreover, simulations of the baffled divertor show an upstream temperature unaffected compared to the unbaffled case, indicating that properties of the main plasma are largely unaffected by the baffles.

A brand new layout, the tightly baffled long legged divertor (TBLLD), has been studied recently on TCV through the SOLPS-ITER code. Its aim is to increase the connection length in order to decrease the target temperature. Further analysis have been performed in [38].

1.5 Aim of the thesis

The primary goal of this project is to model and analyze the transport of energy by electrons and ions in the TCV (section 1.11) plasma and its exchange between them, specifically in the outer core and in the Scrape-Off Layer (SOL, section 2.2.1) regions, using the SOLPS-ITER code (section 3.2). Moreover, it is of interest the behavior of the ions in the Scrape-Off Layer, since they are hotter than ions going towards the last flux surface [39] even if they have less power in the core. This is confirmed and consistent in both simulations and experiments on TCV. Another question that arises is, why the transfer of power from ions to electrons is not enough to equalize their temperatures, i.e. there is weak electron-ion thermal coupling at the edge of the tokamak.

Some interesting results can be found in [40], which presents a quantitative test of SOLPS-ITER simulations against TCV L-mode (Low confinement mode, characterized by relatively low energy confinement) experiments. Differently from what will be performed in this thesis work, these simulations account for drifts which affect significantly the cross-field transport. What has been noticed is that there are some big discrepancies between simulations and experiments in the outer divertor region. Firstly, the simulated ion temperature T_i appears to be underestimated, but both simulations and experiments consistently find an ion temperature that exceeds the electron temperature, $T_i^u > T_e^u$. Furthermore, Langmuir probes [41] measurements indicate that the simulations overestimate the target electron density n_e^t and underestimate the target electron temperature T_e^t. Also, the simulated divertor neutral pressure p_n^{div} exceeds the measured value by factor $\sim$4.

The present work focuses on the scan of some parameters or boundary conditions that greatly affect the power balance and power transport in the balance equations present in the code. This with the aim to enhance the understanding of plasma-wall interactions and the energy transport mechanisms in the SOL, which is a key aspect to improve the understanding of power exhaust, which is crucial for managing the heat load on reactor components and ensuring efficient operation, thus ensuring the longevity and safety of the reactor components.

2. Edge plasma physics

2.1 Plasma transport

A significant complexity arises when analyzing plasma as a macroscopic system, particularly regarding the transport of energy, momentum, and particles. When considering only binary collisions and assuming small deviations from thermodynamic equilibrium, plasma transport theory naturally extends the well-established kinetic transport theory of standard gases. However, it also accounts for the influence of collective effects on charged particles due to external electromagnetic fields. In this context, the transport is described by *classical transport theory* [42].

As already said in section 1.2.4, the charged particles follow the direction parallel to the magnetic field lines with a gap equal to the Larmor radius in the plane perpendicular to the field lines. However, in reality collisions can move the particles from one unperturbed orbit to another with the effect to transport both particles and energy. This makes the transport to be completely anisotropic with respect to the direction of the magnetic field. Thus, parallel transport is slowed down by collisions whereas perpendicular transport needs collisions. This transport across the flux surfaces can be described by a diffusion approximation:

$$\Gamma_j = -D_j \nabla n_j \tag{2.1}$$

where D_j is the *diffusion coefficient* for the species *j*. This is the well known *Fick's law*, which is saying us that particles diffuse down along the density gradient. Then, if we see the movement of a particle as a general *random walk*, it will undergo a number N of statistically independent steps of size Δl. The diffusion coefficient is defined as the product of the square of the step size times the frequency, resulting in:

$$D^{classic} \cong \Delta l^2 \nu \tag{2.2}$$

where ν is the collision frequency, i.e. the inverse of the characteristic time between collisions.

The classical transport theory found a relation for the perpendicular diffusion coefficient with some important plasma parameters

$$D_{\perp}^{classic} \propto B^{-2} T_e^{-1/2} \tag{2.3}$$

which would be positive, since by producing large magnetic fields B and by heating the plasma it would have been possible to achieve optimal confinement. Anyway, these predictions were proved wrong from experiments [43], where it has been found that

$$D_{\perp}^{exp} \simeq 1\ m^2/s >> D_{\perp}^{classic} \simeq 5 \times 10^{-5}\ m^2/s \tag{2.4}$$

So, classical transport theory provides reasonably accurate approximations for the parallel diffusion coefficient $D_{\parallel}$ while it fails in the estimations of the perpendicular diffusion coefficient $D_{\perp}$, which requires a more precise description. This leads to the *neo-classical transport theory* ([44], [45]). Even if this theory retrieve much larger values of the cross-field diffusion coefficient, it is still far off the experimental behavior

$$D_{\perp}^{neo-cl} \simeq 60 D_{\perp}^{classic} << D_{\perp}^{exp} \tag{2.5}$$

This is due to the turbulent fluctuations arising from the various micro-instabilities [46], i.e. instabilities which have wave lengths that are comparable to the ion or electron Larmor radii, such as drift waves [47] or pressure gradient driven ballooning mode [48], causing perturbations in the guiding centers of the particles orbits. In this case, we are talking about *anomalous transport theory* [49]. A rough estimate of the turbulent diffusion coefficient, assuming the step size Δl to be comparable to the ion thermal Larmor radius, can be obtained - the gyro-reduced Bohm ([47]) scaling:

$$D_{\perp}^{AN} \approx \rho_L^2 \frac{v_{th}}{a} \approx \frac{\rho_L^2}{a} \frac{T}{qB} \tag{2.6}$$

where a is the minor radius of the device.

The anomalous transport is still not entirely understood, although it is associated to the effect of the plasma turbulence originated from the unstable electromagnetic waves and oscillations in the plasma, and it is one of the greatest challenges in theoretical plasma physics.

2.1.1 Drifts effect

A great contribution to the turbulence and cross-field transport is given by *drifts*, that influence the classical trajectory of the charged particles due to forces acting in the plasma. As we have already seen, equation (1.2.4) describes the motion of a charged particle. Considering also the presence of an external force it will result in

$$m\frac{d\mathbf{v}}{dt} = q\mathbf{v} \times \mathbf{B} + \mathbf{F} \tag{2.7}$$

In particular, we focus to the component perpendicular to field lines, contributing to the cross-field transport. Associating the velocity $\mathbf{v}$ to the laboratory reference frame, changing this last will lead to define the *relative velocity* $\mathbf{w}$=$\mathbf{v}$-$\mathbf{v_g}$, where $\mathbf{v_g}$ is the velocity of the guiding center reference frame

$$m\frac{d\mathbf{w}}{dt} = q(\mathbf{w} + \mathbf{v_g}) \times \mathbf{B} + \mathbf{F}_{\perp} = q\mathbf{w} \times \mathbf{B} + q\mathbf{v_g} \times \mathbf{B} + \mathbf{F}_{\perp} \tag{2.8}$$

where the second term of the RHS of the equations has to be equal to 0

$$\mathbf{v_g} = \frac{\mathbf{F}_{\perp} \times \mathbf{B}}{qB^2} \tag{2.9}$$

Thus, the guiding-center motion is perpendicular to both the magnetic field and the external force. Some of the forces that could cause drift on the plasma particles are shown hereafter.

$\mathbf{E} \times \mathbf{B}$ drift

In the presence of a perpendicular electric field, this will exert a force on the charged particles $\mathbf{F}_{\perp} = q\mathbf{E}_{\perp}$

$$\mathbf{v}_{\mathbf{E}\times\mathbf{B}} = \frac{\mathbf{E}_{\perp} \times \mathbf{B}}{B^2} \tag{2.10}$$

This has the effect to accelerate the particle on one side of the orbit, while decelerating on the other, resulting in a net drift of the trajectory (displayed in figure 8.5 of [15]).

∇B drift

Modifications of the gyromotion may arise also from inhomogeneities in the fields. In particular, the magnetic field gradient produces particle drift perpendicular to both $\mathbf{B}$ and ∇B. Defining the magnetic moment of particles

$$\mu = \frac{mv_\perp^2}{2B} \tag{2.11}$$

related to the gyromotion of the particles is subject to the force $\mathbf{F}_{\nabla B} = -\mu \nabla_\perp B = -\frac{mv_\perp^2}{2} \nabla_\perp lnB$, which gives

$$\mathbf{v}_{\nabla B} = \frac{mv_\perp^2}{2q} \frac{\mathbf{B} \times \nabla B}{B^3} \tag{2.12}$$

Knowing that $B_\phi \propto 1/R$ in a tokamak, this drift will be vertically directed. A better sketch can be seen in figure 8.7 of [15].

Curvature drift

Field line curvature leads to a new guiding center drift perpendicular to both the magnetic field and the curvature vector. The drift is induced by the centrifugal force experienced by a particle as it freely streams along a curved magnetic field line. This force can be defined as $\mathbf{F_c} = -mv_\parallel^2/R_c\mathbf{k}$ where $\mathbf{k} = \mathbf{R_c}/R_c$ is the radial versor pointing outside of the curve and R_c is the radius of the curvature vector. Going through several passages, it results that $\mathbf{b} \cdot \nabla \mathbf{b} = -\mathbf{R_c}/R_c^2$, where $\mathbf{b} = \mathbf{B}/B$. Thus, the curvature drift velocity results as

$$\mathbf{v}_\kappa = \frac{v_\parallel^2}{\omega_L} \frac{\mathbf{R_c} \times \mathbf{B}}{R_c^2 B} = \frac{mv_\parallel^2}{q} \frac{\mathbf{B} \times \nabla B}{B^3} \tag{2.13}$$

As can be noticed, the curvature drift has the same direction of the ∇B drift and could be combined in a single expression.

Polarization drift

Drifts can also be induced by time-varying electric and magnetic fields. One of the main consequences of this time dependence is the emergence of a new guiding center drift, known as polarization drift. This drift results from the effects of particle inertia in response to a time-dependent perpendicular electric field. As $\mathbf{E}_\perp$ changes slowly over time, the particle motion follows the field's evolution but lags slightly due to inertia. Analysis shows that the resulting polarization drift is directed along $\mathbf{E}_\perp$ and is more pronounced for ions than for electrons, due to the greater mass of ions. In a constant B field with a slowly varying perpendicular electric field

$$\mathbf{v_p} = \frac{1}{\omega_L B} \frac{d\mathbf{E}_\perp}{dt} \tag{2.14}$$

A good physical picture is given in picture 8.10 of [15], where we can see the combined effect with the $\mathbf{E} \times \mathbf{B}$ drift.

The final expression for the cross-field velocity can be written as

$$\mathbf{v}_\perp = \mathbf{v_{gyro}} + \mathbf{v_{E \times B}} + \mathbf{v}_{\nabla B} + \mathbf{v}_\kappa + \mathbf{v_p} \tag{2.15}$$

where the contribution of the gravitational force has been neglected due to its small impact.

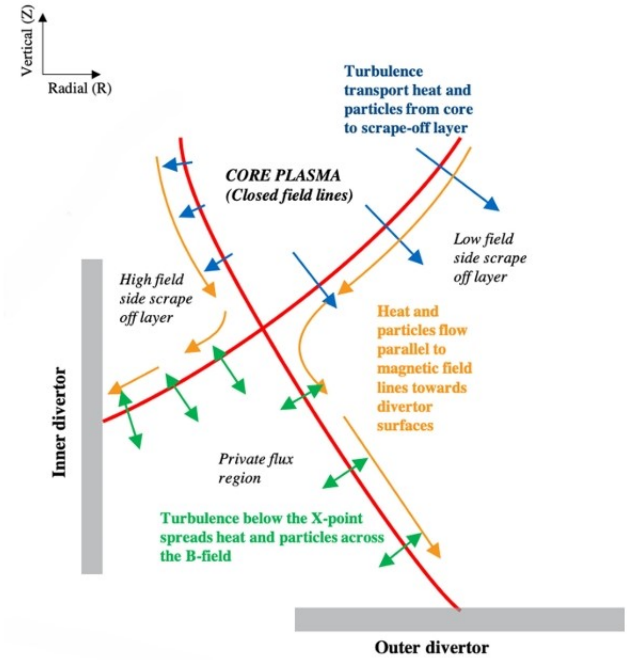
Vertical (Z)
Radial (R)
Turbulence transport heat and particles from core to scrape-off layer
CORE PLASMA (Closed field lines)
Low field side scrape off layer
High field side scrape off layer
Heat and particles flow parallel to magnetic field lines towards divertor surfaces
Inner divertor
Private flux region
Turbulence below the X-point spreads heat and particles across the B-field
Outer divertor

Figure 2.1: Turbulent and parallel transport processes in the divertor volume, taken from [4]

Moreover, unlike the guiding-center drifts discussed earlier, which cause direct displacements of particle guiding centers, there is the *diamagnetic drift* which is a fluid drift that occurs in magnetized plasmas in the presence of a pressure gradient ∇p [50] and won't be discussed further.

2.2 Physics of the Scrape Off Layer

2.2.1 The Scrape Off Layer

In a fusion reactor, the solid surface acts as an effective sink for plasma. It is not a mass sink, however, since the particles are subsequently released as neutrals. Since they are typically not firmly bonded to surfaces, the neutral atoms that are produced are thermally re-emitted back into the plasma, where they can be re-ionized typically by electron impact. When recombined neutrals re-enter the plasma at the same rate as plasma charged pairs are lost to the surface, a steady-state condition known as **recycling** occurs.

In a *tokamak*, due to the presence of the toroidal magnetic field, the rate at which electrons and ions are falling towards the wall is reduced, making the plasma magnetically confined. Charged particles diffuse very slowly across magnetic fields, compared with their unrestricted motion along **B**, which tends to be at velocities of order of the sound speed. The radial diffusion of particles from main plasma (i.e. outboard of the last closed flux surface, LCFS) to the wall leads to a much less dense and cooler environment which can be identified as the *Scrape Off Layer*. Cross field velocities can be retrieved from equation (2.1) and are of the order:

$$v_\perp \simeq D_\perp/\ell_\perp \tag{2.16}$$

where $D_\perp$ is the cross-field diffusion coefficient $[m^2 s^{-1}]$ and $\ell_\perp$ is the characteristic radial scale length of density [m]. The particle flux density in the perpendicular direction is expressed by equation (2.1) and can be re-written as $\Gamma_\perp \equiv nv_\perp$. While $v_\perp$ is slow, $v_\parallel \approx$ to the plasma sound speed:

$$c_s = \left[\frac{(T_e + T_i)}{(m_e + m_i)}\right]^{1/2} \approx \left[\frac{(T_e + T_i)}{(m_i)}\right]^{1/2} \tag{2.17}$$

because the ion mass is much larger than the electron mass.

In the case of a divertor, an external conductor carrying a current in the same direction of the plasma current is used, producing a point where the two current centres a null in the poloidal field (Single Null), named the *X-point.* The magnetic flux surface passing through the X-point is called the magnetic *separatrix.* The region below the X-point and inside the separatrix is called the *private plasma.* Power and plasma particle transport from the main SOL over the private plasma separatrix sustain it.

The self-collisional mean free paths in the high-collisional SOL can be defined as:

$$\lambda_{ee} \approx \lambda_{ii} \approx \frac{10^{16}T^2}{n_e} \tag{2.18}$$

The collisionality plays a crucial role in determining whether a full kinetic analysis is necessary or if a fluid analysis of the plasma behavior is sufficient. Kinetic analysis computes the full velocity distribution of the plasma particles at each spatial (and temporal) location. One settles for merely computing the average quantities at each location in space (and time) in fluid analysis, such as the average (thus "fluid") velocity. Kinetic analysis is obviously much more difficult to perform than fluid analysis, and the interest is about determining when the latter is likely to be sufficient. It turns out that when collisionality is strong, the so-called fluid approximation is probably adequate (section 2.2.2).

2.2.2 Fluid Model - Braginskii equations

The way to describe the transport phenomena within a fluid ([51]) is done by the *transport equation*, which describes how a scalar quantity is transported. This can be written, for the scalar φ, as

$$\frac{\partial \varphi}{\partial t} = \nabla \cdot \mathbf{v}\varphi - \nabla \cdot \Gamma \nabla \varphi + S \tag{2.19}$$

where the first term in the RHS represents the convection and the second term the diffusion. While, S is the source term and $\mathbf{v}$ is the velocity of the fluid.

The state of an ionized gas, e.g. plasma (section 1.2.1), is much more complex and can be defined by the distribution functions $f_s(\mathbf{r}, \mathbf{v}, t)$ that characterize each particle type within it. These functions specify the density of particles of species s at time t and at the position $\mathbf{r}, \mathbf{v}$ in phase space. Here, $f_s(\mathbf{r}, \mathbf{v}, t)d\mathbf{r}d\mathbf{v}$ represents the number of particles in a six-dimensional volume element $d\mathbf{r}d\mathbf{v}$. In the simplest scenario, the plasma consists of electrons and a single ion species, but in more complex cases, it may include multiple ion species along with neutral particles like atoms, molecules, excited atoms, and others. The dynamics of the ionized gas are governed by a system of kinetic equations, which evolve the distribution functions over time. In this case, the *Fokker-Planck* kinetic equation is considered:

$$\frac{\partial f_s}{\partial t} + \nabla \cdot (\mathbf{v} f_s) + \nabla_v \cdot \left[\frac{\mathbf{F_s}}{m_s} f_s\right] = \sum_{s'} C_{ss'}[f_s, f_{s'}]. \tag{2.20}$$

where $C_{ss'}$ is the collisional term between the species s and s' and $\mathbf{F_s}$ is the Lorentz force due to the electromagnetic fields

$$\mathbf{F_s} = Z_s e(\mathbf{E} + \mathbf{v} \times \mathbf{B}) \tag{2.21}$$

where Z_s is the atomic number of the species and e is the electric charge.

A result of statistical mechanics is that the distribution function characterizing the molecules of a gas in thermal equilibrium should be the so called Maxwell-Boltzmann distribution:

$$f^0(\mathbf{v}) = n\left(\frac{m}{2T\pi}\right)^{3/2} e^{-\frac{mv^2}{2T}} \tag{2.22}$$

But, if we are interested in changes occurring in time intervals greater than the collision time, the solution of the kinetic equation will be a *quasi-Maxwellian* distribution, where a small correction to equation 2.22 is needed

$$f_s = f_s^0 + f_s^1 \tag{2.23}$$

where f_s^1 is the first order small perturbation of the Maxwellian distribution and $|f_s^1| << f_s^0$.

Because the SOL is relatively cold in comparison to the hot core plasma and has open magnetic field lines that connect to the solid wall, particle collisions between and within species are more common, enabling the achievement of local thermal equilibrium. In order to model the plasma dynamics, a fluid approach—a description that includes only a few moments of the particle distribution function for particle species—is frequently adequate. In the past Braginskii summarized a fluid description for a strongly magnetized ($\omega_{L,s}\tau_s << 1$ or $\rho_{L,s} << \lambda_{coll}$), collisional ($\lambda_{coll} << L$) for electrons and single ions species [52]. Here $\omega_{L,s}$ is the gyrofrequency for the species s, τ_s the collisional time, $\rho_{L,s}$ the Larmor radius, λ_{coll} the collisional mean free path and L is the characteristic size of the system. Some generalized models are of the Braginskii type are dealt in [53]. In order to do this, Braginskii retrieved the moments of equation 2.20 multiplying by a function $X(\mathbf{v})$ and integrating over velocity equation 2.20:

$$\frac{\partial}{\partial t}\left(\int X f_s\, d^3v\right) + \nabla\cdot\left(\int X f_s \mathbf{v}\, d^3v\right) = \frac{Z_s e}{m_s}\int (\mathbf{E} + \mathbf{v}\times\mathbf{B})\cdot\nabla_v X f_s\, d^3v + \sum_{s'}\int X C_{ss'}[f_s, f_{s'}]\, d^3v. \tag{2.24}$$

The lowest three moments relate to well known macroscopic quantities in fluid dynamics:

$$n_s(\mathbf{r},t) = \int f_s(\mathbf{r},\mathbf{v},t)\, d^3v. \tag{2.25}$$

$$\mathbf{u}_s(\mathbf{r},t) = \frac{1}{n_s}\int \mathbf{v} f_s(\mathbf{r},\mathbf{v},t)\, d^3v. \tag{2.26}$$

$$\frac{3}{2}T_s(\mathbf{r},t) = \frac{1}{n_s}\int \frac{m_s}{2} w^2 f_s(\mathbf{r},\mathbf{v},t)\, d^3v. \tag{2.27}$$

where $\mathbf{w}$ is the relative velocity $\mathbf{w} = \mathbf{v} - \mathbf{u_s}$. These are, respectively, the particle density n_s, the fluid velocity u_s and the temperature T_s.

Continuity equation

Setting X = 1 and integrating, the result will be the conservation of number of particles:

$$\frac{\partial n_s}{\partial t} + \nabla\cdot(n_s\mathbf{u_s}) = S_n \tag{2.28}$$

where S_n is the particle source.

Momentum conservation equation

Integrating with X $= m_s\mathbf{v}$ the conservation of momentum comes out:

$$\frac{\partial(n_s m_s \mathbf{u_s})}{\partial t} + \nabla\cdot(nm\mathbf{u_s}\mathbf{u_s}) + \nabla p_s + \nabla\cdot\underline{\underline{\Pi_s}} = Z_s n_s e(\mathbf{E}+\mathbf{u_s}\times\mathbf{B}) + \sum_{s'\neq s}\mathbf{R}_{ss'} \tag{2.29}$$

where $p_s = n_s T_s$ is the pressure, $\underline{\underline{\Pi_s}}$ is the viscosity tensor and $\mathbf{R}_{ss'}$ is the transfer of momentum between the species due to collisions. Considering electrons and ions as species

$$\mathbf{R}_{ei} = -\mathbf{R}_{ie} \tag{2.30}$$

which is made up of two parts: the force of friction $\mathbf{R}_u$ due to the existence of relative velocity and the thermal force $\mathbf{R}_T$ that arises for the gradient of the electron temperature T_e

$$\mathbf{R}_u = -\frac{m_e n_e}{\tau_e}(0.51\mathbf{u}_\parallel + \mathbf{u}_\perp) = en\left(\frac{\mathbf{j}_\parallel}{\sigma_\parallel} + \frac{\mathbf{j}_\perp}{\sigma_\perp}\right) \tag{2.31}$$

where $\mathbf{j} \equiv -en_e\mathbf{u}$ is the current density and σ is the electrical conductivity

$$\sigma_\perp = \frac{e^3 n_e \tau_e}{m_e} \propto T_e^{3/2} \tag{2.32}$$

$$\sigma_\parallel = 1.96\sigma_\perp \tag{2.33}$$

and

$$\mathbf{R}_T = 0.71 n_e(\mathbf{b}\cdot\nabla T_e) - \frac{3}{2}\frac{n_e}{\omega_e\tau_e}(\mathbf{b}\times\nabla T_e) \tag{2.34}$$

The viscous stress tensor in absence of a magnetic field is

$$\Pi_{ab} = -\eta_0 W_{ab} \tag{2.35}$$

where the rate of strain tensor

$$\underline{\underline{\mathbf{W}}} = \left(\nabla\mathbf{u}_i + \nabla\mathbf{u}_i^T\right) - \frac{2}{3}(\nabla\cdot\mathbf{u}_i)\underline{\underline{\mathbf{I}}} \tag{2.36}$$

where $\underline{\underline{\mathbf{I}}}$ is the unit matrix. In a strong magnetic field ($\omega_L\tau << 1$) the components of the viscous stress tensor have the following form in the coordinate system withthe z-axis parallel to the magnetic field:

$$\begin{aligned}
\Pi_{zz} &= -\eta_0 W_{zz} \\
\Pi_{xx} &= -\frac{\eta_0}{2}(W_{xx}+W_{yy}) - \frac{\eta_1}{2}(W_{xx}-W_{yy}) - \eta_3 W_{xy} \\
\Pi_{yy} &= -\frac{\eta_0}{2}(W_{xx}+W_{yy}) - \frac{\eta_1}{2}(W_{xx}-W_{yy}) + \eta_3 W_{xy} \\
\Pi_{xy} &= \Pi_{yx} = -\eta_1 W_{xy} + \frac{\eta_3}{2}(W_{xx}-W_{yy}) \\
\Pi_{xz} &= \Pi_{zx} = -\eta_2 W_{xz} - \eta_4 W_{yz} \\
\Pi_{yz} &= \Pi_{zy} = -\eta_2 W_{yz} + \eta_4 W_{xz}
\end{aligned} \tag{2.37}$$

where the plasma viscosity coefficients are:

$$
\begin{aligned}
\eta_{e,0} &= 0.73 n_e T_e \tau_e & \eta_{i,0} &= 0.96 n_i T_i \tau_i \\
\eta_{e,1} &= 0.51 \frac{n_e T_e}{\tau_e \omega_e^2} = \frac{1}{4}\eta_{e,2} & \eta_{i,1} &= \frac{3}{10}\frac{n_i T_i}{\tau_i \omega_i^2} = \frac{1}{4}\eta_{i,2} \\
\eta_{e,3} &= -\frac{1}{2}\frac{n_e T_e}{\omega_e} = \frac{1}{2}\eta_{e,4} & \eta_{i,3} &= \frac{1}{2}\frac{n_i T_i}{\omega_i} = \frac{1}{2}\eta_{i,4}
\end{aligned}
\tag{2.38}
$$

Energy conservation equation

Taking $X = \frac{1}{2} m_s v^2$ the conservation of energy will be found as:

$$
\frac{\partial}{\partial t}\left(\frac{3}{2} n_s T_s + \frac{1}{2} n_s m_s u_s^2\right) + \nabla \cdot \left[\mathbf{q}_s + \left(\frac{5}{2} n_s T_s + \frac{1}{2} n_s m_s u_s^2\right)\mathbf{u_s} + \underline{\underline{\Pi}}_s \cdot \mathbf{u_s}\right] = Z_s n_s e \mathbf{E} \cdot \mathbf{u_s} + \sum_{s' \neq s} Q_{ss'} + S_T
\tag{2.39}
$$

where $\mathbf{q_s}$ is the heat flux, $Q_{ss'}$ is the energy gained by species s due to collisions with species s' and S_T is the power source. For electrons the heat flux is given by $\mathbf{q}_e = \mathbf{q}_{e,u} + \mathbf{q}_{e,T}$

$$
\mathbf{q}_{e,u} = 0.71 n_e T_e u_{\parallel} + \frac{3}{2}\frac{n_e T_e}{\omega_e \tau_e}(\mathbf{b} \times \mathbf{u})
\tag{2.40}
$$

$$
\mathbf{q}_{e,T} = -\kappa_{e\parallel} \nabla_{\parallel} T_e - \kappa_{e\perp} \nabla_{\perp} T_e - \frac{5}{2}\frac{n_e T_e}{m_e \omega_e}(\mathbf{b} \times \nabla T_e)
\tag{2.41}
$$

where the thermal conductivities for electrons are:

$$
\kappa_{e\parallel} = \frac{3.16 n_e T_e \tau_e}{m_e} \propto T_e^{5/2}, \quad \kappa_{e\perp} = \frac{4.66 n_e T_e}{m_e \omega_e^2 \tau_e}
\tag{2.42}
$$

Similarly, the heat flux for ions:

$$
q_i = -\kappa_{i\parallel} \nabla_{\parallel} T_i - \kappa_{i\perp} \nabla_{\perp} T_i + \frac{5}{2}\frac{n_i T_i}{m_i \omega_i}(\mathbf{b} \times \nabla T_i)
\tag{2.43}
$$

with thermal conductivities:

$$
\kappa_{i\parallel} = \frac{3.9 n_i T_i \tau_i}{m_i} \propto T_i^{5/2}, \quad \kappa_{i\perp} = \frac{2 n_i T_i}{m_i \omega_i^2 \tau_i}
\tag{2.44}
$$

The expression of heat exchanged between electrons and ions through collisions is

$$
Q_{ie} = \frac{3 m_e}{m_i}\frac{n_e}{\tau_{ei}}(T_e - T_i)
\tag{2.45}
$$

while

$$
Q_{ei} = -Q_{ie} - (\mathbf{R}_u + \mathbf{R}_T)\mathbf{u}
\tag{2.46}
$$

where the term $\mathbf{R}_T \mathbf{u}$ is the Joule heat.

Finally, doing equation 2.39 - equation 2.29 $\cdot$ $\mathbf{u_s}$, the equation for *thermal energy* is found

$$\frac{\partial}{\partial t}\left(\frac{3}{2}n_sT_s\right)+\nabla\cdot\left[\mathbf{q}_s+\frac{3}{2}n_sT_s\mathbf{u_s}\right]+n_sT_s\nabla\cdot\mathbf{u_s}+\Pi:\nabla\mathbf{u_s}=\sum_{s'\neq s}\left(Q_{ss'}-\mathbf{R}_{ss'}\cdot\mathbf{u_s}\right)+S_T+\frac{1}{2}m_su_s^2S_n \tag{2.47}$$

2.2.3 Plasma sheath

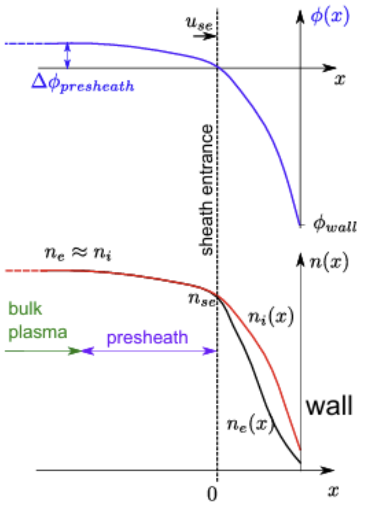

Figure 2.2: Debye shielding 1-D, taken from [5]

Due to their small mass and high mobility ($m_e << m_i$, given the thermal velocity as $v_{th} = \sqrt{T/m}$), the electrons rush ahead of the ions and strike the solid surfaces, charging them negatively. Since then, there has been an electron-repelling potential difference between the plasma and the surface, which slows the rate of electron loss while simultaneously speeding up the rate of ion loss. *Ambipolar plasma transport*, or the formation of an ambipolar electric field in the plasma, is the process by which the potential spontaneously adjusts on a surface until the loss rates of the two charge species equalize. The solid surface will spontaneously charge up to a potential of ϕ_{wall} in relation to the plasma potential. The plasma can be at nearly constant potential along any given magnetic field line and is a very good conductor in the direction along **B**. Regardless of whether the potential develops spontaneously or is applied as an external voltage, electrostatic potentials on surfaces that come into contact with plasmas are nearly completely shielded out within a short distance of the order of few *Debye lengths*

$$\lambda_D = \sqrt{\frac{\varepsilon_0 T_e}{n_e e^2}} \tag{2.48}$$

and this phenomenon is known as *Debye shielding*. This thin region is called the *Debye sheath* which is an area of net positive space charge that is in a state of dynamic equilibrium, meaning that the ions are still traveling fast through the sheath. The positive charge density almost equals the negative charge density existing on the solid surface. As a result, the space charge density in the sheath virtually shields the plasma from the electric field. However, the shielding is not perfect and a small electric field penetrates the plasma. This region is called the *pre-sheath*. Since the sheath's extent is significantly less than the mean-free path of inter-particle collisions, the plasma is essentially collisionless, necessitating a kinetic treatment of the sheath. Finding the pertinent characteristics of the particle distribution function in phase space is the objective of a kinetic treatment. Thus, electrons are assumed to satisfy, almost perfectly, a Boltzmann relation

$$n_e(x) = n_{se}exp\left(\frac{e\phi(x)}{T_e}\right) \tag{2.49}$$

in a simple treatment of the 1-D plasma sheath in absence of a magnetic field and where *se* stands for sheath entrance.

The Bohm criterion

While in plasma *quasi-neutrality* holds ($n_e \approx \sum_i n_i Z_i$), the sheath is a thin region of net charge ($n_e < n_i$). Considering the simple assumption of an isothermal fluid model with a particle source proportional to n, the plasma fluid velocity could not exceed the isothermal sound speed $c_s = [(T_e + T_i)/(m_i)]^{1/2}$. Instead, analysing the sheath side of the plasma–sheath interface (plasma–sheath edge) will come out the *Bohm criterion* [54], which states:

$$u_{se} \geq c_s \tag{2.50}$$

This result in, combining the plasma and sheath conditions, that at the sheath entrance

$$u_{se} = c_s \tag{2.51}$$

Because the sheath is so thin, collisions are typically very rare. When a group of identical gas or plasma particles are allowed to interact only through collisions, without the presence of external forces, and without any particles being lost from the system or added, a steady state known as thermodynamic equilibrium (section 2.2.2) is produced after a period of time longer than the self-collisional time. The Bohm criterion can be derived simply by assuming that the Boltzmann factor relation holds for electron density, since they are repulsed by the electrostatic well. Thus, the electron velocity distribution stays approximately Maxwellian, T_e remains constant and electron density falls of as:

$$n_e(x) = n_{se} exp\left(\frac{e(\phi - \phi_{se})}{T_e}\right) \tag{2.52}$$

where ϕ_{se} is the potential drop which occurs upstream the sheath edge. Moreover, taking the case where $T_i = 0$ (monoenergetic ions) along with the assumption that every ion come from a single point upstream of the sheath edge, this results in:

$$\frac{1}{2} m_i u_{se}^2 = -e\Delta\phi_{pre-sheath} = -e\phi_{se} \tag{2.53}$$

Now, considering the ions, from energy conservation

$$\frac{1}{2} m_i u^2 = -e\phi \tag{2.54}$$

Since the only source of ions is at the upstream source point, particle conservation gives $n_i v = const.$ so that, combining particle and energy conservation:

$$n_i = n_{se}(\phi_{se}/\phi)^{1/2} \tag{2.55}$$

Taking the *Gauss' law* for electricity:

$$\nabla \cdot \mathbf{E} = \frac{\rho}{\varepsilon_0} = \frac{e(n_e - n_i)}{\varepsilon_0} \tag{2.56}$$

and considering the 1-D sheath, being in steady state, the electric field can be expressed as the variation electrostatic potential over space, giving the 1-D *Poisson's equation*:

$$\frac{d^2\phi}{dx^2} = -\frac{e}{\varepsilon_0}(n_i - n_e) \tag{2.57}$$

Under the assumption of non-oscillatory sheath potential $\phi(x)$, the *Bohm criterion* relation 2.50 for the plasma exit velocity comes out.

In case of $T_i \neq 0$, though it makes the analysis more difficult, it is still done in the same way. The result will be:

$$u_{se} \geq c_s = [(T_e + T_i)/m_i]^{1/2} \tag{2.58}$$

rather than $c_s = [(T_e)/m_i]^{1/2}$

Furthermore, in [55] is discussed about a generalization of the $T_i \neq 0$ Bohm criterion, which can be named the *kinetic form of the Bohm criterion*:

$$u_{se} \geq c_s = [(T_e + \gamma T_i)/m_i]^{1/2} \tag{2.59}$$

where γ is the adiabatic coefficient.

Particle flux density

Consequently from previous analysis, particle outflux density can be defined as:

$$\Gamma_{se} = n_{se}u_{se} = n_{se}c_s = \Gamma_w \tag{2.60}$$

which has no dependence on how large a a potential drop exists in the sheath. The particle flux of ions and electrons towards the wall is taken into account. Only ions with an energy greater than $\frac{1}{2}m_i u_i^2 = e(\phi_{se} - \phi_w)$ can avoid the electric field's drag as they are accelerated towards the wall by the sheath potential drop. Since very few ions can accomplish this at normal ion temperatures, we can presume that every ion reaches the wall. The particle flux at the sheath entrance (se) and the particle flux at the wall are equal because of the conservation of particle flux. And for electrons, only the ones with kinetic energy greater than $\frac{1}{2}mu_e^2 = e(\phi_{se} - \phi_w)$, or those that can overcome the electric field, can make it to the solid surface. Additionally, the electron flux towards the wall must be equal at the solid surface and the sheath entrance due to the conservation of particle flux and electric charge.

Heat transmission

The sheath isn't just a particle sink, but works also as an energy sink in the SOL plasma. Considering the electrons to be Maxwellian upstream of the sheath, the heat flux can be defined as:

$$q = 2T\Gamma \tag{2.61}$$

strictly related to the particle flux density Γ.

Even if at the solid surface (ss) the electrons haven't a perfect Maxwellian distribution, the foreword going electrons to the solid surface will still correspond to a perfect Maxwellian of constant T_e since the electrostatic force is conservative. So, the net electron heat flux density at the solid surface can be represented as:

$$q^e_{ss} = 2T_e\Gamma_{ss} = 2T_e\Gamma_{se} \tag{2.62}$$

thanks to equation 2.60, given that the sheath is so thin that any particle source there is negligible. While, the net electron power flow at the sheath edge:

$$q^e_{se} = (2T_e + |e\phi_{sf}|)\Gamma_{se} \tag{2.63}$$

where ϕ_{sf} is the *sheath floating* potential drop that spontaneously arises between a plasma and a solid surface which is electrically isolated ($\Gamma^e_{se} = \Gamma^i_{se}$). Equation (2.63) is due to the fact that the majority of the electrons are reflected back within the sheath. Essentially, the sheath acts as an electron 'high energy filter', permitting only the more energetic electrons to escape. The sheath thus provides a powerful cooling effect on the electrons. Unlike with ions, it doesn't simply remove power; it specifically reduces the temperature, acting as a targeted cooling mechanism for the electrons. However, there is no drop in electron temperature T_e across the sheath. Instead, the temperature of the entire "reservoir" of plasma electrons in the SOL is reduced.

It is important to highlight that $q_{ss}^e \neq q_{se}^e$ and where this power goes. This energy is transferred to the ions, which are accelerated through the sheath. As ions move into the sheath, they tend to disrupt the sheath's electrostatic field, created by the net negative charge on the solid surface. Electrons must continually supply energy to maintain this electrostatic field, which is then transferred to the ions, increasing their kinetic energy by an amount equal to $|e\phi_{sf}|$ as they pass through the sheath. Thus, the sheath also serves as a mechanism for electron-ion energy transfer, channeling energy $|e\phi_{sf}|$ from electrons to ions for each charged pair lost to the solid surface.

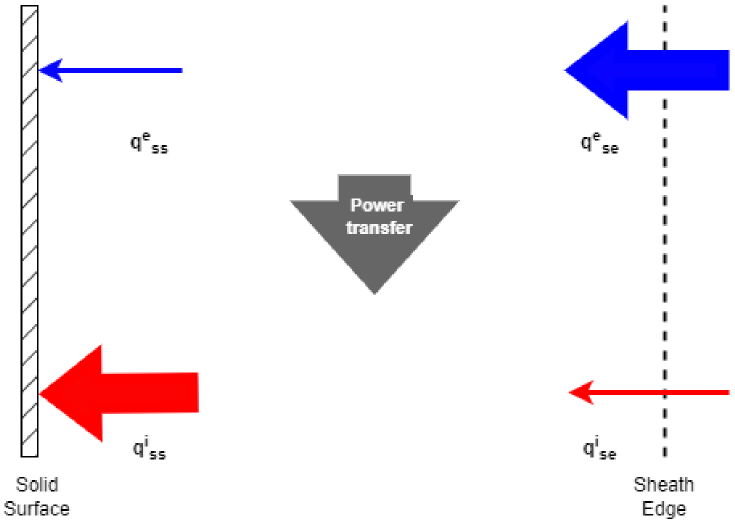

Figure 2.3: Electron–Ion energy transfer mechanism, transferring energy $|e\phi_{sf}|$ from electron to ion. Inspired by [6]

The sheath edge electron heat flux can be rewritten as:

$$q_{se}^e \equiv \gamma_e T_e \Gamma_{se} \tag{2.64}$$

where γ_e is the *electron sheath heat transmission coefficient* which can be defined by:

$$\gamma_e = 2 + |e\phi_{sf}|/T_e + |e\phi_{pre-sheath}|/T_e \approx 2 + 3 + 0.5 = 5.5 \tag{2.65}$$

Let us now consider the ions, which pose a more complex problem than the electrons. This is because ions are accelerated by the pre-sheath electric field, so even if their distribution far upstream from the sheath edge is Maxwellian, by the time they reach the sheath edge, their distribution is significantly distorted from a Maxwellian profile, as they no longer experience a net-zero force. At the sheath edge, there are no ions moving backward. If, hypothetically, the ion distribution at the sheath edge were a drifting Maxwellian with drift velocity c_s, we would then have:

$$q_{se}^i = \left(\frac{5}{2}T_i + \frac{1}{2}m_i c_s^2\right)\Gamma_{se} \tag{2.66}$$

and if $T_e = T_i$

$$q_{se}^i = \gamma_i T \Gamma_{se} \tag{2.67}$$

The ion power flux actually impacting the solid surface is, correspondingly:

$$q^{i}_{ss} \approx (\gamma_i T_i + |e\phi_{sf}|)\Gamma_{se} \tag{2.68}$$

neglecting the pre-sheath effect.

It is useful to define the *total sheath heat transmission coefficient* γ by:

$$q_{se} \equiv q^{i}_{se} + q^{e}_{se} = \gamma T_e \Gamma_{se} \tag{2.69}$$

with $\gamma \simeq 7 \div 8$ for $T_e = T_i$. Finally, note that $q_{ss} = q_{se}$ which means that, in other words, the power removed from the plasma as a whole is equal to the power received by the solid surface.

The sheath cools electrons more effectively than ions, leading to a tendency for $T_i > T_e$ in the SOL. Thus, we may distinguish two separate power channels from the main plasma into the SOL: the electron and ion channels. Moreover, the impurity radiation in the SOL tend to strengthen that $T_i > T_e$ even more.

The Chodura sheath

Until now, it has been assumed that the the magnetic field **B** was perpendicular to the solid surface. In real magnetic devices this is not true and an angle Ψ between **B** and the normal to the surface is present. This effect is desirable because the heat flux deposited on the target wall is just a fraction of the total parallel one, depending on the incidence angle

$$q_{dep} = q_{\|} cos\Psi \tag{2.70}$$

A simplified sketch of what happens in the sheath in presence of an oblique magnetic field is displayed in figure 2.4. In addition to the ordinary pre-sheath and Debye-sheath seen previously, there is the *magnetic pre-sheath*, known also as the *Chodura sheath* [56]. It is quasi-neutral and has the width of few ion Larmor radii $\rho_i = m_i v_\perp / eB \simeq m_i c_s / eB$ [57].

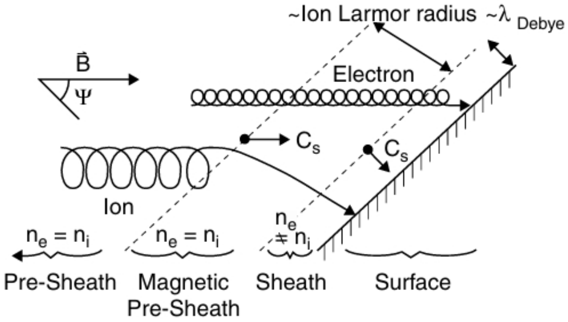

Figure 2.4: Plasma wall interaction when the angle between **B** and the solid surface is oblique. Taken by [6]

In the pre-sheath, far from the surface, electric forces remain weak due to the shielding effect of the sheath. When a strong magnetic field is present, magnetic forces dominate, causing the plasma to flow nearly parallel to **B**, even when the field is oblique to the surface. As the plasma approaches the wall, electric forces become increasingly significant, gradually redirecting the plasma flow from the magnetic field direction toward the normal of the surface. However, the electron and ion trajectories in the magnetic pre-sheath and sheath regions differ. Ions begin to deviate when their distance from the wall is approximately their gyroradius, while electrons, due to their lower mass, remain more tightly bound to magnetic field lines. They continue to flow along **B** until they reach the sheath entrance, where their path is finally deflected. Chodura demonstrated [56] that the Bohm criterion, given by equation (2.50), remains valid at the entrance of the magnetic pre-sheath

$$v_{\parallel \mathbf{B}}^{Ch-se} \geq c_s \tag{2.71}$$

known as the *Chodura criterion.* This implies that the upstream plasma does not "sense" whether the plasma flow tube terminates in a normal or an oblique sheath. Consequently, while the choice of angle Ψ significantly impacts heat dissipation, as described by equation (2.70), it has minimal influence on other plasma properties.

3. Scrape-Off-Layer modeling

Modeling refers to the process of constructing a mathematical, computational or conceptual representation of a complex phenomenon present in reality. Its aim is to simulate, predict, and understand real-world behaviors by capturing essential characteristics. Nevertheless, a model by definition cannot be a perfect replica of what reality is and some approximations and/or simplifying assumptions are necessary. The more the approximations the less the reliability of the model will be. Consequently, a model requires a *validation*, i.e. a comparison with experimental or observational data to ensure that the model results are reliable and meaningful for the study performed. Anyway, modeling remains a really strong feature to try to understand and predict very complex physical phenomena as nuclear fusion is. For instance, it could support in the understanding of some physical behaviors or to predict the evolution of a system in certain conditions to figure out what to focus on and avoid wasting money [58].

In the following, different level of modeling sophistication are presented, starting from a "simple" analytical model, section 3.1, to a more complex computational/mathematical model, section 3.2.

3.1 Analytic 2 Point Modeling

As already anticipated in section 1.3, in a tokamak the divertor targets will be damaged if the power flux density deposited on them exceeds thermo-mechanical engineering limits. Additionally, a slower erosion process may occur, but it will remain intolerable unless the net erosion rate is extremely low. So, it's important to define a *target parameter operating window.* To do so, the heat load on the wall has to be analysed.

The parallel power flux density can be divided into:

- Thermal energy - T
- Kinetic energy - mnv^2
- Potential energy - ε_H^{pot}

The target sheath causes plasma cooling by removing the plasma's thermal and kinetic energy:

$$q_{||t}^{plasma-cooling} = \gamma_{sheath}^{plasma-cooling} n_t T_{et} c_{st} \tag{3.1}$$

where $c_{st} = \sqrt{2T_{et}/m_i}$ is the isothermal plasma sound speed at the target. The power flux density deposited on the target by the plasma can be defined as:

$$q_{dep,t}^{plasma} = q_{||t}^{target-heating} sin\theta_{\perp} = \gamma_{sheath}^{target-heating} n_t T_{et} c_{st} sin\theta_{\perp} \tag{3.2}$$

where $\theta_\perp$ is the incidence angle between $\mathbf{B}$ and the target surface and

$$\gamma_{sheath}^{target-heating} = \gamma_{sheath}^{plasma-cooling} + \frac{\varepsilon_H^{pot}}{T_{et}} \tag{3.3}$$

where the potential energy is given by ionization and molecular dissociation.

Furthermore, it's fundamental to understand the level of volumetric power loss required in the tokamak edge, i.e. in the SOL and divertor due to radiation, etc. For each flux tube in the edge we have from power balance:

$$q_{\parallel u} A_{\parallel u} = q_{\parallel t}^{target-heating} A_{\parallel t} + \int_u^t Q_{loss-edge}(s_\parallel) A_\parallel(s_\parallel)\, ds_\parallel \tag{3.4}$$

where $A_\parallel$ is the cross-sectional area of the flux tube perpendicular to $\mathbf{B}$, $q_{\parallel u}$ $[MWm^{-2}]$ is the value of the parallel power flux density at the upstream end of the flux tube and $Q_{loss-edge}$ $[MWm^{-3}]$ is the volumetric power loss density in the flux tube. Then, it is convenient to define the *power loss fraction* of a flux tube as:

$$f_{pwr-loss}^{edge} = \frac{\int_u^t Q_{loss-edge}(s_\parallel) A_\parallel(s_\parallel)\, ds_\parallel}{q_{\parallel u} A_{\parallel u}} \tag{3.5}$$

Conservation of total magnetic flux gives $A_\parallel \propto 1/B$, and since for tokamaks $B \propto 1/R$, which comes out to good approximation:

$$(1 - f_{pwr-loss}^{edge}) q_{\parallel u} R_u = q_{\parallel t}^{target-heating} R_t \tag{3.6}$$

where R_t/R_u is the *toroidal flux expansion.*

The *2 Point Model* (2PM) is a widely used analytic model for relating *target* (t) conditions (T_t, n_t) to the *upstream* (u) conditions, in particular to the primary control quantities, i.e. the primary drivers of the SOL plasma:

- plasma pressure (or density) at the divertor entrance or outer mid-plane (OMP) - $p_u(n_u)$
- the parallel power flux density at the divertor entrance - $q_{\parallel u}$

A first, rough, model was developed (see section 5.2 of [6]), known as the basic (conductive) 2PM. This relates upstream and downstream quantities on individual flux tubes in the SOL using the conservation equations without taking into account the volumetric losses in momentum and energy equations. In particular, in the pressure balance, if no friction between the plasma flow in the thin ionization region and the target and no viscous effects is assumed, it results the conservation of total pressure along a flux tube:

$$p_{tot} = p_{static} + p_{dynamic} = nT_e + nT_i + mnv^2 = constant \tag{3.7}$$

becoming, for the Bohm criterion

$$2n_t T_t = n_u T_u \tag{3.8}$$

And, with the assumption that parallel heat convection is absent and the all parallel power flux density is carried by conduction, following the classical Spitzer-Härm parallel heat conduction definition

$$q_\parallel = -\kappa_0 T^{5/2} \frac{dT}{ds_\parallel} \tag{3.9}$$

from where upstream temperature can be evaluated as

$$T_u = \left[T_t^{7/2} + \frac{7}{2} \frac{q_{\parallel u} L}{\kappa_{0e}} \right]^{2/7} \approx \left[\frac{7}{2} \frac{q_{\parallel u} L}{\kappa_{0e}} \right]^{2/7} \tag{3.10}$$

where L is the connection length and κ_{0e} is the electron parallel conductivity coefficient, neglecting the ion one as comparatively small. With the addition of the definition of the power flux density entering the sheath

$$q_{\parallel,t} = \gamma n_t T_t c_{st} \tag{3.11}$$

where γ is the sheath heat transmission coefficient. Then, putting together equations (3.8), (3.10), (3.11) we have the conductive 2PM.

Anyway, the 2PM has been extended to include volumetric losses in a simple form and including both conductive and convective to $q_{\parallel u}$ in [59] and differently from section 5.4 in [6]. The most complete 2PM formulation is given in [60]. Thus, from the volumetric loss (transfer) terms for power and momentum, $(1 - f_{pwr})$ and $(1 - f_{mom})$ respectively, are defined by the relations:

$$(1 - f_{pwr}) q_{\parallel u} R_u = q_{\parallel t}^{plasma-cooling} R_t \tag{3.12}$$

$$(1 - f_{mom}) p_{tot,u} = p_{tot,t} \tag{3.13}$$

The resulting 2PM equations for target temperature, target density and target particle flux retrieved from equations (18)-(23) in [59] will be:

$$T_{et}^{2PM} = \left(\frac{8m_i}{e\gamma^2}\right)\left(\frac{q_{\parallel u}^2}{p_{tot,u}^2}\right)\left(\frac{(1-f_{pwr})^2}{(1-f_{mom})^2}\right)\left(\frac{R_u}{R_t}\right)^2\left(\frac{(1+M_t^2)^2}{4M_t^2}\right)\left(\frac{(1+\tau_t/z_t)}{2}\right) \tag{3.14}$$

$$n_{et}^{2PM} = \left(\frac{\gamma^2}{32m_i}\right)^{1/3}\left(\frac{p_{tot,u}^3}{q_{\parallel u}^2}\right)\left(\frac{(1-f_{mom})^3}{(1-f_{pwr})^2}\right)\left(\frac{R_t}{R_u}\right)^2\left(\frac{8M_t^2}{(1+M_t^2)^3}\right)\left(\frac{4}{(1+\tau_t/z_t)^2}\right) \tag{3.15}$$

$$\Gamma_{e\parallel t}^{2PM} = \left(\frac{\gamma}{8m_i}\right)\left(\frac{p_{tot,u}^2}{q_{\parallel u}}\right)\left(\frac{(1-f_{mom})^2}{(1-f_{pwr})}\right)\left(\frac{R_t}{R_u}\right)\left(\frac{4M_t^2}{(1+M_t^2)^2}\right)\left(\frac{2}{(1+\tau_t/z_t)}\right) \tag{3.16}$$

where M is the plasma flow Mach number based on sound speed $M = v/c_{st}$, $\tau \equiv T_i/T_e$ and $z \equiv n_e/\sum_a n_a$.

The strength of the 2PM stands in the fact that with these simple analytical relations we are able to describe the most important target variables. These are strictly related to the upstream control quantities (independent variables), which are classically those variables that can be controlled in the functioning of a tokamak device, such as the input power and the density inside the reactor. The ultimate goal is to reach the *detachment* regime (section 1.3.1) to mitigate the power exhaust problem. From equations (3.14), (3.15) and (3.16) it is possible to understand how to change the upstream control quantities to achieve the target survival values (check figure 1 of [59] to see the target parameter operating window) of T_t and n_t. The goal is to achieve simultaneously low T_t and high n_t and can be done

- reducing $q_{\parallel,u}$, so diminishing, for instance, the power crossing the separatrix $P_{SOL} = P_{core} - P_{core}^{rad}$ increasing the rate od radiation in the core
- raising $p_{u,tot}$, i.e. increasing plasma density
- increasing the fraction of volumetric power losses f_{pwr}
- decreasing the momentum losses f_{mom}, i.e. f_{pwr} and f_{mom} are in competition
- increasing the *flux expansion* R_t/R_u

Furthermore, a model where the contrary happens, i.e. finding the upstream primary drivers best values based on the target values imposed was analyzed on [61]. While a model, always realized by

Stangeby, including the commonly excluded recycle power losses can be found in [62]. Then, many other analytical models based on the 2PM were studied, as the

- *Modified 2PM* which takes into account the variation of R with the poloidal position $s_\parallel$ [63]
- *2 fluid 2PM* [64], where thermal decoupling in the SOL is assumed due to the fact that $T_i^u > T_e^u$ [39], thus allowing the separation of the equations for electron and ions for heat conduction and conservation along field line
- *Box model* [65] which is similar to the previous two

Lastly, for post-processing purposes the two-point model can also be utilized to interpret the output of transport code simulations, a process referred to as *two-point model formatting* [59]. In the simplest one, the 2PMF *wovi*-without volume integration- the loss terms are calculated for each flux tube based on the code output (equations (3.12) and (3.13)), requiring information at only two specific locations, upstream and at target. Instead, the 2PMF *wivi*-with volume integration- where code output is utilized at all intermediate locations between upstream and target, providing significantly more information than the 2PMF *wovi*. For maximum information, along-flux-tube integrals are calculated for each individual source/sink term in each of the conservation equations, resulting in

$$f_{pwr} \equiv \frac{\int_t^u R(s_\parallel) S_{pwr}(s_\parallel) ds_\parallel}{q_{\parallel,u} R_u} \tag{3.17}$$

$$f_{mom} \equiv \frac{\int_t^u S_{mom}(s_\parallel) ds_\parallel}{p_{tot,u}} \tag{3.18}$$

where $S_{pwr}(s_\parallel)$ and $S_{mom}(s_\parallel)$ are the volumetric loss density terms.

3.2 The SOLPS-ITER code

The SOLPS-ITER code ([66], [7]) is the latest development of the code package SOLPS (*Scrape Off Layer Plasma Simulator*) which was fundamental in the ITER design study. It consists in a coupling of two distinct physical modules, namely *B2.5*, a 2D multi-fluid plasma transport code and the most recent version of *EIRENE*, a 3D kinetic Monte Carlo neutral transport code. The very first version of the code was developed by B. Braams during his Ph.D. [67] and then improved and firstly coupled with the EIRENE Monte Carlo code by M. Baelmans during her PhD [68].

SOLPS-ITER can operate in two different modes: standalone (where only B2.5 runs) or fully coupled (where both B2.5 and EIRENE run together, [7]). In standalone mode, only the fluid module is used, meaning that fluid equations govern both charged plasma particles and neutral particles. Conversely, in the fully coupled mode, plasma particles are still described using the fluid module, while the transport of neutral species, along with their interactions with plasma and material surfaces, is handled by the Monte Carlo module. Specifically, in this case, the coupling occurs through surface and volumetric sources/sinks for the plasma in B2.5, which are determined based on neutral interactions computed by EIRENE [69]. The key advantage of the standalone mode is its significantly faster computation time and the absence of Monte Carlo noise in the results. However, simulations in coupled mode offer higher accuracy, particularly in scenarios where the neutral density is relatively high. In addition, the package also contains other tools, namely *DivGeo* and *Carre*, which are used to generate the computational grid for B2.5.

The code solves the equations governing the behavior of a fluid plasma (see section 2.2.2) in the edge region, considering a 2D poloidal section in toroidal simmetry, which consists on the outer core plasma and the entire scrape-off layer (section 3), down to the divertor region. The primary objective of SOLPS-ITER is to accurately capture a steady-state condition, achieved through a time-dependent convergence process in which plasma evolution is tracked by solving the included equations, in accordance with the described inputs and boundary conditions. Once this steady state is reached, all relevant information for the modeled scenario can be extracted.

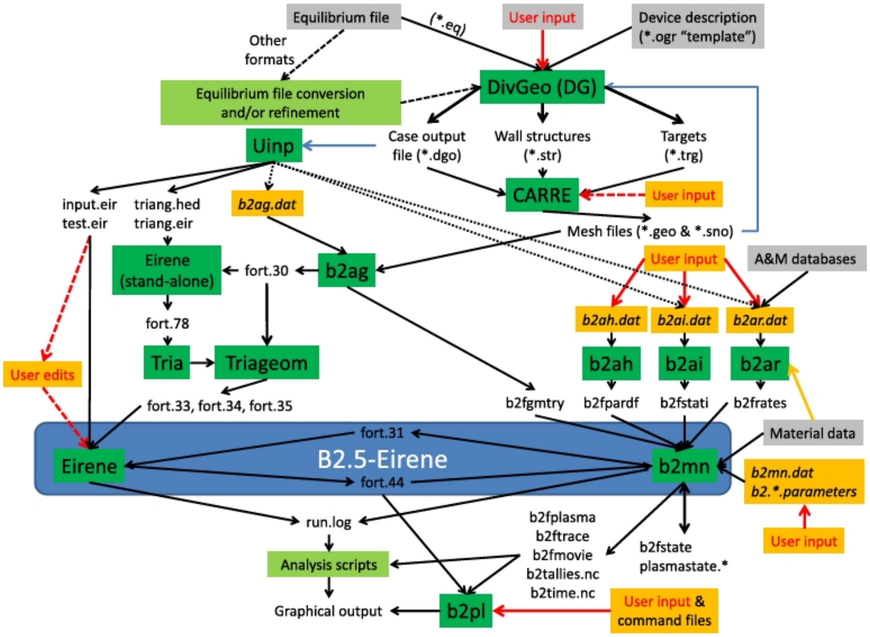
Equilibrium file
(*.eq)
User input
Device description
(*.ogr "template")
Other
formats
Equilibrium file conversion
and/or refinement
DivGeo (DG)
Uinp
Case output
file (*.dgo)
Wall structures
(*.str)
Targets
(*.trg)
CARRE
User input
input.eir
test.eir
triang.hed
triang.eir
b2ag.dat
Mesh files (*.geo & *.sno)
User input
A&M databases
Eirene
(stand-alone)
fort.30
b2ag
fort.78
b2ah.dat
b2ai.dat
b2ar.dat
Tria
Triageom
b2ah
b2ai
b2ar
User edits
fort.33, fort.34, fort.35
b2fgmtry
b2fpardf
b2fstati
b2frates
Material data
fort.31
Eirene
B2.5-Eirene
b2mn
fort.44
b2mn.dat
b2.*.parameters
run.log
b2fplasma
b2ftrace
b2fmovie
b2tallies.nc
b2time.nc
b2fstate
plasmastate.*
User input
Analysis scripts
Graphical output
b2pl
User input &
command files

Figure 3.1: SOLPS-ITER workflow, taken by [7]

3.2.1 B2.5 multi-fluid code

B2.5 is the fluid module of SOLPS-ITER, entirely written in FORTRAN 90, and is responsible for computing the evolution of charged plasma particles. Specifically, it solves the fluid transport equations—namely, a modified version of the Braginskii equations seen in section 2.2.2—for electrons and an arbitrary number of ion species, all of which share the same temperature. These equations are solved using a finite volume discretization method.

At each numerical iteration, corresponding to a single time step, volumetric and surface source terms are computed, and the conservation equations (for particles, momentum, and energy, as well as potential if currents are considered) are solved. The process continues for the required number of time steps until convergence is achieved, which is monitored by evaluating the norm of the residuals for each conservation equation. A steady-state condition is considered reached when no significant variations in the main plasma parameters are observed, regardless of the chosen time step.

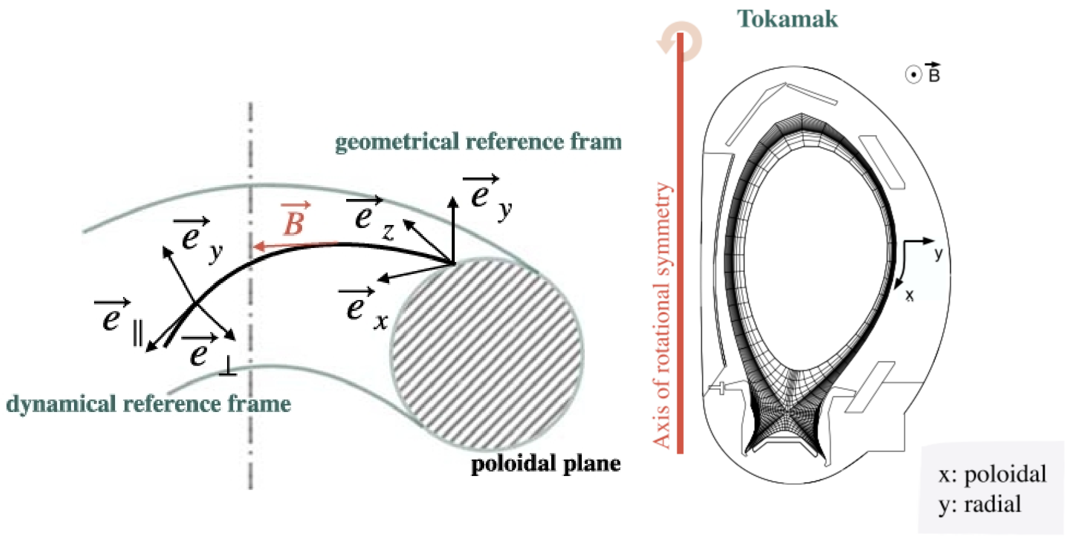
geometrical reference fram
$\vec{e}_y$
$\vec{B}$
$\vec{e}_z$
$\vec{e}_y$
$\vec{e}_\parallel$
$\vec{e}_\perp$
$\vec{e}_x$
dynamical reference frame
poloidal plane
Tokamak
$\vec{B}$
Axis of rotational symmetry
y
x
x: poloidal
y: radial

(a) (b)

Figure 3.2: a) Curvilinear reference frame of B2.5 . b) Geometrical reference frame of a tokamak (ASDEX in figure), taken by [8]

The equations are solved on a curvilinear grid that spans the entire plasma edge region and is strictly aligned with the magnetic field lines. Consequently, this grid must be generated by importing the magnetic equilibrium configuration of the specific scenario being modeled. The numerical calculations are performed on a topologically rectangular mesh, where the transformation between the physical geometry and the computational mesh is defined in each cell through a set of metric coefficients [68]: $h_x = 1/|\nabla x|^{-1}, h_y = 1/|\nabla y|^{-1}, h_z = 1/|\nabla z|^{-1} = 2\pi R$ with the cell volume $\sqrt{g} = h_x h_y h_z$. This results in a curvilinear orthogonal coordinate system, where the x-direction represents the orthogonalized poloidal coordinate, the y-direction represents the orthogonalized radial coordinate and z is the direction of rotational symmetry, hence in tokamak case this will be the toroidal direction, as represented in figure 3.2a. The resulting rectangular grid on B2.5 for a lower single null divertor configuration is displayed in figure 3.4.

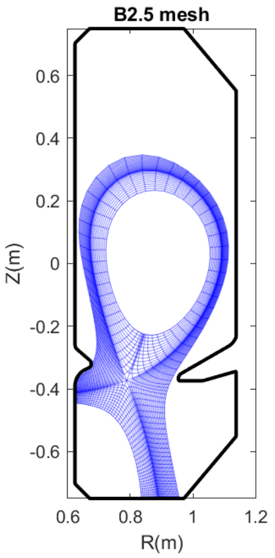

Figure 3.3: B2.5 mesh of TCV SILO

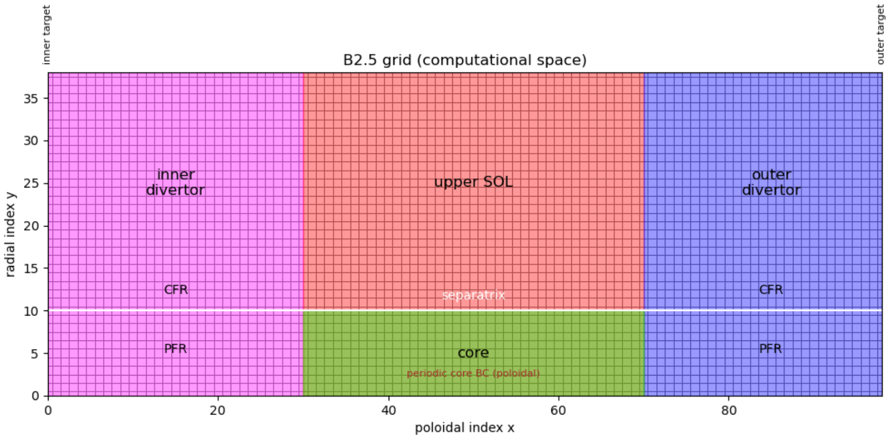
inner target
outer target
B2.5 grid (computational space)
inner
divertor
upper SOL
outer
divertor
CFR
separatrix
CFR
PFR
core
periodic core BC (poloidal)
PFR
radial index y
0
5
10
15
20
25
30
35
poloidal index x
0
20
40
60
80

Figure 3.4: B2.5 computational space in a LSN configuration, inspired by [5]

3.2.2 B2.5 model equations

The equations implemented in the B2.5 module for the physical description of the system are of the Braginskii type, section 2.2.2, adapted to the rectangular computational mesh.

Continuity equation

The ion particle continuity equation

$$\frac{\partial n_a}{\partial t} + \frac{1}{\sqrt{g}}\frac{\partial}{\partial x}\left(\frac{\sqrt{g}}{h_x}\tilde{\Gamma}_{a,x}\right) + \frac{\partial}{\partial y}\left(\frac{\sqrt{g}}{h_y}\tilde{\Gamma}_{a,y}\right) = S_n^a \tag{3.19}$$

is solved for the particle density n_a, where a represents each ion species included in the simulations. $\tilde{\Gamma}_{a,x}$ and $\tilde{\Gamma}_{a,y}$ are the effective poloidal and radial particle fluxes respectively and S_a^n is the total particle source, grouping all the sources and sinks. The effective particles fluxes are described as

$$\tilde{\Gamma}_{a,x} = (b_x v_{\parallel,a})n_a - D_{\perp,a}^{AN}\frac{1}{h_x}\frac{\partial n_a}{\partial x} \tag{3.20}$$

$$\tilde{\Gamma}_{a,y} = -D_{\perp,a}^{AN}\frac{1}{h_y}\frac{\partial n_a}{\partial y} \tag{3.21}$$

where $b_x = B_x/B$ is the poloidal projection, $D_{\perp,a}^{AN}$ is the spatially constant anomalous cross-field transport coefficient in our case equal to $0.2m^2s^{-1}$. Other terms aren't displayed because of the settings of the simulations of our interest. Instead, the source term accounts for ionisation, recombination and charge-exchange processes not involving neutrals on the B2.5 side, while additional particle sources involving atomic or molecular neutrals are provided by Eirene. The electron desnity follows from quasi-neutrality, i.e. $n_e = \sum_a Z_a n_a$.

Parallel momentum equation

The parallel ion momentum equation

$$m_a \frac{\partial}{\partial t}\left(n_a u_{\|,a}\right) + \frac{1}{h_z\sqrt{g}}\frac{\partial}{\partial x}\left(h_z\frac{\sqrt{g}}{h_x}\tilde{\Gamma}^m_{a,x}\right) + \frac{1}{h_z\sqrt{g}}\frac{\partial}{\partial y}\left(h_z\frac{\sqrt{g}}{h_y}\tilde{\Gamma}^m_{a,y}\right) = S^m_a \tag{3.22}$$

is solved for the parallel velocity $u_{\|,a}$ of ion species a. $\tilde{\Gamma}^m_{a,x}$ and $\tilde{\Gamma}^m_{a,y}$ are the poloidal and radial momentum fluxes respectively and S^m_a is the total momentum source. The momentum fluxes

$$\tilde{\Gamma}^m_{a,x} = m_a u_{\|,a}\Gamma_{a,x} - \eta_{a,x}\frac{\partial u_{\|,a}}{h_x\partial x} \tag{3.23}$$

$$\tilde{\Gamma}^m_{a,y} = m_a u_{\|,a}\Gamma_{a,y} - \eta_{a,y}\frac{\partial u_{\|,a}}{h_y\partial y} \tag{3.24}$$

where the first term in the RHS denote the convection and the second is the viscous contribution, with η_a the viscosity coefficient. The source term includes the centrifugal forces, friction forces, thermal forces and momentum sources due to plasma-neutral interactions from Eirene. The electron velocity follows from the parallel electric current $u_{\|,e} = (\sum_a e n_a u_{\|,a} - j_\|)/(e n_e)$.

Electron energy equation

The electron energy equation

$$\frac{3}{2}\frac{\partial}{\partial t}(n_e T_e) + \frac{1}{\sqrt{g}}\frac{\partial}{\partial x}\left(\frac{\sqrt{g}}{h_x}\tilde{q}_{e,x}\right) + \frac{1}{\sqrt{g}}\frac{\partial}{\partial y}\left(\frac{\sqrt{g}}{h_y}\tilde{q}_{e,y}\right) = S^h_e \tag{3.25}$$

is solved for the electron temperature T_e. $\tilde{q}_{e,x}$ and $\tilde{q}_{e,y}$ are the poloidal and radial effective heat fluxes respectively and S^h_e is the total electron energy source. The heat fluxes

$$\tilde{q}_{e,x} = \frac{3}{2}\Gamma_{e,x}T_e - \left(\kappa^{AN}_e + \kappa^{CL}_{e,x}\right)\frac{1}{h_x}\frac{\partial T_e}{\partial x} - 0.71 T_e\frac{j_{\|,x}}{e} \tag{3.26}$$

$$\tilde{q}_{e,y} = \frac{3}{2}\Gamma_{e,y}T_e - \left(\kappa^{AN}_e + \kappa^{CL}_{e,y}\right)\frac{1}{h_y}\frac{\partial T_e}{\partial y} \tag{3.27}$$

are the combination of the convective heat flux, the conductive one, containing both the anomalous κ^{AN} and the classical κ^{CL} contributions. In the poloidal direction, the anomalous contribution is minimal, and electron heat conduction is primarily governed by classical conductivity, i.e. the Spitzer-Härm conductivity. Instead, the anomalous cross-field conductivity is defined as $\kappa^{AN}_e = n_e\chi^{AN}_e$ with χ^{AN}_e the anomalous cross-field energy coefficient and is dominant in the radial direction. The third term in equation (3.26) is the heat flux connected with thermal forces. Moreover, the source term can include the compression term, the energy exchange through electron-ion Coulomb collisions, volumetric radiation losses due to line radiation and Bremsstrahlung, as well as the energy consumed for the ionization of non-neutral species, heat generated by friction and thermal forces and interactions with neutrals, calculated by Eirene.

Ion energy equation

The ion energy equation

$$\frac{3}{2}\frac{\partial}{\partial t}(n_i T_i) + \frac{1}{\sqrt{g}}\frac{\partial}{\partial x}\left(\frac{\sqrt{g}}{h_x}\tilde{q}_{i,x}\right) + \frac{1}{\sqrt{g}}\frac{\partial}{\partial y}\left(\frac{\sqrt{g}}{h_y}\tilde{q}_{i,y}\right) = S^h_i \tag{3.28}$$

is solved for the ion temperature T_i, assumed to be equal for all ionic species a. $\tilde{q}_{i,x}$ and $\tilde{q}_{i,y}$ are the poloidal and radial effective heat fluxes respectively and S_i^h is the total ion energy source. The heat fluxes

$$\tilde{q}_{i,x} = \frac{3}{2}\Gamma_{i,x}T_i - \left(\kappa_i^{AN} + \kappa_{i,x}^{CL}\right)\frac{1}{h_x}\frac{\partial T_i}{\partial x} \tag{3.29}$$

$$\tilde{q}_{i,y} = \frac{3}{2}\Gamma_{i,y}T_i - \left(\kappa_i^{AN} + \kappa_{i,x}^{CL}\right)\frac{1}{h_y}\frac{\partial T_i}{\partial y} \tag{3.30}$$

Such as the electrons, the total heat flux consists of convective and conductive components, with the latter incorporating contributions from both anomalous (κ^{AN}) and classical (κ^{CL}) conductivity. The ion energy source is very similar to that of electrons, apart from the viscous heating, ionization, recombination and charge exchange terms.

Current balance equation

The current continuity equation

$$\frac{1}{\sqrt{g}}\frac{\partial}{\partial x}\left(\frac{\sqrt{g}}{h_x}j_x\right) + \frac{1}{\sqrt{g}}\frac{\partial}{\partial y}\left(\frac{\sqrt{g}}{h_y}j_y\right) = 0, \tag{3.31}$$

is solved for the electric potential ϕ. j_x and j_y are the poloidal and radial currents. The parallel component of the poloidal electric currents is described as

$$j_{\parallel x} = \sigma_\parallel\left(\frac{b_x}{e}\frac{1}{h_x}\left(\frac{\partial(n_eT_e)}{n_e\partial x} + 0.71\frac{\partial T_e}{\partial x}\right) - \frac{b_x}{h_x}\frac{\partial\phi}{\partial x}\right), \tag{3.32}$$

while, the anomalous current contribution is artificially introduced mainly to ensure code stability

$$j_x^{AN} = -\sigma^{AN}\frac{\partial\phi}{h_x\partial x}, \tag{3.33}$$

$$j_y^{AN} = -\sigma^{AN}\frac{\partial\phi}{h_y\partial y}. \tag{3.34}$$

where σ^{AN} is the anomalous electrical conductivity.

3.2.3 EIRENE code

The original derivation of the EIRENE [70] Monte Carlo model was carried out in D. Reiter's PhD thesis [71]. EIRENE is the module dedicated to modeling neutral species, also written in FORTRAN 90. The latest version of EIRENE includes an expanded set of atomic and molecular processes, the ability to simulate radiation losses, neutral-neutral and photon-neutral collisions, as well as the option to run simulations in parallel mode. Specifically, EIRENE solves the linear kinetic transport equations for neutrals using a Monte Carlo method, treating them as test particles moving within a 3D volume. It computes the statistical expectation values for interactions between these test particles and the plasma by tracking the histories of a large number of them as they propagate through the plasma. The operating principle of EIRENE is as follows: a set number of test particles is introduced into a background medium from a designated source, with an initial distribution of directions and velocities. In a coupled SOLPS-ITER simulation, this background medium corresponds to the plasma state computed at each time step by B2.5 [72]. The distances traveled by these test particles are randomly determined but remain proportional to their mean free path. Each test particle is tracked along its trajectory until it either gets absorbed at a material surface or becomes ionized, joining the plasma background. The probabilities of different events occurring along the particle's trajectory are determined based on the cross sections of the relevant atomic processes. Once the simulation has run, multiple histories of test particles are recorded, from which averaged values of the relevant physical quantities are derived at each spatial location. The rate coefficients for atomic processes affecting these test particles—such as interactions with plasma particles—are sourced from external atomic physics databases like AMJUEL and HYDHEL.

EIRENE's computations take place in a fully 3D geometry using tetrahedral volumes, which reduce to a triangular grid in the poloidal plane. This grid extends beyond the entire computational domain of B2.5, reaching the material boundaries of the main chamber wall. At these boundaries, material surfaces are characterized by specific absorption and reflection probabilities to account for the interactions of neutral particles with solid surfaces.

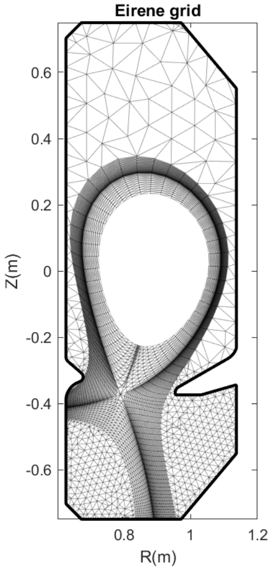

Figure 3.5: Eirene grid of TCV SILO

4. Simulation results

Energy transport in the Scrape-Off Layer (Chapter 3) is a very complex phenomenon and to model it is an extremely difficult task which requires many assumptions and adjustments.

In this chapter, we present the results of a parametric study aimed at investigating how variations of key parameters influence energy transport and the overall energy balance in the SOL of the TCV (section 1.11) tokamak, specifically in its SILO (Short Inner Long Outer) (section 1.4.1) baffled configuration with just deuterium D and carbon C impurities and with a Lower Single Null divertor.

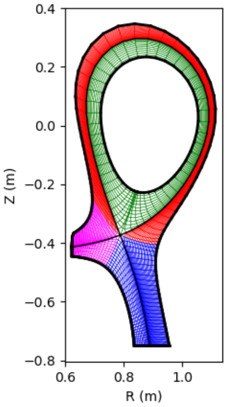

Figure 4.1: Regions division in the TCV SILO simulated: Core, SOL, Inner divertor, Outer divertor

The primary focus of this study is the transport of energy by electrons and ions in the SOL, with particular attention to the behavior of ions near the last flux surface. The last because, in experiments, was noticed a difference between electron and ion temperatures diverse than expected. The same was noticed in simulations, but with underestimated T_i values wrt experimental measurements, as said in [40]. Given the complex transport mechanisms in this region (section 2.2.3), we analyze how changes in some important parameters for energy transport affect the power balance. The results of these simulations can provide insights about the dominant transport mechanisms and help refine existing models of SOL physics in the SOLPS-ITER code package.

The scan will be performed on the following features:

1. Fraction of power into the electron and ion populations at fixed total input power. We will refer to this as *power split*.

   The reason of this scan lies in the fact that, in the past and in the present, most of the fluid simulations of the tokamak edge were using the assumption of setting as input boundary condition evenly distributed power in the core for both electrons and ions in the simulations $P^e_{core} = P^i_{core}$. This was doubted since it was thought that an offset between the two could have result in $T^u_i \approx T^u_e$. In addition, since the simulations refer to *L-mode ohmic discharges*, it is expected that electrons will be hotter than ions in the core because of their lighter mass, gaining greater acceleration and hence more energy due to the electric current passing through the plasma.

2. Ion and electron anomalous cross-field energy transport coefficients - χ_i and χ_e

   Fluid codes such as SOLPS-ITER do not directly model turbulence (section 2.1), as they rely on macroscopic equations that do not resolve the small-scale fluctuations responsible for turbulence. Instead, they use effective transport coefficients to approximate the enhanced transport caused by turbulence. These coefficients are usually empirically fitted based on experimental data [73] or prescribed using simplified theoretical models (e.g. Bohm/gyro-Bohm scaling) [49]. In particular, since the total ion and electron heat fluxes consist of a conductive component and a convective one, values for the radial thermal diffusivities can be inferred from the experimental density and temperature profile.

   Even if this approach may work reasonably well for large-scale transport studies, it lacks the self-consistent physics of turbulence seen in kinetic or gyrokinetic models [74], where small-scale fluctuations and drift-wave dynamics are resolved explicitly. An interesting study of the application of the, well known in fluid dynamics analysis, RANS (Reynolds Averaged Navier Stokes) to the Braginskii-like plasma equations implemented in SOLPS-ITER can be found in [75].

   Since theoretical predictions very often struggle to match with the experimental values [76] and also because the actual anomalous energy diffusivity can vary depending on specific plasma conditions (strong of the fact that anomalous cross-field transport is not a completely well understood phenomena yet) a scan on these parameters has been performed.

   It is of interest to understand how plasma parameters change in the SOL due to increased or decreased cross-field energy transport, with particular focus of the difference in temperature between electrons and ions.

3. Ion flux limiter on the ion parallel heat conduction - *cflmi*

   A fluid description of the plasma edge is overall good, but there may be exceptions. The necessary condition for a fluid model is that all characteristic lengths must be smaller than the parallel connection length. This condition is usually fulfilled, unless in the presence of steep temperature gradients or when collisionality drops. In this case, classical local transport theory breaks down and the thermal transport becomes ‘non-local’ [77]. To accurately capture these non-localities is a major challenge in the SOL modeling.

   To capture non-locality without resorting to full kinetic modeling in case of low collisionality [78], a first simple solution widely used was the implementation of the *flux limiters*, i.e. a parameter that limit the heat flux when the local Spitzer-Härm model ($k_{\parallel} \propto T^{5/2}$) predictions become unphysically large, thus exceeding greatly the *free streaming heat flux* $q_{fs} = nvT = \Gamma T$. So, Spitzer-Härm is limited to a specified fraction α of q_{fs} using equation

   $$\frac{1}{q_{\parallel}} = \frac{1}{q_{SH}} + \frac{1}{\alpha q_{fs}} \tag{4.1}$$

   Thus, the thermal conductivity in the heat flux calculation is adjusted to an "effective" thermal conductivity

   $$k_{eff} = k_{SH} \frac{1}{1 + \frac{q_{SH}}{\alpha q_{fs}}} \tag{4.2}$$

   While there is greater comprehension of the electron flux limiter (cflme = 0.2) [79] from comparison with kinetic calculations [80] for electrons, the situation for ions is less clear and has to be studied further. Then, a parametric scan analysis on the values of the ion flux limiter *cflmi* has been performed to understand deeper what is its effect on the energy transport in the scrape-off layer.

> In past simulations performed at the Swiss Plasma Center, it was noticed that the change of the ion flux limiter was affecting greatly the outer target plasma parameters. Further study about this parameter is done with the aim of understand more in depth its impact on energy balance in the TCV.

The simulations will be run without drifts, for computational cost reasons, and in *feedback* mode, meaning that we fix a value of electron upstream density at separatrix $n_{e,sep}$ where the gas puff (entering from the gas valve, placed close to the Outer Strike Point OSP in the outer leg) of molecular deuterium D_2 is varied iteratively until convergence of the target density value. More details and motivation of the study done will be given later on in the following sections.

To do so, some fundamental plasma variables and fluxes from code output are analysed, juxtaposed by an internal energy balance of electrons and ions (equations (3.25) and (3.28)) from the *balance.nc* file generated in the code.

4.1 Input power on electrons and ions

The focus of this section will be on cases with larger electron input power at the core boundary with consequently decreased ion input power.

The total input power in the core is fixed at 330 kW and the **reference** simulation has the even power split between electrons and ions of $P^e_{core} = P^i_{core} = 165kW$. The scan will be performed by progressively increasing the input power for electrons while decreasing of the same amount the one for ions. The different cases will be differentiated in the figures by the percentage of input power for electrons or ions with respect to the total fixed input one, i.e. $P^e_{core}/P^{tot}_{core} - P^i_{core}/P^{tot}_{core}$. Of interest will be to see if there will be some noticeable consequences in the Scrape-Off Layer, e.g. changes in electron and ion temperatures, and if there will be effects on the overall energy balance of the system.

4.1.1 Attached case

The first simulations were performed with a target separatrix electron density of $n_e^{sep} = 1.5 \cdot 10^{19} m^{-3}$. Since the density remains approximately unchanged in the different cases, the temperature serves as a direct indicator of the plasma's thermal internal energy. As expected, increasing the core input power to electrons results in a corresponding rise in their internal energy (temperature) in the core, while the opposite occurs for ions. However, as shown in figure 4.2, this disparity appears to diminish approaching the separatrix, where temperature differences between cases become small, and ions are already hotter than electrons. Within the closed field line region, the high parallel thermal conductivity of electrons ensures that their temperature remains evenly distributed along the magnetic field lines. However, as one approaches the separatrix, radial transport mechanisms—such as turbulence (section 2.1)—become dominant, leading to a more pronounced outward loss of electron thermal energy. Consequently, the electron temperature decreases more rapidly than the ion temperature in this region, eventually becoming lower than T_i near the last closed flux surface (figure 4.4). In contrast, ions, due to their lower parallel thermal conductivity and slower radial transport, retain more thermal energy, resulting in a region where $T_i > T_e$ close to the separatrix.

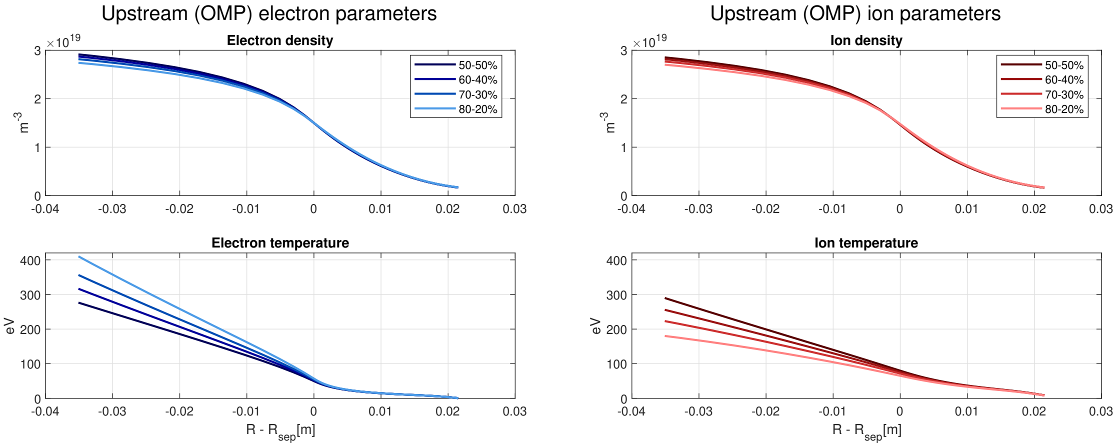

(a)

(b)

Figure 4.2: Upstream plasma parameters - percentage power distribution represents $P^{e}_{core}/P^{tot}_{core} - P^{i}_{core}/P^{tot}_{core}$% - *Power split*

To have a better understanding on the physical mechanisms that lead to the observed differences in the temperature profiles, a power balance analysis was performed starting from the core region. As we can see in figure 4.3b, the difference in input power on electrons and ions tends then to re-distribute because of collisionality due to the large temperature difference between electrons and ions, following the law

$$Q_{\Delta} = \frac{3m_e}{m_i} n_e \nu_{ei}(T_e - T_i) \propto \frac{n_e^2}{T_e^{3/2}}(T_e - T_i) \tag{4.3}$$

where the total power exchanged for collisional processes is computed in the various regions (figure 4.3b) of the tokamak cross-section as

$$Q_{reg} = \int_{V_{reg}} Q_{\Delta} dV \tag{4.4}$$

where positive values of Q_{Δ} mean transfer of power from electrons to ions. Indeed, we see an increasing trend of power transferred from electrons to ions at increasing(decreasing) input electron(ion) power in the core. Comparing the figures in 4.3 show that the power gained by ions at the separatrix (OUT-IN in figure 4.3a) are approximately equal to the one exchanged in the core for collisionality. Then, the remaining power losses for electrons, in addition to the collisional heat transfer, come from radiative effects.

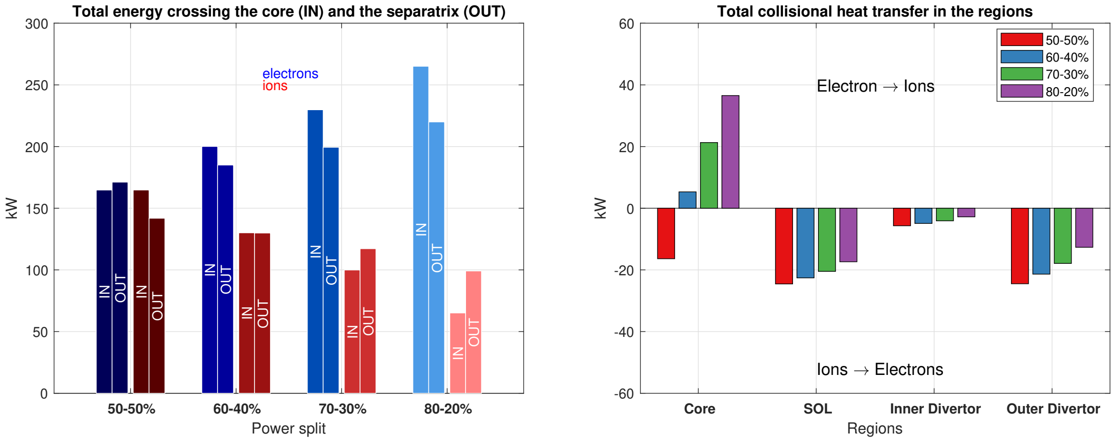

(a) (b)

Figure 4.3: a) Power transport in the core b) Collisional heat transfer in the regions - refer to figure 4.1 for the identification of the regions

As can be appreciated better in figure 4.4, right at the separatrix the electron temperature difference among the cases is small compared to the change of ion temperature, which is substantial ($\approx 20eV$ between the two opposite cases), for the reasons explained earlier. Crossing the separatrix (dot-dashed line in figure 4.4) and moving further into the Scrape-Off Layer, temperature variations among the different cases become negligible. This because the power is rapidly transported downstream due to the strong classical conductivity (more powerful for electrons wrt ions), as described by equation (3.9). Indeed, temperatures towards the walls, i.e. in the last flux surface in the computational domain, remain completely unaffected, contrary to initial expectations.

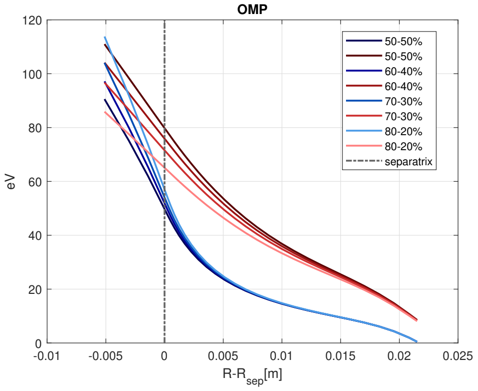

Figure 4.4: Temperatures in the outer core and in the SOL - Outer Mid Plane. Electrons in blue, ions in red

The targets appear to be only marginally influenced across the different cases. The inner target shows slightly more variation compared to the outer one, but in both instances, the modifications to the radial profiles are minor. This outcome is somewhat unexpected, as supplying more power to the electrons and less to the ions should intuitively result in electrons carrying more power to the targets, while ions would carry less. So where does this power go? It appears that the energy redistributes progressively across the different regions. A more in-depth analysis follows with the power balance in the regions.

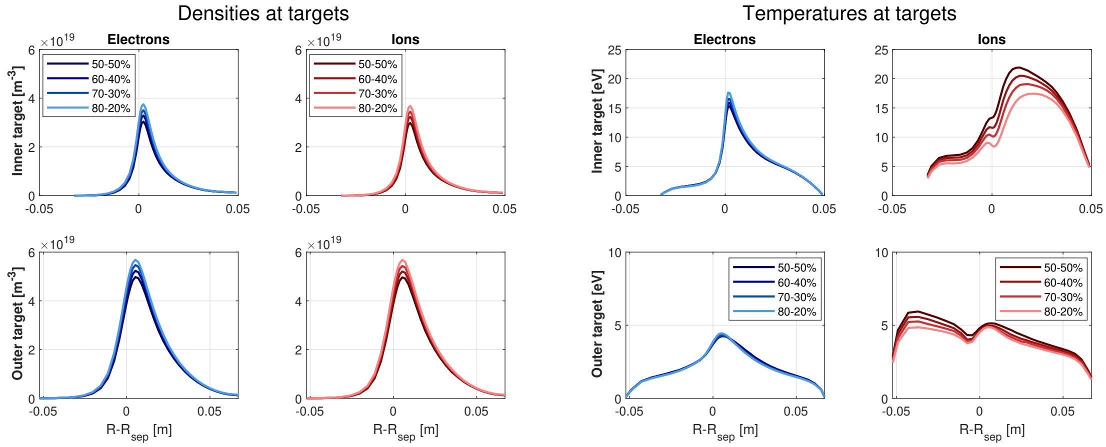

(a) (b)

Figure 4.5: Target plasma variables - *Power split*

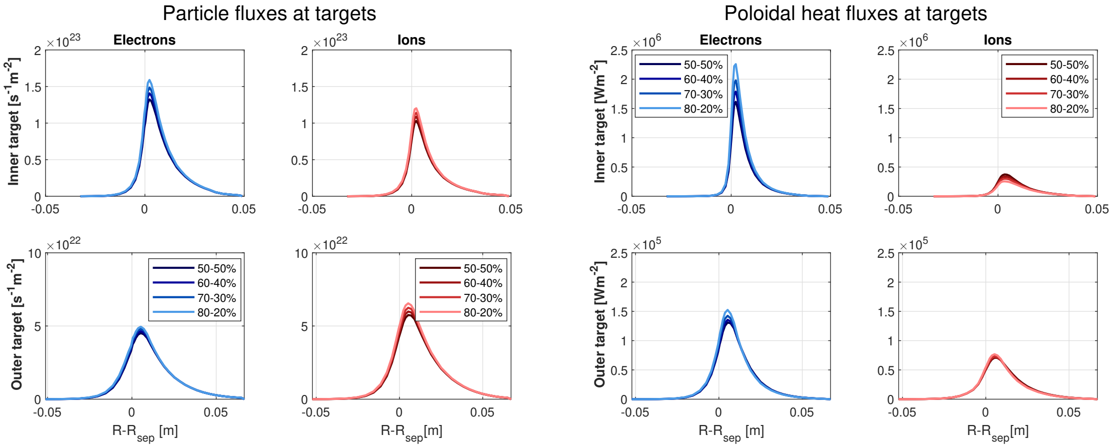

(a) (b)

Figure 4.6: Target plasma fluxes - *Power split*

4.1.2 Internal energy balance

The aim of this this study is to give an answer to the last question, i.e. why the variables at targets show almost unchanged trends in the different cases. Hence, a power balance analysis, based on the energy fluid equations ((3.25), (3.28)) implemented in SOLPS-ITER (section 3.2), is performed. The first region analysed is the Scrape-Off Layer, on both the *internal energy balance*, section 3.2.2, for electrons and ions

$$Q_{sep} = Q_{wall} + Q_{ID} + Q_{OD} + Q_{loss} \tag{4.5}$$

where Q_{sep} is the total power crossing the separatrix from the core (OUT value in figure 4.3a), Q_{wall} is the power deposited to the wall, Q_{ID} and Q_{OD} are the power entering into the inner and outer divertor legs respectively and Q_{loss} is the sum of the volumetric sources and sinks (corresponding to

S^h in equations (3.25) and (3.28))

$$Q_{loss} = \int_{SOL} S^h dV \tag{4.6}$$

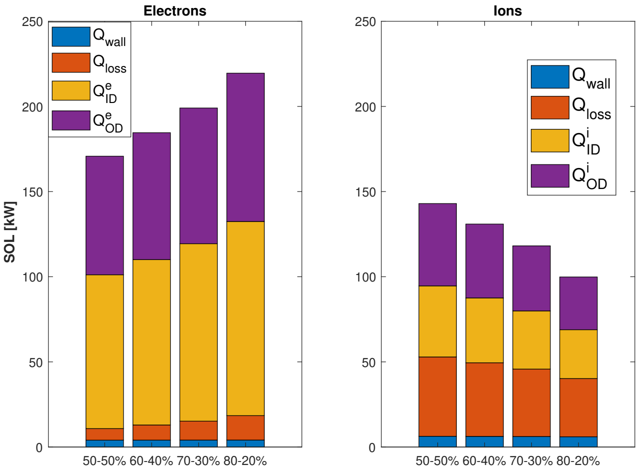

Figure 4.7: Internal energy balance in the Scrape-Off Layer - *Power split*

Figure 4.7 clearly tells us that the electron power entering in both divertor legs is increasing with increasing electron input power in the core, while the exact opposite happens for the ions. Remarkably, the total power entering the legs—the sum of electrons and ions—remains approximately unchanged. However, there is a slight shift in the power distribution from an initial $50-50\%$ split to an $80-20\%$ division as the power increases by approximately 10 kW between the two extreme cases. A similar trend is observed in the overall energy losses as well. The power deposited on the wall stays always approximately the same, which is consistent since nothing in perpendicular energy transport has been modified and the radial temperature drop is slightly different.

Going into the balance in the divertor legs

$$Q_{*D} = Q_{*T} + Q_{loss} \tag{4.7}$$

$$Q_{loss} = \int_{*Divertor} S^h dV \tag{4.8}$$

where $*$ stands for I (Inner) or O (Outer), thus Q_{IT} and Q_{OT} are the power deposited at the inner and outer target respectively, while Q_{loss} are the losses in the two different legs.

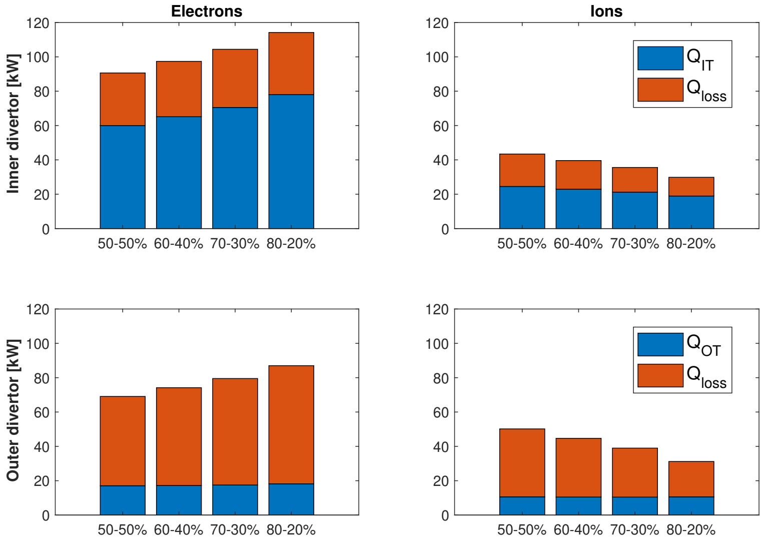

Figure 4.8: Internal energy balance in the divertor legs - *Power split*

Looking at figure 4.8 can be immediately noticed that the power reaching the targets, for both ions and electrons and in every case, remains almost unchanged while the main differences are the volumetric losses along the legs, showing increasing power losses for ions at increasing electron input power and the contrary for ions. As for the balance in the SOL, combining the electron and ion losses leads to a nearly constant value in the various cases. In fact, looking to the *total* volumetric power losses f_{pwr} (which accounts to the total energy balance) in the outer leg (see next section, 4.1.3, figure 4.12) from analytical calculations with the 2 point model formatting (section 3.1), we see that there are no substantial changes, telling us that the power and the losses are just re-distributed between electrons and ions. This justifies what said in the above discussion about target values in figures 4.5 and 4.6.

4.1.3 Detached case

In a *detached* case, where detachment, section 1.3.1, is controlled by setting a higher electron density at the separatrix, $n_e^{sep} = 2.5 \cdot 10^{19} m^{-3}$, the simulation is again run in feedback mode. This was done to examine whether the two different scenarios exhibit similar behavior or not.

As in the attached case, we observe in figure 4.9b a power redistribution in the core due to collisional heat exchange, which is even more pronounced due to the quadratic dependence of Q_Δ on the density n, equation (4.3). As before, the power gained by ions at the separatrix is approximately equal to the amount transferred through collisional processes in the core (Figure 4.9), with a slightly higher contribution from radiation losses.

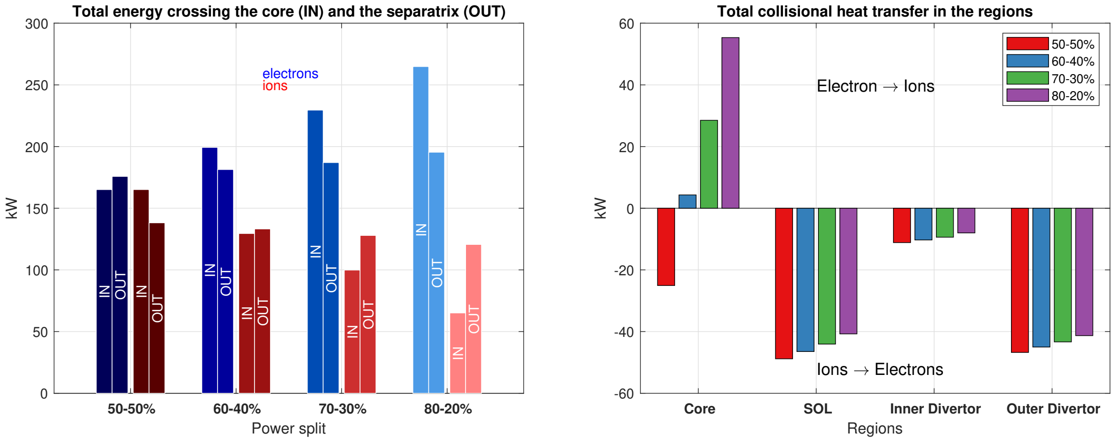

(a) (b)

Figure 4.9: a) Power transport in the core b) Collisional heat transfer in the regions - refer to figure 4.1 for the identification of the regions

The targets display no significant changes despite the different boundary conditions imposed, indicating that strong volumetric power losses, particularly due to increased impurity radiation, effectively eliminate any discrepancies observed upstream.

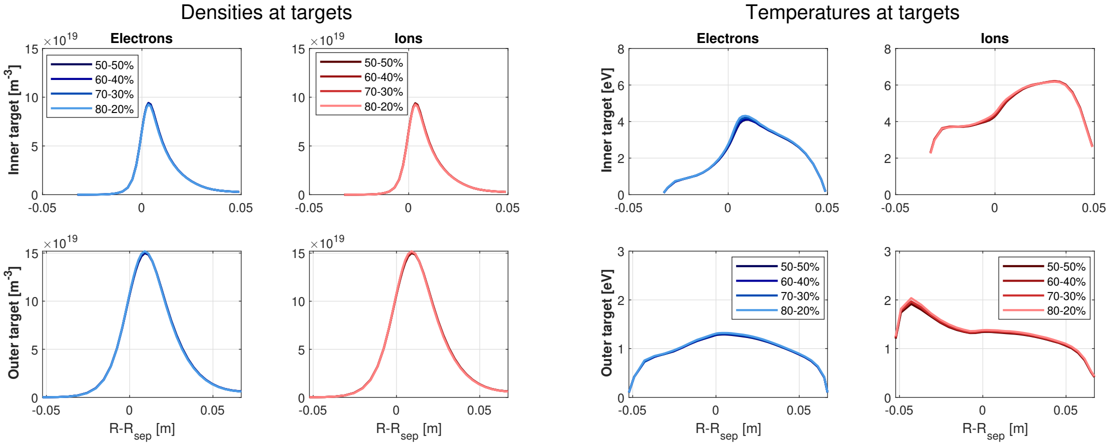

(a) (b)

Figure 4.10: Target plasma variables

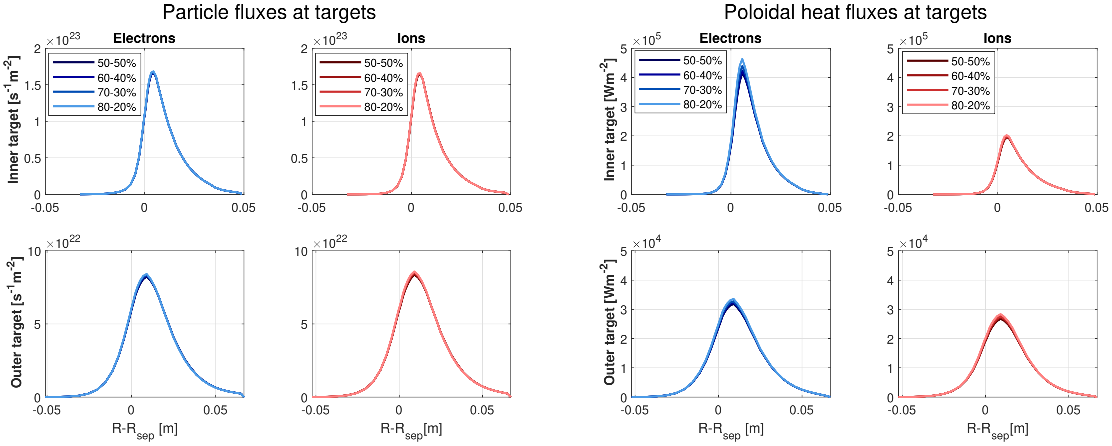

(a) (b)

Figure 4.11: Target plasma fluxes

2 Point Model Formatting analysis

To quantify the previously cited volumetric losses we rely on the 2 point model formatting (section 3.1). Figure 4.12 is showing analytical calculations of the volumetric momentum (f_{mom}) and power losses (f_{pwr}) with the 2PMf on the outer leg. The left y axis (black) is the scale of the volumetric losses f, while the right y axis (blue) is the scale of the relative percentage error, computed as $\epsilon = \frac{1-f}{f} \cdot 100$. As referred in section 3.1 and in [59], we calculate both f_{mom} and f_{pwr} without volume integration, *wovi* (f SOLPS in figure 4.12), reversing equations (3.13) and (3.12) respectively. On the other hand, we compute them with volume integration, *wivi* (f 2PMF in figure 4.12), as in equations (3.18) and (3.17). The relative percentage error is calculated for the 2PMf wovi. As we can see from figure 4.12, 2PMf wovi and wivi match pretty well.

In the detached case, such as in the attached one, the total power losses between the different power split cases are negligible. Of more interest is to notice the big difference between the attached and detached cases, where it is shown that in the high density case the volumetric power losses are substantially larger, as we would have expected from what mentioned in section 1.3.1 and from 2PM analysis, confirming what said before.

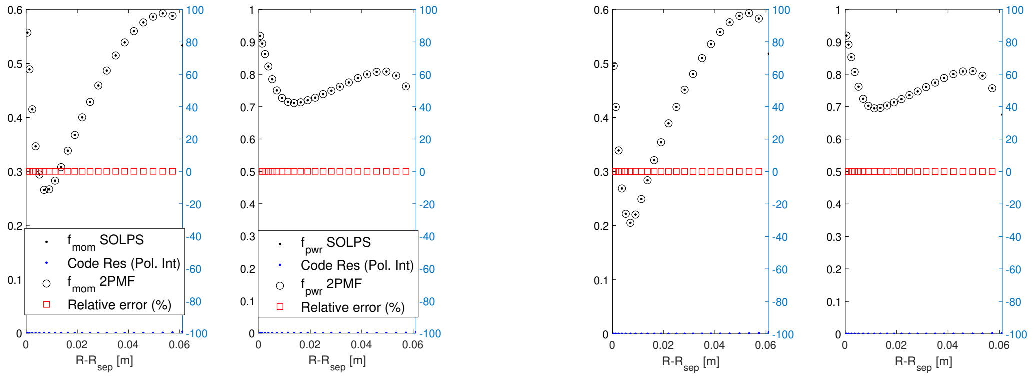

(a) Attached - $50-50\%$

(b) Attached - $80-20\%$

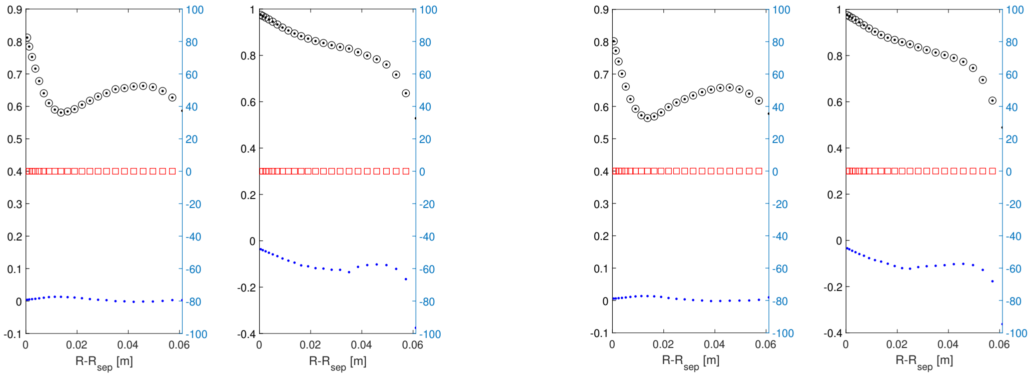

(c) Detached - $50-50\%$

(d) Detached - $80-20\%$

Figure 4.12: 2PMf on the outer divertor - comparison between the attached and detached case with the two opposite power splits

4.2 Anomalous cross-field energy diffusivity

The starting **reference** value taken was the one used in past simulations, i.e. $\chi_e = \chi_i = 1m^2/s$ constant. The scan will be performed for values starting from a minimum of $0.2m^2/s$ to a maximum of $2m^2/s$ with steps of 0.2, so covering a range of values close to reality. However, keeping their value constant all over the outer core and Scrape-Off Layer region could be a wrong assumption too. In SOLPS-ITER there is the possibility to shape these coefficients radially modifying the input file in the B2.5 code named *b2.transport.inputfile*. The way the anomalous cross-field power transport is defined in SOLPS-ITER is:

$$q_{s,y}^{AN} = -k_{s,y}^{AN} \frac{\partial T_s}{h_y \partial y} \tag{4.9}$$

$$k_{s,y}^{AN} = n_s \chi_s^{AN} \tag{4.10}$$

4.2.1 Ion χ_i

As previously mentioned, modifying χ_i affects perpendicular ion power transport within the simulation domain, with particular interest in the ion temperature behavior in the Scrape-Off Layer (SOL).

The first noticeable detail in Figure 4.13b is that altering the anomalous cross-field ion transport coefficient significantly changes the steepness of the ion temperature T_i profile in the core. This trend is consistent with how perpendicular power transport is defined in SOLPS-ITER (Equation (4.9)) and is further influenced by the fact that the core boundary condition is of the Neumann type, with a constant heat flux imposed. Consequently, in cases with a lower coefficient value, the weaker perpendicular transport necessitates a steeper temperature gradient to compensate. Additionally, electron temperature in the core is also slightly affected by changes in the coefficient. Upstream density is also marginally affected by this parameter.

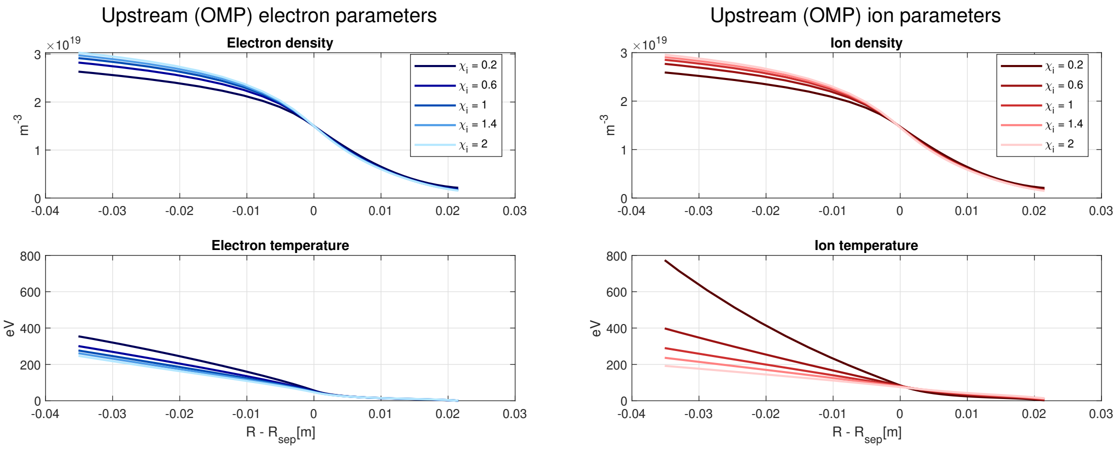

(a) (b)

Figure 4.13: Upstream plasma variables - χ_i

More interestingly, as expected, ion power transport is also influenced in the SOL as can be seen in figure 4.14. At higher χ_i values, ion temperatures increase in the far SOL, while the opposite occurs for lower values. This indicates that strengthening cross-field conductive power transport significantly impacts the overall energy distribution, as ions, unlike electrons, do not exhibit strong parallel conduction. Consequently, an increase in χ_i enhances ion energy diffusion across flux surfaces, altering the balance between radial and parallel transport and leading to noticeable modifications in the overall heat flux structure.

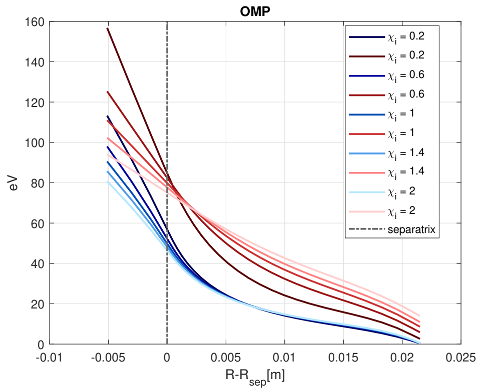

Figure 4.14: Temperatures in the outer core and in the SOL - Outer Mid Plane. Electrons in blue, ions in red - χ_i

Examining the target profiles in figures 4.15 and 4.16, no significant changes are observed, except for the electron heat flux at the inner target (Figure 4.16b). Surprisingly, ion heat flux at both targets remains nearly unchanged, which may be attributed to a balance between the potentially higher heat flux from upstream and the enhanced cross-field transport along the divertor legs. However, one would expect at least the ion temperature to vary at the targets. Indeed, as χ_i increases, ion temperature T_i rises at both targets because more energy is entering in the SOL from the core, given that no modifications were made to poloidal transport mechanisms. It is not trivial to understand why the ion poloidal heat flux at targets, figure 4.16b, does not change while the ion temperature does. An explanation to this phenomena could be in the component terms of the ion heat flux, i.e. conducted and convected, $q_i = q_{cond,i} + q_{conv,i}$ where the convected heat flux can be written as $q_{conv,i} \approx \Gamma_i T_i$ with Γ_i the ion particle flux. We see from picture 4.16a that at high χ_i the particle flux density is little lower, which means that ion temperature has to be higher so that the ion heat flux stays constant. The question now is why this ion heat flux is unchanged among the cases? This will be studied in the *internal energy balance* analysis.

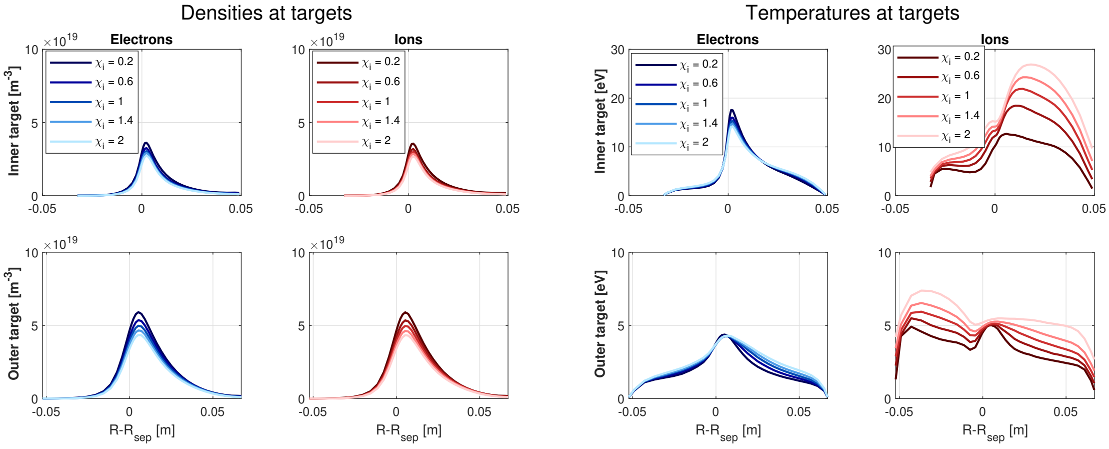

(a)

(b)

Figure 4.15: Target plasma variables - χ_i

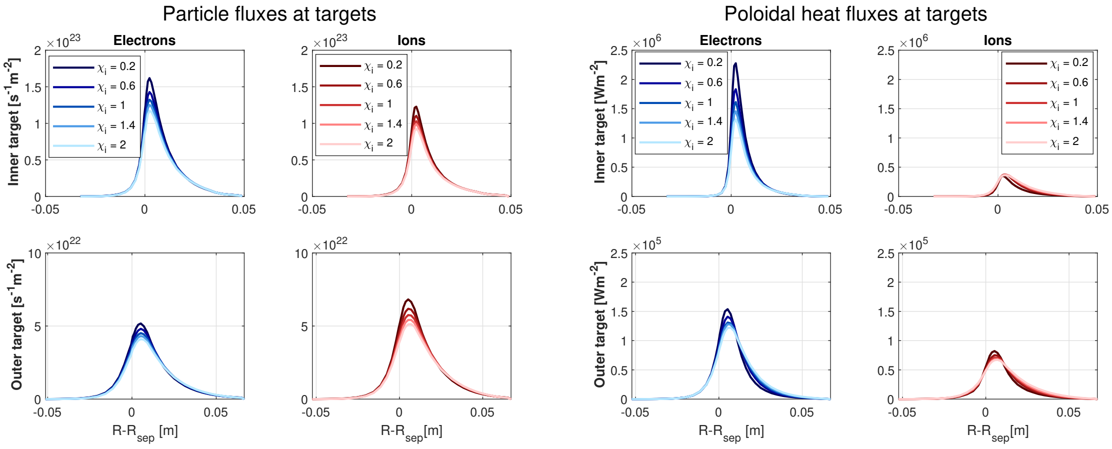

(a)

(b)

Figure 4.16: Target plasma fluxes - χ_i

Internal energy balance

The internal energy balance analysis is performed to have a clearer picture of how the power gets re-distributed in the different regions while changing the ion anomalous cross-field energy coefficient. Figure 4.17 shows that at low χ_i values more electron and less ion power are crossing the separatrix (the sum of the contributions in the bar of figure 4.17) from the core, because ion power in the core region struggles going toward the SOL due to depowered cross-field ion heat transport. Most of the power gained by electrons is for collisional heat transfer, given the high temperature difference.

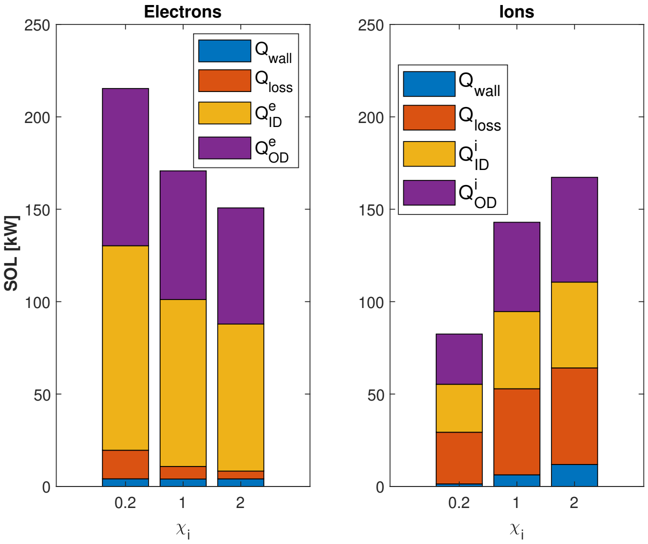

Figure 4.17: Internal energy balance in the Scrape-Off Layer - χ_i

Looking figure 4.18 we see what we would have expected from figure 4.17, increasing χ_i lower the electron power entering in the divertor legs while the contrary happens for the ions. As we can notice for ions, the power reaching the targets stays approximately constant (confirming what was seen before in figure 4.16b) while the overall power entering in the divertor legs is different among the cases, i.e. the power losses in the divertor tend to level out the values of power going to the target. This may be due to the fact that at high χ_i, even if more power is entering in the SOL and then coming to the divertors, the increased anomalous cross-field energy transport steals power from the parallel channel resulting in increased losses.

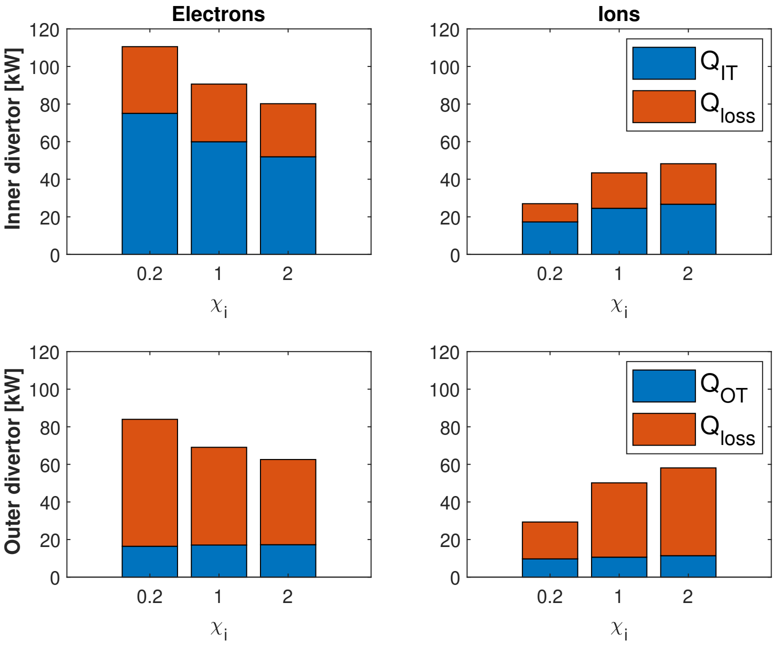

Figure 4.18: Internal energy balance in the divertor legs - χ_i

4.2.2 Electron χ_e

Here, we observe the same behavior described in the previous section, namely that the steepness of the electron temperature profile in the core (Figure 4.19a) varies significantly with changes in χ_e for the same underlying reason. Meanwhile, upstream ion temperature and both electron and ion densities exhibit only minor changes with varying χ_e.

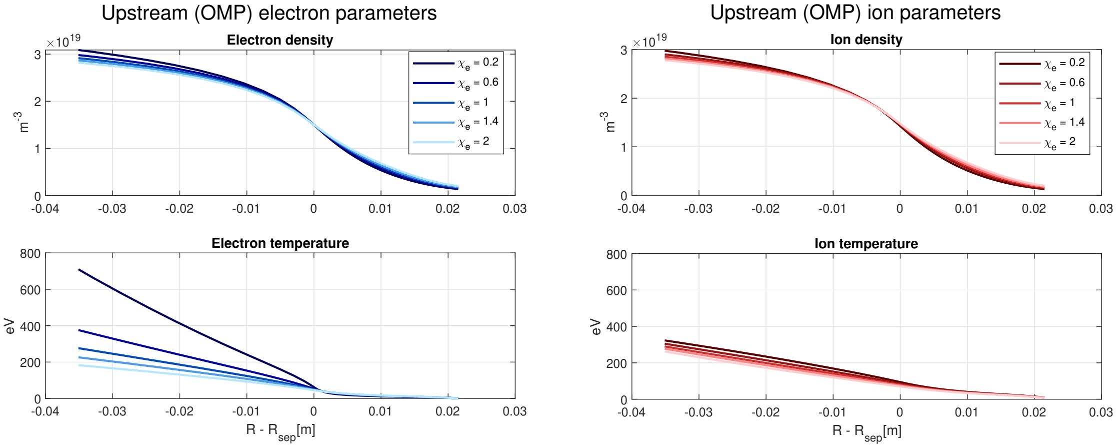

(a)

(b)

Figure 4.19: Upstream plasma variables - χ_e

However, unlike in the ion case, cross-field power transport for electrons appears to be less effective in the Scrape-Off Layer. This can be explained by the fact that parallel heat conduction is the dominant energy transport mechanism for electrons due to their small mass, effectively minimizing the impact of variations in the anomalous electron cross-field energy transport coefficient. As we see in figure 4.20, after the separatrix (dot dashed line) the electron temperature shows little variations, to the far SOL where this difference is negligible. Even the ions show substantial temperature changes in the Scrape-Off Layer. This is because in the different cases different amounts of ion energy are entering in the SOL and these struggle to level out for the weaker ion parallel conduction wrt electrons, thus transporting slowly the ion power downstream.

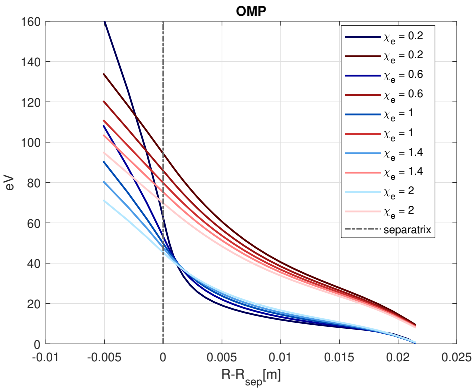

Figure 4.20: Temperatures in the outer core and in the SOL - Outer Mid Plane. Electrons in blue, ions in red - χ_e

The anomalous electron energy transport coefficient appears to significantly impact the power balance at the targets, as shown in Figures 4.21 and 4.22. Specifically, at higher χ_e, we observe progressively lower temperatures and parallel heat flux for both ions and electrons, highlighting the effectiveness of perpendicular power transport in the divertor legs. To have a better comprehension, an *internal energy balance* analysis is performed hereafter.

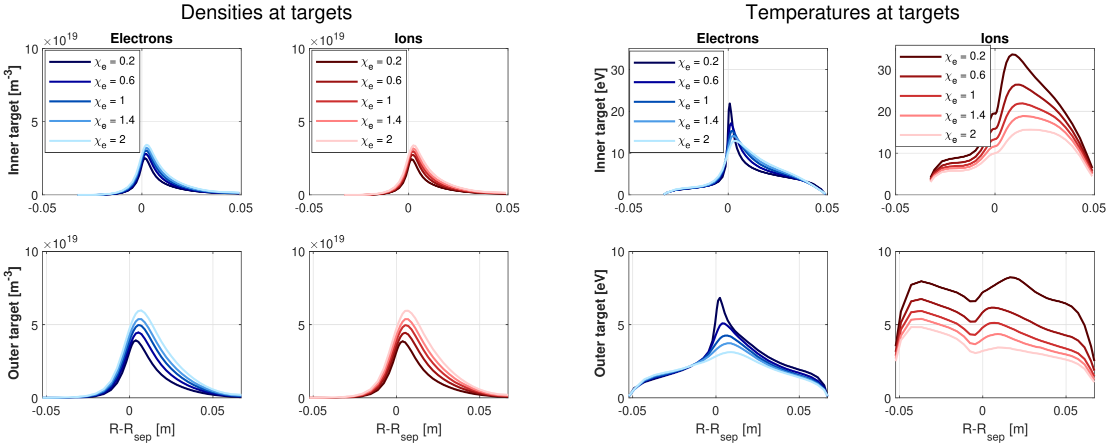

(a) (b)

Figure 4.21: Target plasma variables - χ_e

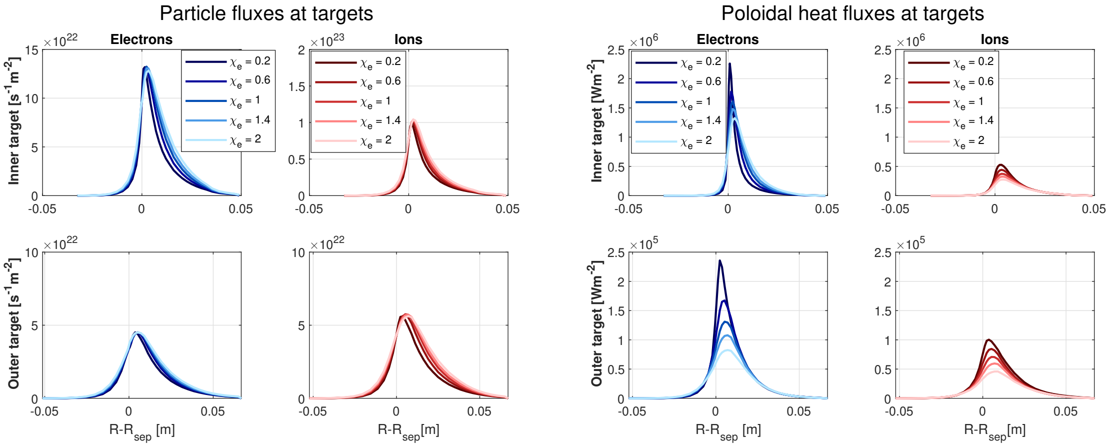

(a) (b)

Figure 4.22: Target plasma fluxes χ_e

It is both interesting and important to emphasize that modifying a parameter governing electron power transport influences both species more significantly than χ_i affects the ions alone. This indicates that electrons dominate overall power transport in the TCV.

Internal energy balance

The *internal energy balance* analysis is done with the goal of providing a sharper picture of the overall energy transport and to understand better what is actually happening at the targets. Figure 4.23 shows the power balance in the Scrape-Off Layer, illustrating a clear trend of increasing electron power crossing the separatrix (the sum of the contributions in the bar of figure 4.23) and entering in the SOL while increasing χ_e. This was expected, since at low χ_e the cross-field electron energy transport is even weaker than it usually is, due to the very strong parallel Spitzer Harm electron heat conductivity. It means larger electron energy retention in the core, promoting the exit of a bigger amount of ion power gained mainly by electron-ion Coulomb collisions.

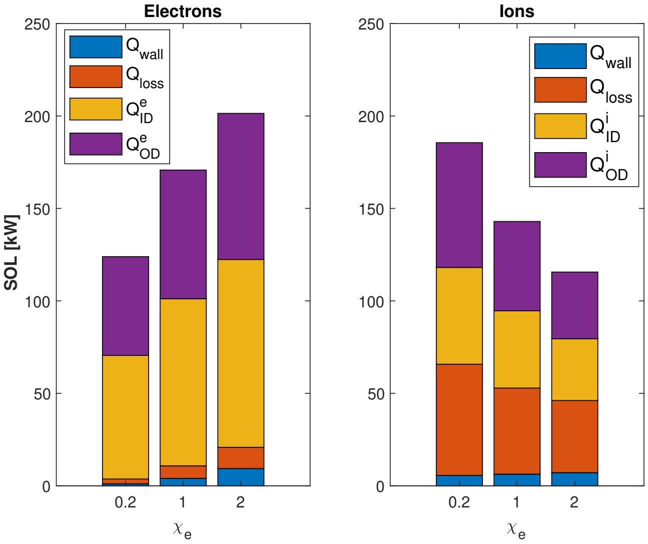

Figure 4.23: Internal energy balance in the Scrape-Off Layer - χ_e

As we can see in figure 4.24, the increasing and decreasing power entering in the SOL (figure 4.23) of electrons and ions respectively at increasing χ_e results in equal trend in terms of power entering into the divertor legs. The only strange pattern is in the inner divertor for the electrons in figure 4.24, because the power reaching the respective target grows rather than decreasing. Calculating the percentage of power losses over the total power entering in the inner divertor, $Q_{loss}/Q_{ID} \cdot 100$, it results that for each case it is constant ($\approx 30\%$), as if the cross-field transport was not affecting at all the electron energy transport in this divertor leg. This may be due to the shortness of this leg. Instead, in the outer divertor leg the electron power losses are increasing, resulting to lower power reaching the target at increasing χ_e. It means that in the longer divertor leg the stronger cross-field transport tends to dissipate more effectively the parallel electron energy flowing towards the target. Ions are mainly affected by the difference in the amount of power entering to the SOL from the core region, since the percentage amount of power losses in both the SOL and the divertor legs stays constant among the different cases.

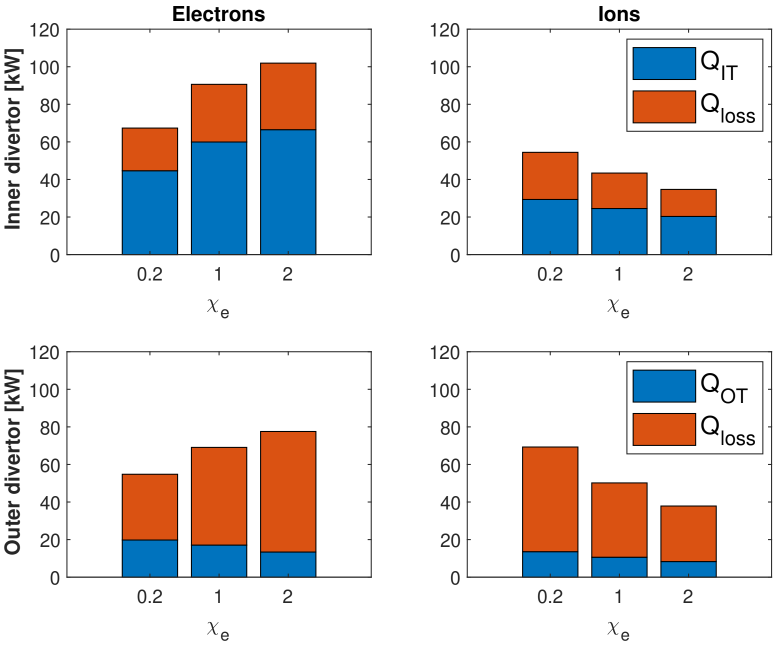

Figure 4.24: Internal energy balance in the divertor legs - χ_e

4.3 The ion flux limiter

The **reference** value was of cflmi = 10, going to an upper limit of 50 down to a minimum value equal to 0.1. The way it is implemented on SOLPS-ITER is

$$q_{ix,cond} = -k_{i,x}^{lim} \frac{\partial T_i}{h_x \partial x} \tag{4.11}$$

$$k_{i,x}^{lim} = \frac{1}{1 + \frac{q_{ix,cond}^{unlim}}{cflmi \cdot n_i v_i T_i}} k_{ix}^{unlim} \tag{4.12}$$

For lower densities the heat flux limiters are expected to become more important [81], while at higher densities, i.e. close to a detached regime, the flux limiters have a lower impact.

Modifying the ion flux limiter directly impacts parallel conductive ion power transport. At lower cflmi values, poloidal ion heat transport is more constrained, meaning that cross-field ion energy transport becomes dominant. As a result, ion temperatures in the far SOL, closer to the wall, are higher, as shown in Figure 4.25b. As expected, electron temperature remains unaffected, and no significant changes are observed in the upstream density profile.

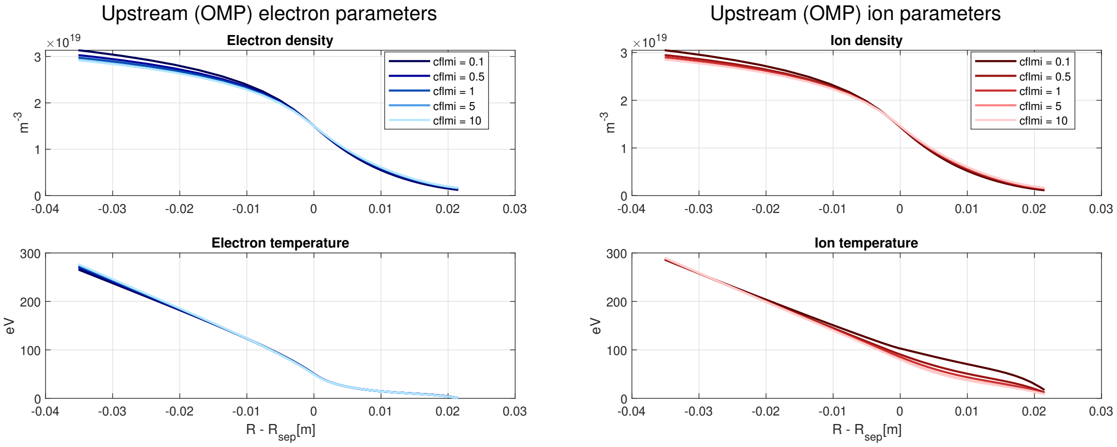

(a) (b)

Figure 4.25: Upstream plasma variables - *cflmi*

The radial temperature profile in figure 4.26 clearly shows the very weak conduction losses for ions in the SOL for low ion flux limiter values, translated into larger ion internal energy close to the wall. Similarly to what was said in section 4.1, within the closed field line region, the limited parallel thermal conductivity of ions, as modeled by the ion flux limiter parameter, results in less energy retention. Instead, examining the ion temperature drop along field lines outside the separatrix (figure 4.27b), we see that at the lowest cflmi value, a very steep temperature drop occurs in the X-point region and at the entrance to the SOL-outer target. At low ion flux limiter values, volumetric power losses in the flux tubes are thought to be higher and it will be analysed later in section 4.3.1. Conversely, as cflmi increases, this temperature drop becomes more gradual. Electron temperature also appears to be influenced in the divertor region, although it remains unchanged upstream. Surprisingly, densities (figure 4.27a) undergo significant modifications upon entering the divertor region, with the most notable changes occurring at the targets, where both electron and ion densities increase substantially at low cflmi values.

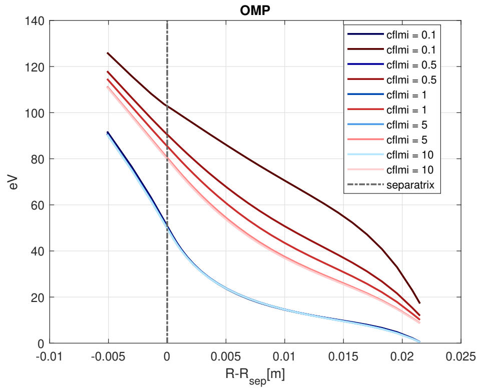

Figure 4.26: Temperatures in the outer core and in the SOL - Outer Mid Plane - *cflmi*

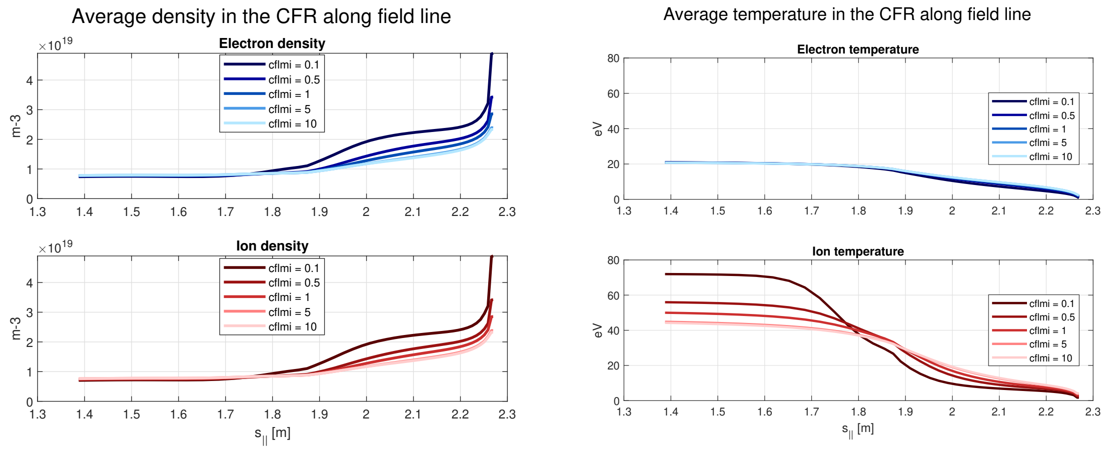

(a) (b)

Figure 4.27: Trend of variables from OMP towards the outer target, averaged in the common flux region (CFR) from OMP to the target.

As expected, the ion heat flux at the targets (figure 4.29b) is influenced by modifications to the ion flux limiter. In particular, as we see in figures 4.28 and 4.29 is that the outer leg, the longer, is the one mainly affected by the modification of the *cflmi*. What we would expect from this parameter scan are changes at the targets in terms of ion energy balance and thus temperature. Indeed it is, ion temperature is greatly affected by this parameter (figure 4.28b). However, the most surprising result is the strong influence of the ion flux limiter on electrons, contradicting initial expectations. Particularly relevant are the outer target values of electron density $n_{e,OT}$ (figure 4.28a) and temperature $T_{e,OT}$ (figure 4.28b), which decrease and increase, respectively, at higher cflmi values. This aligns well with previous validation work on SOLPS-ITER simulations of the TCV SILO configuration done in [40]. Furthermore, it is evident and curious to see from these figures that the effect of the ion flux limiter saturates for values $cflmi \geq 5.0$.

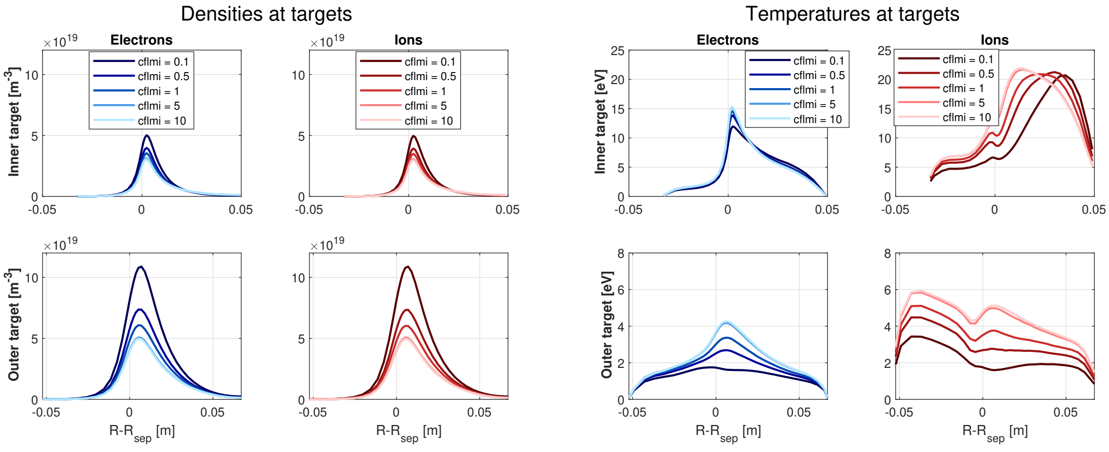

(a) (b)

Figure 4.28: Target plasma variables - *cflmi*

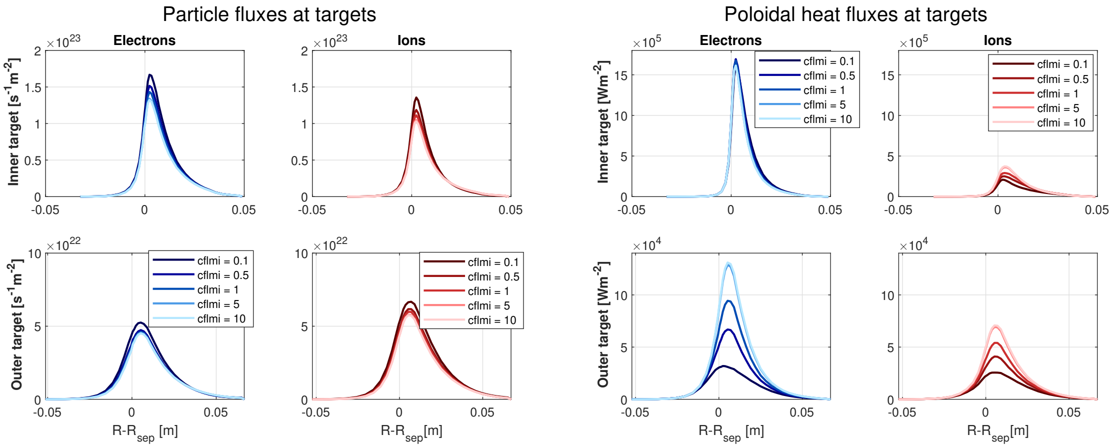

(a) (b)

Figure 4.29: Target plasma fluxes - *cflmi*

A natural question arises: how does the ion flux limiter affect electron energy transport in the outer divertor region? And how does the density get influenced so much by the change of a parameter that modifies power transport? It is not at all trivial to understand why the energy transport of the electron species is so significantly influenced by the change in the ion flux limiter parameter, which directly modifies ion energy transport instead. This is even more puzzling considering that upstream, electron quantities remain nearly unchanged, while at the outer divertor, the electron energy balance appears to be strongly altered. One might think that the thermal coupling between electrons and ions is particularly effective in the outer leg, also due to the higher divertor density compared to the scrape-off layer, whereas in the SOL, it remains very weak. The change in electron temperature at the outer target is thought to be responsible also of the variations in electron and ion densities. The changes in electron temperature at the outer target are thought to be responsible for the variations in electron and ion density at the target itself. This is because the electrostatic potential drop Φ, as displayed in figure 4.30b, in the sheath (section 2.2.3) is proportional to the electron temperature, $\Phi \approx 3T_e$. Therefore, at higher temperatures (under high *cflmi* conditions), the target potential will be higher, more effectively repelling electrons (equation (2.52)).

As shown in Figure 4.30a, the neutral density at the outer target is also significantly influenced by this parameter. At low *cflmi* values, less power reaches the target, leading to a cooler divertor condition. As a result, the ionization rate near the target decreases, causing the ionization front to shift upstream into a hotter region where ionization is more efficient. Additionally, electron-ion recombination at the target becomes more prominent, further increasing the local neutral density. Moreover, as discussed previously, the lower potential drop in this regime results in ions reaching the target with reduced energy, decreasing the likelihood of sputtering and limiting power-driven neutral depletion.

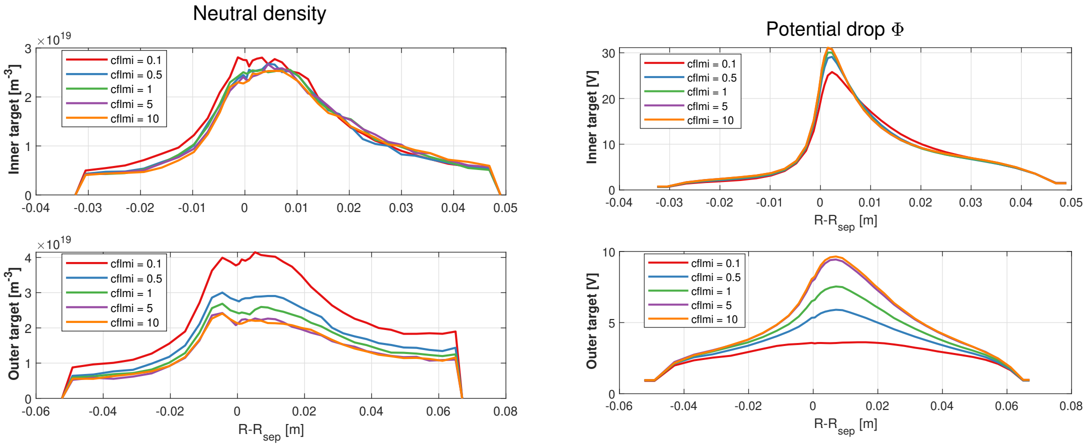

(a)

(b)

Figure 4.30: Neutral density and potential drop at the divertor targets

The main point of interest stays on the power balance, given the large discrepancies between different cases. An important question arises: where does this difference in power go? To address this, the following section will present a power balance analysis.

4.3.1 Power balance

Starting from a basic analytical study, specifically the two-point model formulation, we can retrieve the volumetric loss factors from the code output (see Section 3.1) as it was done in section 4.1.3. A first comparison is conducted between two extreme cases, cflmi = 0.1 and cflmi = 10. As shown in figure 4.31, the higher values of f_{pwr} in the low flux limiter case indicate that volumetric power losses are greater compared to the high flux limiter case. A similar trend is observed for the fraction of momentum losses f_{mom}.

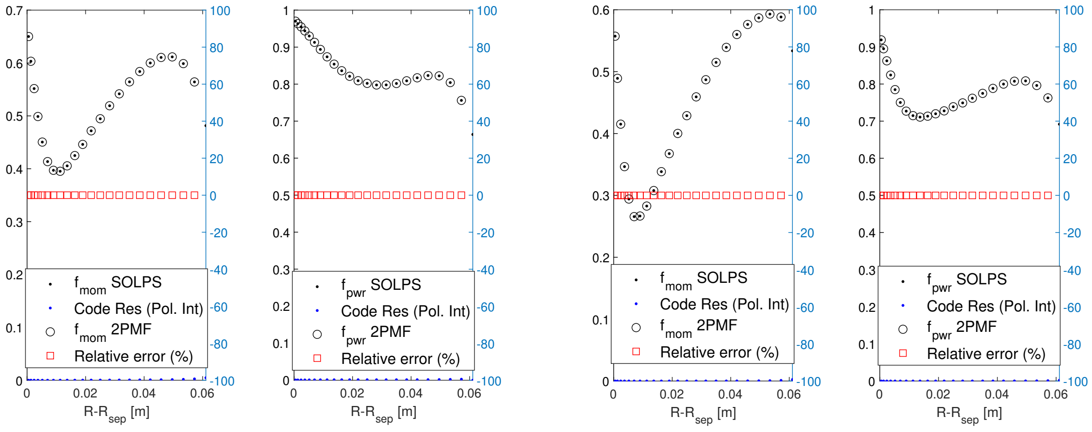

(a) **cflmi = 0.1**

(b) **cflmi = 10**

Figure 4.31: 2PM formatting analysis on the two opposite cases

This raises the question: what are these losses, and how does power transport behave in the outer divertor? Figure 4.32 illustrates the trend of total power entering the outer divertor as it moves toward the target. Significant differences emerge between the two opposite cases. At *cflmi* = 0.1, a large amount of electron power crosses the entrance boundary, whereas ion power remains minimal. While this is not surprising, what stands out is the downstream evolution, where ions lose very little energy while electrons undergo a substantial drop, ultimately resulting in both species losing the same amount of power to the target wall. In contrast, at cflmi = 10, little less electron power crosses the outer divertor entrance while, due to the less restricted ion conductivity, a higher amount of ion power enters the divertor. However, less electron power is lost in the divertor region, suggesting that it is transported more efficiently, while, proportionally, ion power losses increase.

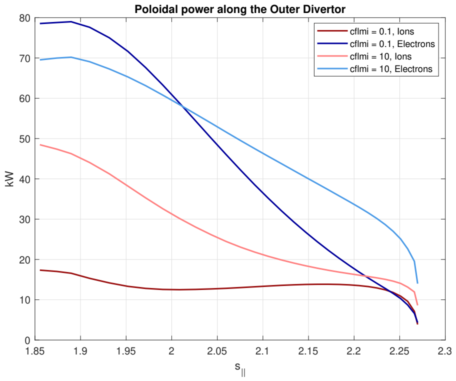

Figure 4.32: Total power entering in the outer divertor CFR and flowing towards the target

Internal energy balance

The next step is to study the power balance of electrons and ions separately, looking into their *internal energy balance equations* (equations (3.25) and (3.28)) with the aim of finding out the power losses characterizing the different cases. In the Scrape-Off Layer, figure 4.33, the electron energy balance is less interesting, since the total power crossing the separatrix (the whole bar in figure 4.33) and entering in the SOL is not much affected and also the redistribution in terms of power going into the divertor legs (Q^e_{ID} and Q^e_{OD}) and power losses Q_{loss} are not substantial. Differently for the ions, whose energy balance changes dramatically. Increasing the ion flux limiter results in a clear trend of progressive power loss reduction, while the power entering into the divertors (Q^i_{ID} and Q^i_{OD}) grows significantly, demonstrating the effectiveness of the ion flux limiter in the ion power transport.

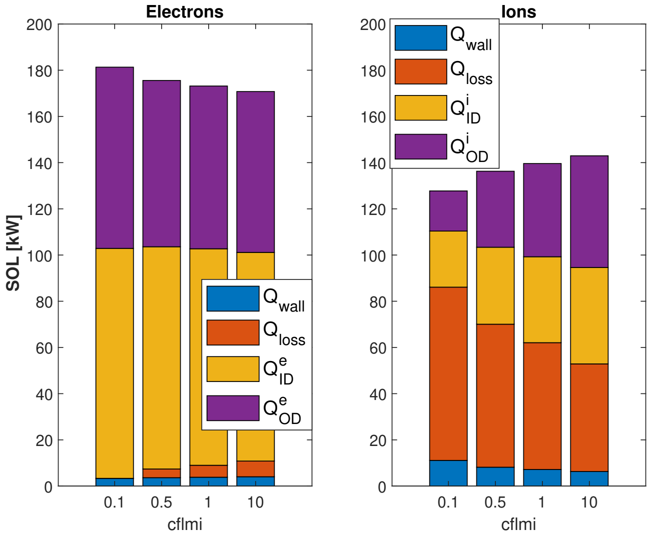

Figure 4.33: Internal energy balance in the Scrape-Off Layer - *cflmi*

Finally, figure 4.34 confirms what said before. The simple and main reason why more ion power is reaching the target is because the increased parallel heat flux (raising *cflmi*) means more power arriving to the divertor legs. Calculating the percentage of power losses in each case, e.g. $Q_{loss}/Q_{OD} \cdot 100$ for the outer divertor (where Q_{OD} is the total power entering, equal to the whole bar in figure 4.34), is equal and constant. The only difference stands in how much power is reaching the divertor entrance. The same cannot be told about the electrons, whose power crossing the divertor entrance is approximately equal in the various cases, but the power losses are decreasing resulting in more power reaching the target. This happens particularly at the outer target, where the reason could be the stronger electron-ion thermal coupling wrt the inner divertor leg.

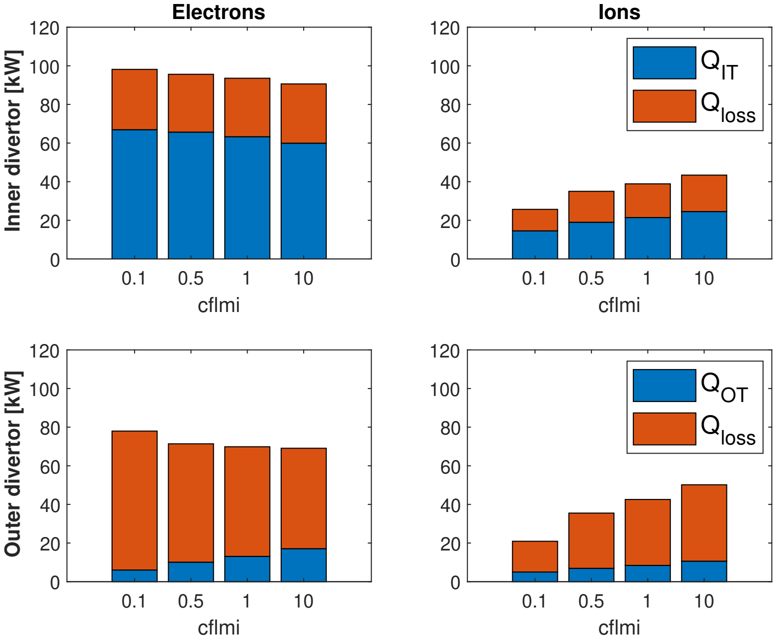

Figure 4.34: Internal energy balance in the divertor legs - *cflmi*

5. Conclusion and perspectives

This study has systematically investigated energy transport in the Scrape-Off Layer (SOL) of the TCV tokamak, focusing on the SILO baffled configuration with a Lower Single Null divertor. Using SOLPS-ITER, a parametric analysis was conducted to examine how variations in three key parameters—the input power split between electrons and ions at fixed total core power, the anomalous cross-field energy transport coefficients and the ion flux limiter—affect the energy balance, temperature profiles, and power deposition in different plasma regions.

The results reveal distinct effects of each parameter, highlighting the complex interplay between parallel and perpendicular transport mechanisms, collisional energy redistribution, and volumetric power losses in different tokamak regions. The study provides crucial insights into the dominant transport mechanisms in the TCV edge and contributes to improving SOLPS-ITER modeling capabilities.

The key findings are:

1. In the case of the *power split scan*, varying the fraction of input power to electrons and ions changes the core plasma conditions, it does not substantially alter the total power balance at the targets. Instead, the system efficiently redistributes energy through collisional processes, ensuring that the total power transported remains relatively stable across different cases. The biggest changes in temperature can be noticed in the core and near the separatrix while the impact on target conditions remain minimal.
2. Regarding the *anomalous cross-field energy transport coefficients scan*, the ion χ_i has main impacts just on the ions, affecting greatly upstream temperature due to the modified perpendicular transport. This gets reflected also at the target. In contrast, electron χ_e impacts both species, confirming that electron conduction regulates overall energy transport and power dissipation in the SOL and divertor legs. Its effectiveness can be seem especially in the divertor legs and directly at the targets, where parallel conduction gest weaker.
3. About the *ion flux limiter scan*, it directly modifies parallel ion heat conduction, restricting energy transport at low cflmi values. Change in ion flux limiter has a great effect on the volumetric power losses in the divertor legs. Indeed, it surprisingly influences electron temperature and density at the outer divertor target, despite the parameter explicitly controlling ion heat transport. The study confirmed that beyond $cflmi \approx 5$, the effect of increasing cflmi saturates, suggesting a natural limit to the influence of flux limiting on energy transport in the TCV SOL.

These findings provide valuable insights into energy transport mechanisms in the SOL and contribute to improving edge plasma modeling for tokamak operation and divertor optimization. The study highlights several key aspects that are critical for future fusion devices, including:

- The dominance of electron transport in power dissipation: electron conduction governs overall energy transport, making it the primary driver of power redistribution in the SOL and divertor legs.

- The importance of volumetric power losses: A significant portion of energy is dissipated through volumetric losses, particularly in the outer divertor leg
- The strong coupling between ion and electron energy transport: while ion flux limiters directly control ion conduction, their influence extends to electron energy transport and sheath potential structure, highlighting the complexity of plasma-wall interactions.

The insights gained from this study pave the way for further research and improvements in tokamak edge transport modeling. Several key areas for future investigation include:

- Inclusion of drift effects: extending SOLPS-ITER simulations to include drift terms, which could further clarify their role in cross-field transport and SOL structure formation
- Model the anomalous cross-field energy transport coefficients through the *b2.transport.inputfile*, where they can be shaped depending on the radius, so being able to better represent what happens in reality
- Experimental validation: comparing these simulation results with experimental data from TCV to refine transport models and improve the accuracy of anomalous diffusivity prescriptions
- Deepen the comprehension of the ion flux limiter to find the value that best represents the reality, particularly for cases where non-local heat flux regulation becomes dominant, since for the electrons the flux limiter has already been compared with kinetic models, which have been extensively studied due to their lighter mass and faster dynamics
- Impurity transport: investigating how impurity radiation, recombination, and neutral dynamics influence volumetric power losses

These advancements will enhance our understanding of plasma-wall interactions and support the development of next-generation divertor solutions for future fusion reactors, including ITER and DEMO. By refining our predictive capabilities for energy transport in the SOL, this work contributes to the broader goal of achieving sustainable, efficient, and well-controlled plasma confinement in fusion devices.

Bibliography

---

[1] Hannah Ritchie, Pablo Rosado, and Veronika Samborska. Climate change. *Our World in Data*, 2024. https://ourworldindata.org/climate-change.

[2] Jozef Ongena, Robert Koch, Robert Wolf, and Hartmut Zohm. Magnetic-confinement fusion. *Nature Physics*, 12, 2016.

[3] Arne Kallenbach, Matthias Bernert, R. Dux, Livia Casali, Thomas Eich, Louis Giannone, Albrecht Herrmann, R. M. McDermott, Alexander Mlynek, Hans Werner Müller, Felix Reimold, Josef Schweinzer, Marco Sertoli, Giovanni Tardini, Wolfgang Treutterer, Eleonora Viezzer, Ronald Wenninger, and M. Wischmeier. Impurity seeding for tokamak power exhaust: from present devices via iter to demo. *Plasma Physics and Controlled Fusion*, 55, 2013.

[4] Nicholas Walkden, Fabio Riva, James F. Harrison, Fulvio Militello, T Farley, John Omotani, and Bruce Lipschultz. The physics of turbulence localised to the tokamak divertor volume. *Communications Physics*, 5:1–10, 2022.

[5] Wensing. Drift-related transport and plasma-neutral interaction in the TCV divertor. *PhD thesis*, 2021.

[6] Peter C Stangeby. *Plasma Physics and Fusion Energy.* IOP, 2000.

[7] Xavier Bonnin, Wouter Dekeyser, Richard A. Pitts, David P. Coster, S. P. Voskoboynikov, and Sven Wiesen. Presentation of the new solps-iter code package for tokamak plasma edge modelling. 2016.

[8] M. Sala, Elena Tonello, Andrea Uccello, Xavier Bonnin, D. Ricci, David Dellasega, Gustavo Granucci, and Matteo Passoni. Simulations of argon plasmas in the linear plasma device gym with the solps-iter code. *Plasma Physics and Controlled Fusion*, 62, 2020.

[9] IEA. Net zero roadmap: A global pathway to keep the 1.5 °c goal in reach. *IEA*, 2023. https://www.iea.org/reports/net-zero-roadmap-a-global-pathway-to-keep-the-15-0c-goal-in-reach.

[10] H.-S. Bosch and G.M. Hale. Improved formulas for fusion cross-sections and thermal reactivities. *Nuclear Fusion*, 32(4), 1992.

[11] Georgeanne R. Caughlan and William A. Fowler. Thermonuclear reaction rates v. *Atomic Data and Nuclear Data Tables*, 40:283–334, 1988.

[12] Ambrogio Fasoli. Kinetic theory of plasmas. *lecture notes from Plasma 2 course, EPFL*, 2011.

[13] Ding Li. New coulomb logarithm and its effects on the fokker-planck equation, relaxation times and cross-field transport in fusion plasmas. *Nuclear Fusion*, 41:631–635, 2001.

[14] John Wesson. *Tokamaks.* Oxford University Press, 2004.

[15] Jeffrey Freidberg. *The Plasma Boundary of Magnetic Fusion Devices.* Cambridge, 2007.

[16] Jimmie D. Lawson. Some criteria for a power producing thermonuclear reactor. 1957.

[17] J. W. Kesner and Robert W. Conn. Space-dependent effects on the lawson and ignition conditions and thermal equilibria in tokamaks. *Nuclear Fusion*, 16:397 – 404, 1976.

[18] Fabio Subba. Notes on nuclear fusion reactor physics. *Politecnico di Torino*, 2023.

[19] Yuntao Song, Weiyue Wu, and Shijun Du. Tokamak engineering mechanics. 2013.

[20] L. Jr. Spitzer. The stellarator concept. *IEEE Transactions on Plasma Science*, 9:130–141, 1958.

[21] Shunjie Li, H. Jiang, Zhigang Ren, and Chao Xu. Optimal tracking for a divergent-type parabolic pde system in current profile control. *Abstract and Applied Analysis*, 2014, 2014.

[22] Alberto Loarte, Bruce Lipschultz, A S Kukushkin, G. F. Matthews, P. C. Stangeby, Nobuyuki Asakura, Glenn Counsell, Gianfranco Federici, Arne Kallenbach, K. Krieger, Amirmehran Mahdavi, Volker Philipps, Detlev Reiter, J. Roth, James Douglas Strachan, Daniel G. Whyte, Russell P. Doerner, Thomas Eich, Wojciech R. Fundamenski, Albrecht Herrmann, M. Fenstermacher, Philippe Ghendrih, Mathias Groth, Andreas Kirschner, S. Konoshima, Brian LaBombard, Peter Thomas Lang, Anthony W Leonard, Pascale Monier-Garbet, Rudolf Neu, H. D. Pacher, Brigitte Pégourié, Richard A. Pitts, Shuichi Takamura, J. L. Terry, and E. Tsitrone. Chapter 4: Power and particle control. *Nuclear Fusion*, 47:S203 – S263, 2007.

[23] Antonino Cardella, K. Skladnov, K. Ioki, H. D. Pacher, Yu.S. Strebkov, and W. Daenner. Design and manufacturing of the iter limiter. *Fusion Engineering and Design*, 61:111–116, 2002.

[24] C. S. Pitcher and P. C. Stangeby. Experimental divertor physics. *Plasma Physics and Controlled Fusion*, 39:779–930, 1997.

[25] Bastiaan J. Braams. Radiative divertor modelling for iter and tpx. *Contributions To Plasma Physics*, 36:276–281, 1996.

[26] Holger Reimerdes et al. Assessment of alternative divertor configurations as an exhaust solution for demo. *Nuclear Fusion*, 60, 2020.

[27] V. Soukhanovskii. A review of radiative detachment studies in tokamak advanced magnetic divertor configurations. *Plasma Physics and Controlled Fusion*, 59, 2017.

[28] Richard A. Pitts, Xavier Bonnin, Frédéric Escourbiac, Heinke Frerichs, J. P. Gunn, Takeshi Hirai, A. S. Kukushkin, Elizaveta Kaveeva, M. A. Miller, David Moulton, V. Rozhansky, Ilya Y Senichenkov, Elizaveta Sytova, Oliver Schmitz, P. C. Stangeby, Gregory De Temmerman, I. Yu. Veselova, and Sven Wiesen. Physics basis for the first iter tungsten divertor. *Nuclear Materials and Energy*, 2019.

[29] Sergei I. Krasheninnikov and A. S. Kukushkin. Physics of ultimate detachment of a tokamak divertor plasma. *Journal of Plasma Physics*, 83, 2017.

[30] G. F. Matthews. Plasma detachment from divertor targets and limiters. *Journal of Nuclear Materials*, pages 104–116, 1995.

[31] Joachim Roth. Chemical erosion of carbon based materials in fusion devices. *Journal of Nuclear Materials*, 266:51–57, 1999.

[32] Alberto Loarte, Robert D.G. Monk, Jose Ramon Martin-Solis, David J. Campbell, Alex Chankin, S. Clement, S. J. Davies, Jürgen Ehrenberg, S. K. Erents, Houyang Y Guo, Peter J. Harbour, L. D. Horton, L. C. Ingesson, Heinz Jäckel, Johann Lingertat, C. G. Lowry, Costanza F Maggi, G. F. Matthews, K. Mccormick, David P. O'Brien, Roger Reichle, G. Saibene, R. J. Smith, M. F. Stamp,

David G. Stork, and George C. Vlases. Plasma detachment in jet mark i divertor experiments. *Nuclear Fusion*, 38:331–371, 1998.

[33] Holger Reimerdes, S. Alberti, P. Blanchard, Pierluigi Bruzzone, René Chavan, Stefano Coda, B. Duval, Ambrogio Fasoli, Benoit Labit, Bruce Lipschultz, Tilmann Lunt, Y. Martin, J-M. Moret, Umar Ahmed Sheikh, Bassem Sudki, Duccio Testa, Christian Theiler, M. Toussaint, Davide Uglietti, Nicola Vianello, and M. Wischmeier. Tcv divertor upgrade for alternative magnetic configurations. *Nuclear materials and energy*, 12:1106–1111, 2017.

[34] Holger Reimerdes, B. Duval, H. Elaian, Ambrogio Fasoli, Olivier Février, Christian Theiler, F. Bagnato, M. Baquero-Ruiz, P. Blanchard, Dominik Brida, Claudia Colandrea, H. de Oliveira, Davide Galassi, Sophie Gorno, S. Henderson, Michael Komm, Bryan Lee Linehan, L Martinelli, Roberto Maurizio, J-M. Moret, Artur Perek, Harshita Raj, Umar Ahmed Sheikh, D. Testa, M. Toussaint, Cedric Kar-Wai Tsui, Mirko Wensing, the TCV team, the EUROfusion MST1 team, and C. Tsironis. Initial tcv operation with a baffled divertor. *Nuclear Fusion*, 61, 2021.

[35] Holger Reimerdes. Overview of the tcv tokamak experimental programme. *Nuclear Fusion*, 62, 2022.

[36] Iter physics basis. *Nuclear Fusion*, 39, 1999.

[37] Mirko Wensing, B. Duval, Olivier Février, A. Fil, Davide Galassi, E. Havlícková, Artur Perek, Holger Reimerdes, Christian Theiler, Kevin Verhaegh, Kevin Verhaegh, and M. Wischmeier. Solps-iter simulations of the tcv divertor upgrade. *Plasma Physics and Controlled Fusion*, 61, 2019.

[38] G. Sun, Holger Reimerdes, Christian Theiler, B. Duval, Massimo Carpita, Claudia Colandrea, and Olivier Février. Performance assessment of a tightly baffled, long-legged divertor configuration in tcv with solps-iter. *Nuclear Fusion*, 63, 2023.

[39] M. Kočan, J.P. Gunn, S. Carpentier-Chouchana, A. Herrmann, A. Kirk, M. Komm, H.W. Müller, J.-Y. Pascal, R.A. Pitts, V. Rohde, and P. Tamain. Measurements of ion energies in the tokamak plasma boundary. *Journal of Nuclear Materials*, 415(1, Supplement):S1133–S1138, 2011.

[40] Mirko Wensing, Holger Reimerdes, Olivier Février, Claudia Colandrea, L Martinelli, Kevin Verhaegh, F. Bagnato, P. Blanchard, B. Vincent, Artur Perek, Sophie Gorno, H. de Oliveira, Christian Theiler, B. Duval, Cedric Kar-Wai Tsui, M. Baquero-Ruiz, and M. Wischmeier. Solps-iter validation with tcv l-mode discharges. *Physics of Plasmas*, 2021.

[41] Harold M. Mott-Smith and Irving Langmuir. The theory of collectors in gaseous discharges. 1926.

[42] Radu Balescu. *Transport processes in plasmas*. North-Holland, 1988.

[43] J. W. Connor. Transport in tokamaks: Theoretical models and comparison with experimental results. *Plasma Physics and Controlled Fusion*, 37, 1995.

[44] F. L. Hinton and R. D. Hazeltine. Theory of plasma transport in toroidal confinement systems. *Reviews of Modern Physics*, 48:239–308, 1976.

[45] P. Helander and D.J. SIGMAR. *Collisional transport in magnetized plasmas*. Cambridge University Press, 2002.

[46] W. M. Tang. Microinstability theory in tokamaks. *Nuclear Fusion*, 18:1089 – 1160, 1978.

[47] Wendell Horton. Drift waves and transport. *Reviews of Modern Physics*, 71:735–778, 1999.

[48] Wendell Horton, Duk In Choi, and William M. Tang. Toroidal drift modes driven by ion pressure gradients. *Physics of Fluids*, 24:1077–1085, 1981.

[49] John W. Conner and Howard R Wilson. Survey of theories of anomalous transport. *Plasma Physics and Controlled Fusion*, 36:719–795, 1994.

[50] Alex Chankin and P. C. Stangeby. The effect of diamagnetic drift on the boundary conditions in tokamak scrape-off layers and the distribution of plasma fluxes near the target. *Plasma Physics and Controlled Fusion*, 36:1485–1499, 1994.

[51] B.R. Munson, A.P. Rothmayer, and T.H. Okiishi. *Fundamentals of Fluid Mechanics, 7th Edition*. Blackwell handbooks in linguistics. Wiley, 2012.

[52] S. I. Braginskii. *Transport Processes in a Plasma*. 1965.

[53] Peter Hunana, Thierry Passot, Elena Khomenko, David Martínez-Gómez, Manel Collados, Anna Tenerani, Gary P. Zank, Yana G. Maneva, Melvyn L. Goldstein, and Gary M. Webb. Generalized fluid models of the braginskii type. *The Astrophysical Journal Supplement Series*, 260, 2022.

[54] Andrew Guthrie and R. K. Wakerling. The characteristics of electrical discharges in magnetic fields. 1949.

[55] Riemann. Bohm's criterion and plasma-sheath trasmission. *Contrib. Plasma Phys.*, 36, 1996.

[56] R. Chodura. Plasma–wall transition in an oblique magnetic field. *Physics of Fluids*, 25:1628–1633, 1982.

[57] P. C. Stangeby. The bohm–chodura plasma sheath criterion. *Physics of Plasmas*, 2:702–706, 1995.

[58] A. S. Kukushkin, H. D. Pacher, Vladislav Kotov, G. W. Pacher, and Detlev Reiter. Finalizing the iter divertor design: The key role of solps modeling. *Fusion Engineering and Design*, 86:2865–2873, 2011.

[59] P. C. Stangeby. Basic physical processes and reduced models for plasma detachment. *Plasma Physics and Controlled Fusion*, 60, 2018.

[60] V. Kotov and D. Reiter. Two-point analysis of the numerical modelling of detached divertor plasmas. *Plasma Physics and Controlled Fusion*, 51:115002, 2009.

[61] P. C. Stangeby, Jeremy D. Lore, Richard A. Pitts, J. M. Canik, and Xavier Bonnin. A reduced model for the iter divertor based on solps solutions for iter q = 10 baseline conditions: B. a reduced model based on reversed-direction two point modeling. *Nuclear Fusion*, 63, 2022.

[62] Peter Stangeby. The roles of power loss and momentum-pressure loss in causing particle-detachment in tokamak divertors: Ii. 2 point model analysis that includes recycle power-loss explicitly. *Plasma Physics and Controlled Fusion*, 62, 2019.

[63] Thomas Walter Petrie, J. M. Canik, Charles Lasnier, Anthony W Leonard, Mehrzad Mahdavi, J. G. Watkins, M. Fenstermacher, John R. Ferron, Richard J Groebner, David N. Hill, A. Hyatt, Christopher T. Holcomb, T. C. Luce, M. A. Makowski, R. A. Moyer, Terry E. Osborne, and P. C. Stangeby. Effect of changes in separatrix magnetic geometry on divertor behaviour in diii-d. *Nuclear Fusion*, 53, 2013.

[64] F. Nespoli, Hugo Bufferand, M. Valentinuzzi, N. Fedorczak, Guido Ciraolo, Eric Serre, Yannick Marandet, Roberto Maurizio, H. de Oliveira, Benoit Labit, Michael Komm, Michael Faitsch, and S. Elmore. Application of a two-fluid two-point model to soledge2d-eirene simulations of tcv h-mode plasma. *Nuclear Materials and Energy*, 2019.

[65] X. J. Zhang, Francesca M Poli, E.D. Emdee, and Mario Podestà. Reduced physics model of the tokamak scrape-off-layer for pulse design. *Nuclear Materials and Energy*, 2022.

[66] Sven Wiesen, Detlev Reiter, Vladislav Kotov, Martine Baelmans, Wouter Dekeyser, A. S. Kukushkin, Steven W. Lisgo, Richard A. Pitts, V. Rozhansky, G. Saibene, I. Yu. Veselova, and S. P. Voskoboynikov. The new solps-iter code package. *Journal of Nuclear Materials*, 463:480–484, 2015.

[67] Braams B. *Computational Studies in Tokamak Equilibrium and Transport.* PhD thesis, Rijksuniversiteit, Utrecht, 1986.

[68] Baelmans M. *Code improvements and applications of a two-dimensional edge plasma model for toroidal devices.* PhD thesis, Katholieke Universiteit, Leuven, 1994.

[69] Ralf Schneider, Xavier Bonnin, Kurt Borrass, David P. Coster, H. Kastelewicz, Detlev Reiter, V. Rozhansky, and Bastiaan J. Braams. Plasma edge physics with b2-eirene. *Contributions to Plasma Physics*, 46, 2006.

[70] D. Reiter. Eirene manual. 2023.

[71] Reiter D. *Randschicht-konfiguration von tokamaks: entwicklung und anwendung stochastischer modelle zur beschreibung des neutralgastransports.* PhD thesis, 1984.

[72] Detlev Reiter, Martine Baelmans, and P. Börner. The eirene and b2-eirene codes. *Fusion Science and Technology*, 47:172 – 186, 2005.

[73] David P. Coster, J. W. Kim, Günter Haas, B. Kurzan, Heindieter Murmann, J. Neuhauser, Hans Salzmann, Ralf Schneider, Wolfgang Schneider, and Josef Schweinzer. Automatic evaluation of edge transport coefficients with b2-solps5.0. *Contributions To Plasma Physics*, 40:334–339, 2000.

[74] Paolo Ricci. Simulation of the scrape-off layer region of tokamak devices. *Journal of Plasma Physics*, 81, 2015.

[75] Wouter Dekeyser, Reinart Coosemans, Stefano Carli, and Martine Baelmans. A self-consistent κ-model for anomalous transport due to electrostatic, interchange-dominated e × b drift turbulence in the scrape-off layer and implementation in solps-iter. *Contributions to Plasma Physics*, 62, 2022.

[76] Weston M. Stacey. Comparison of theoretical and experimental heat diffusivities in the diii-d edge plasma. *Physics of Plasmas*, 15:052503, 2008.

[77] Andrei Maximov and Viktor P. Silin. Theory of nonlocal heat transport in fully ionized plasma. *Physics Letters A*, 173:83–86, 1993.

[78] John Omotani and Ben D Dudson. Non-local approach to kinetic effects on parallel transport in fluid models of the scrape-off layer. *Plasma Physics and Controlled Fusion*, 55, 2013.

[79] Michael Robert Knox Wigram, Christopher P. Ridgers, Ben D Dudson, J. P. Brodrick, and J T Omotani. Incorporating nonlocal parallel thermal transport in 1d iter sol modelling. *Nuclear Fusion*, 60, 2020.

[80] Wojciech R. Fundamenski. Parallel heat flux limits in the tokamak scrape-off layer. *Plasma Physics and Controlled Fusion*, 47:R163 – R208, 2005.

[81] David P. Coster, Xavier Bonnin, Bastiaan J. Braams, Detlev Reiter, Reinhold Schneider, and the ASDEX Upgrade team. Simulation of the edge plasma in tokamaks. *Physica Scripta*, 2004:7 – 13, 2004.

Ringraziamenti

Ci tengo a ringraziare innanzitutto il mio relatore presso il Politecnico di Torino, il Professor Fabio Subba. Lo ringrazio per la sua disponibilità, per il suo interesse nel lavoro svolto e per avermi fatto conoscere meglio un ambito che ritengo veramente affascinante. Un forte ringraziamento va anche ai miei relatori presso lo Swiss Plasma Center, il Prof. Holger Reimerdes ed Elena Tonello per l'opportunità che mi hanno concesso e per il lavoro svolto assieme. Un grazie va anche a tutto il team di SOLPS ed al Boundary team. Sono grato di aver potuto lavorare in un posto del genere, in mezzo a tantissime menti brillanti e persone di gran simpatia. Mi sento di essere maturato tanto come persona e di aver imparato altrettanto a livello professionale durante questo mio periodo a Losanna, e questo è anche grazie a tutti loro.

Un grazie infinito va anche ai miei genitori Rita e Ignazio, che nel bene o nel male mi hanno sempre sostenuto. Un grazie va a Clara, che mi è sempre stata accanto, nei momenti bui come nei momenti di luce, credendo sempre in me e nelle mie capacità. Grazie anche ai miei cugini, che per me sono come dei fratelli e so che ci sono sempre. Un grazie ai miei nonni, alle mie zie e a mio zio che ci sono da sempre. Infine, un grazie va a tutti i miei amici, dal più datato al meno, vi voglio bene e sono contento di avervi incontrato nella mia vita. Ancora un grazie a tutti voi, dal primo all'ultimo, che in un modo o nell'altro avete un posto importante nella mia vita e so di poter contare su di voi, come voi potete contare su di me.

Torino, Marzo 2025

S. D.